UNIVERSITÄT OSNABRÜCK

Dissertation

at the **Osnabrück University**

for the conferral of the degree
“Doctor rerum naturalium” (Dr. rer. nat.)

Topic

Open geospatial data fusion and its application in sustainable urban development

Submitted on 04/07/2019 and defended on 08/27/2019 by

Shaojuan Xu

born on August 6, 1982 in Henan,
People's Republic of China

Supervisor: Manfred Ehlers
Co-Supervisor: Peter Reinartz

Osnabrück University
School of Mathematics/Computer Science
Institute of Computer Science

Osnabrück, 2020

Universität Osnabrück

To my husband,
Johannes Karl,

and to my children,
Jan and Kai

Acknowledgments

First and foremost, I would like to express my deepest appreciation for my supervisor, Prof. Dr. Manfred Ehlers, who provided me with the opportunity to work as a researcher in the field of remote sensing and geoinformatics. Thank you for accepting me in your group, even though my academic background was only partially related to the group's work. When I first started, I was captured by the powerful technologies being used, and you encouraged me to explore different ideas. Throughout my time here, you introduced me to the topic of data fusion, shared your professional knowledge, guided me through the obstacles that I faced during the thesis project, and revised this thesis carefully. Additionally, you are always reliable and helpful when I need support. With your open-mindedness and profound knowledge, you have set an excellent example for me to pursue my academic career.

I have been blessed for having had the pleasure of working with some of the most helpful and wonderful colleagues. To Dr. Christine Pohl, thank you for your guidance and enthusiasm. Your resilience and work ethic will always be a source of inspiration to me. Thanks also for helping to proof-read and comment on parts of this thesis despite your other commitments. Also special thanks to Prof. Dr. Peter Reinartz to take over the co-supervising of this thesis, and Prof. Dr. Jochen Schiewe for his evaluation of this thesis. I want to thank all professors and colleagues that I met at the Institute of Computer Science of Osnabrück University for sharing their knowledge with me during the past years: Bastian Albers, Doris Middelbeck, Florian Beyer, Sandra Dützer, Dr. Yevgeniya Filippovska, Prof. Dr. Jan-Henrik Haunert, Dr. Florian Hillen, Dr. Thomas Jarmer, Dr. Richard Jung, Prof. Dr. Norbert de Lange, Prof. Dr. Martin Kada, Martin Kanning, Thomas Kastler, Nina Manzke, Dr. Daniel Mwaura, Johannes Oehrlein, Dr. Bastian Siegmann, Timo Otte-Vinke, Dr. Andreas Wichmann, and Jan Zülsdorf.

A special thanks to Dirk Ohde and Jens Born from the Department Geodaten und Verkehrsanlagen of the city of Osnabrück. Thank you for sharing the data and helping me without asking for anything in return.

I am grateful to Osnabrück University for the family-friendly working environment, so that I could balance my responsibilities at work and life. Many thanks to the Equality Office of the university, which provided the scholarship to finish my doctoral studies.

My sincere thanks to my friend, Dr. Chee Keong Kwok, who always provides his time and patience to help me with the wording of my thesis. I feel so lucky to have you as a friend.

I am grateful to my parents, Shuzhen Li and Gaoyong Xu, and parents-in-law, Elisabeth Schmees-Haidegger and Johannes Severin Schmees, who helped me with my two little children Jan and Kai. Without your help, I would not have been able to get through this challenging time.

Finally, last but by no means least, heartfelt thanks go to my husband, Johannes Karl Schmees, who believes in gender equality and is trying everything to firmly implement this idea within our family. Performing the doctoral project, in addition to working and having two kids, is harder than I could have ever imagined. But I cannot give up, thinking of all the effort you have put in to support me.

Table of Contents

List of Figures

List of Tables

List of Abbreviations

ALOS	Advanced Land Observing Satellite
API	Application Programming Interface
ASAR	Advanced Synthetic Aperture Radar
ASTER	Advanced Spaceborne Thermal Emission and Reflection Radiometer
AVHRR	Advanced Very High Resolution Radiometer
AVIRIS	Airborne Visible/Infrared Imaging Spectrometer
CBERS	China-Brazil Earth Resources Satellite
CC	correlation coefficient
CHRIS	Compact High Resolution Imaging Spectrometer
CLC	CORINE Land Cover
DN	digital numbers
EEA	European Environment Agency
EO	Earth observation
EO-1	Earth Observing-1
EPA	United States Environmental Protection Agency
ERGAS	relative dimensionless global error of synthesis
ERS	European Remote Sensing Satellite
ESA	European Space Agency
ETM+	Enhanced Thematic Mapper Plus
EU	European Union
FFT	fast Fourier transform
FOEN	Federal Office for the Environment of Switzerland
GEO	Group on Earth Observations
GFF	General framework for image fusion
GIF	General image fusion
GIS	geographical information system
GOS	green and open spaces
GPS	global positioning system
GRASS GIS	Geographic Resources Analysis Support System GIS
HPF	high-pass filter
HyMap	Hyperspectral Mapper
IHS	Intensity-Hue-Saturation
INSPIRE	Infrastructure for Spatial Information in Europe
JAXA	Japan Aerospace Exploration Agency
JERS	Japan Earth Resources Satellite
J-spacesystems	Japan Space Systems
LST	land surface temperature
METI	Japan’s Ministry of Economy, Trade and Industry
MODIS	Moderate Resolution Imaging Spectroradiometer
MS	multispectral
MSS	Multi Spectral Scanner
NASA	National Aeronautics and Space Administration
NDVI	normalized difference vegetation index

NIR	Near-Infrared
NOAA	National Oceanic and Atmospheric Administration
OGC	Open Geospatial Consortium
OLI	Operational Land Imager
OSM	OpenStreetMap
PALSAR	Phased Array type L-band Synthetic Aperture Radar
PC	principal component
PDA	potential development area
QGIS	Quantum-GIS
RASE	relative average spectral error
RGB	red, green, and blue
RMSE	root mean square error
SAR	Synthetic Aperture Radar
SEDAC	Socioeconomic Data and Applications Center
SNAP	Sentinel Application Platform
STRM	Shuttle Radar Topography Mission
SWIR	short-wavelength infrared
TIR	Thermal infrared
TM	Thematic Mapper
TOA	top of the atmosphere
UA	Urban Atlas
UAV	unmanned aerial vehicle
UHI	urban heat island
UIQI	universal image quality index
UK	United Kingdom of Great Britain and Northern Ireland
UN	United Nations
URBIS	URBan land recycling Information services for Sustainable cities
USGS	United States Geological Survey
VI	vegetation index
VIS	visible
WGS	World Geodetic System
WWW	World Wide Web

Abstract

This thesis presents the implementation of data fusion techniques for sustainable urban development. Recently, increasingly more geospatial data have been made easily available for no cost. The immeasurable quantities of geospatial data are mainly from four kinds of sources: remote sensing satellites, geographic information systems (GIS) data, citizen science, and sensor web. Among them, satellite images have been mostly used, due to the frequent and repetitive coverage, as well as the data acquisition over a long time period.

However, the rather coarse spatial resolution of e.g. 30 m for Landsat 8 multispectral images impairs the application of satellite images in urban areas. Even though image fusion techniques have been used to improve the spatial resolution, the existing image fusion methods are neither suitable for sharpening one band thermal images nor for hyperspectral images with hundreds of bands. Therefore, simplified Ehlers fusion was developed. It adds the spatial information of a high-resolution image into a low-resolution image in the frequency domain through fast Fourier transform (FFT) and filter techniques. The developed algorithm successfully improved the spatial resolution of both one band thermal images as well as hyperspectral images. It can enhance various images, regardless of the number of bands and the spectral coverage, providing more precise measurement and richer information.

To investigate the performance of simplified Ehlers fusion in practical use, it was applied for urban heat island (UHI) analysis. This was done by sharpening daytime and nighttime thermal images from Landsat 8, Landsat 7, and the Advanced Spaceborne Thermal Emission and Reflection Radiometer (ASTER). The developed algorithm effectively improved the spatial details of the original images so that the temperature differences between agricultural, forest, industrial, transportation, and residential areas could be distinguished from each other. Based on that, it was found that in the study city the causes of UHI are mainly anthropogenic heat from industrial areas as well as high temperatures from the road surface and dense urban fabric. Based on this analysis, corresponding mitigation strategies were tailored.

Remote sensing images are useful yet not sufficient to retrieve land use related information, despite high spatial resolution. For sustainable urban development research, remote sensing images need to be incorporated with data from other sources. Accordingly, image fusion needs to be extended to broader data fusion. Extraction of urban vacant land was therefore taken as a second application case. Much effort was spent on the definition of vacant land as unclear definitions lead to ineffective data fusion and incorrect site extraction results. Through an intensive study of the current research and the available open data sources, a vacant land typology is proposed. It includes four categories: transportation-associated land, natural sites, unattended areas or remnant parcels, and brownfields. Based on this typology, a two-level data fusion framework was developed. On the feature level, sites are identified. For each type of vacant land, an individual site extraction rule and data fusion procedure is implemented. The overall data fusion involves satellite images, GIS data, citizen science, and social media data. In the end, four types of vacant land features were extracted from the study area. On the decision level, these extracted sites could be conserved or further developed to support sustainable urban development.

Keywords: brownfield, data fusion, geospatial data analysis, image sharpening, open data, sustainable urban development, urban heat island, vacant land

Zusammenfassung (German abstract)

In der vorliegenden Arbeit werden offene Geodaten durch Datenfusionstechniken für die Stadtforschung nutzbar gemacht. Dabei ist zu beobachten, dass immer mehr Geodaten frei zur Verfügung gestellt werden – zumeist stammen sie aus vier Quellen: Fernerkundungssatelliten, GIS-Daten, Citizen Science (Bürgerwissenschaft) sowie Websensoren. Satellitenbilder werden aufgrund der häufigen und wiederholten Abdeckung eines Gebiets sowie der Datenerfassung über einen längeren Zeitraum hinweg am häufigsten eingesetzt.

Die grobe räumliche Auflösung bspw. der multispektralen Bilddaten von Landsat 8 von 30 m beeinträchtigt jedoch die Anwendung in städtischen Gebieten. Eine Möglichkeit zur Bildschärfung sind Bildfusionstechniken. Die bestehenden Verfahren sind jedoch weder zum Schärfen von Wärmebildern mit nur einem Band, noch zum Schärfen von hyperspektralen Bildern mit hunderten von Bändern geeignet. Daher wurde im Rahmen des Promotionsprojekts die *simplified Ehlers fusion* entwickelt. Durch diese wird mithilfe einer schnellen Fourier-Transformation (FFT) und Filtertechniken räumliche Informationen eines höher aufgelösten Bildes zu einem Bild mit niedrigerer Auflösung im Frequenzbereich hinzugefügt. Der entwickelte Algorithmus verbesserte erfolgreich die räumliche Auflösung von Wärmebildern auf der einen und hyperspektralen Bildern auf der anderen Seite. Er ist zur Schärfung für unterschiedliche Bildtypen einsetzbar, unabhängig von der Anzahl der Bänder und der spektralen Abdeckungm was insgesamt zu präziseren Messungen und reichhaltigeren Informationen führt.

Um die Leistung der *simplified Ehlers fusion* im praktischen Einsatz zu testen, wurde sie zur Untersuchung von städtischen Wärmeinseln (UHI) eingesetzt. Dazu wurden tagsüber und nachts Wärmebilder von Landsat 8, Landsat 7 und dem *Advanced Spaceborne Thermal Emission and Reflection Radiometer* (ASTER) geschärft. Der entwickelte Algorithmus verbessert effektiv die räumlichen Details der Originalbilder, sodass die Temperaturunterschiede zwischen landwirtschaftlichen Flächen, Wald, Industriegebieten, Transportwegen und Wohngegenden unterscheidbar werden. Basierend auf dieser Analyse können die Ursachen für die UHI in der untersuchten Stadt, die exemplarisch für die Anwendungsfälle herangezogen wurde. gefunden werden. Hauptfaktoren sind demnach die anthropogene Wärme der Industrieanlagen sowie die hohen Temperaturen asphaltierter Straßen und dichter Stadtgefüge. Basierend auf dieser Analyse werden Strategien für die Vermeidung von UHI präsentiert.

Satellitenbilder liefern für zahlreiche Anwendungen hilfreiche Informationen, reichen jedoch trotz mitunter hoher räumlicher Auflösung nicht aus, um detaillierte Informationen zur Landnutzung und Landbedeckung sicher bestimmen zu können. Für die Unterstützung einer nachhaltigen Stadtentwicklung müssen Fernerkundungsbilder daher mit Daten aus anderen Quellen kombiniert werden. Folglich müssen Methoden der Bildfusion um Methoden der Datenfusion erweitert werden. Die Identifikation städtischer Freiflächen wurde daher als zweiter Anwendungsfall ausgewählt. Da eine unklare Definition zu einer ineffektiven Datenfusion und falschen Ergebnissen führt, wurde basierend auf einer intensiven Recherche aktueller Forschungsarbeiten und der verfügbaren offenen Datenquellen eine Typologie von Freiflächen entwickelt. Diese umfasst vier Kategorien: verkehrsbedingte Freiflächen, Naturstätten, vernachlässigte Gebiete oder Restflächen sowie Brachflächen. Basierend auf

dieser Typologie wird ein zweistufiges Verfahren zur Datenfusion präsentiert. Auf der *Feature*-Ebene werden Standorte identifiziert. Für jede Art von Freiflächen wird eine individuelle Regel zur Extraktion und Datenfusion implementiert. Die gesamte Datenfusion basiert auf Satellitenbildern, GIS-Daten sowie durch Citizen Science und soziale Medien gewonnen Daten. Schließlich wurden vier Arten von Freiflächen in dem Untersuchungsgebiet identifiziert. Auf der Entscheidungsebene könnten diese abgebauten Standorte konserviert oder städtebaulich erschlossen werden, um eine nachhaltige Stadtentwicklung zu unterstützen.

Schlüsselwörter: Bildschärfung, Brachfläche, Datenfusion, Freifläche, Geodatenanalyse, nachhaltige Stadtentwicklung, offene Daten, städtische Wärmeinsel

1. Introduction

This chapter describes the geospatial data development background, which shows that vast data has been freely accessible and more open source data will become available. However, it is still not clear how to fuse these freely accessible data together to get even more accurate and useful information for urban research. Therefore, this thesis takes three steps to present geospatial data fusion: firstly, an image fusion algorithm is developed for improving the spatial resolution of various remote sensing images; afterward, the developed algorithm is applied to sharpen remote sensing thermal images and the sharpened images are then used for urban heat island (UHI) analysis which is the first application case; at the end, urban vacant land identification is taken as the second practical use case to emphasize the situation that only remote sensing images alone are not sufficient to analyze urban issues, where remote sensing images need to be integrated with geographical information system (GIS) data and volunteered geographic information.

1.1. Open geospatial data

In September 2015, the United Nations (UN) officially endorsed all countries' support for the public-private cooperation to contribute to the availability of Earth observation (EO) and geospatial information in the 2030 agenda for sustainable development (UN, 2015). In the last decades, governments from around the world started to call for cooperation in sharing geospatial data as well as to promote open geospatial data initiatives, as they realized that these data foster opportunities for economic, social, and environmental developments. Supported by a succession of G20 and G7/G8 meetings, the globally recognized Group on Earth Observations (GEO) is a community of more than 100 national governments and 100 participating organizations that work towards a future where decisions and actions for the betterment of humankind are guided by Earth observations (GEO, n.d.). Encouraged by GEO, several initiatives have made it possible to open access to geospatial data, namely Global Forest Watch, Ocean Climate Change, Global Marine Biodiversity Observational Network, Global Agricultural Monitoring, and Water Sustainability. A majority of countries have enacted policies to improve access to open geospatial data, typically including topography and data regarding land use and land cover—this aims at encouraging more participants and stakeholders to use the geospatial information with opportunities for more participation in science, politics, and social action (Craglia and Shanley, 2015).

Directed by the governments, space agencies operate various programs offering vast amounts of free data from satellites as well as ground-based, airborne, and seaborne measurements. For example, Landsat represents the world's longest continuously acquired collection of remote sensing data. It is a joint initiative between the United States Geological Survey and the National Aeronautics and Space Administration (NASA). NASA is responsible for most of the worldwide earth observation programs such as the Advanced Spaceborne Thermal Emission and Reflection Radiometer (ASTER) and the Moderate Resolution Imaging Spectroradiometer (MODIS). Copernicus is the European Union's EO program, which is operated by the European Space Agency (ESA) together with other partners. This program is served by a set of satellites, among which Sentinel-1 provides day and night radar imagery, Sentinel-2 offers optical imagery, and Sentinel-3 focuses on sea surface and land surface temperature. Other Sentinel family members are scheduled to be launched in the future. Also, the Japan Aerospace

Exploration Agency (JAXA) contributes a worldwide digital surface model using the Advanced Land Observing Satellite (ALOS). Among the open satellite data sources, NASA and ESA are the main providers.

There are also programs that provide regional data only. For example, the China-Brazil Earth Resources Satellite (CBERS) was established through the cooperation between the National Institute for Space Research and the Chinese Academy of Space Technology. However, only the data covering South America and Africa provided by CBERS is freely accessible. India, too, has built up a geospatial data platform by its National Remote Sensing Centre, which distributes free satellite data products in India and its neighboring countries.

Not only space agencies from around the world, but also organizations and stakeholders from the business sector are contributing to open geospatial data sources. The Esri ArcGIS Hub holds more than 220,000 data sets from more than 2,400 organizations worldwide (ArcGIS, 2019). The Socioeconomic Data and Applications Center (SEDAC) from NASA hosted by Columbia University, New York, provides more than 200 global and national data sets covering themes regarding human interactions with the environment, such as the Last of the Wild initiative which mapped the last remaining wild areas on Earth, and the Population Exposure Estimates in Proximity to Nuclear Power Plants, Locations data set which provides global point locations describing nuclear power plants and reactors.

Besides the above official sources, citizen science is gradually becoming a common way of collecting geospatial data. Rapidly developed web mapping technologies have made it relatively easy for volunteers to map, enter data, and participate in online activities. Citizen science projects allow any interested individual to contribute information through online platforms or online tools. This technology can assist geographers to collect information from citizen science databases. The citizen science research approach can result in positive overall satisfaction for different users and support a wide variety of tasks with reliable data quality. For instance, Parr and Scholz (2015) have developed a web mapping and data collection site which allows users, regardless of GIS experience, to submit possible low water crossing locations in addition to descriptions and photos, for the purpose of identifying potential roadway flooding hazards. The most popular and prominent volunteered geographic information product is OpenStreetMap (OSM), which is a free and editable digital map of the world (http://wiki.openstreetmap.org).

Sensor web has emerged as an important EO data acquisition source. With the development of web technology, various vastly distributed sensors are connected to the World Wide Web (WWW). Sensor web services enable online publishing and sharing of the data produced and collected by the sensors. It can be used to obtain real-time and *in situ* observations for environmental monitoring (Zheng *et al.*, 2012), as well as to assist disaster management (Wang and Yuan, 2010). In recent years, a focus has been on sensor systems which integrate *in situ* devices, remote sensing satellites, stationary sensors, and sensors attached to mobile platforms. For instance, EO web is a data acquisition and processing network which comprises the EO sensor, the sensor network, and the Internet (Chen *et al.*, 2014). Thus, sensor web is defined as an infrastructure which enables an interoperable usage of sensor resources by enabling their discovery, access, tasking, as well as eventing and alerting within the WWW in a standardized way (Bröring *et al.*, 2011).

While many focus on making data open, the awareness of open source geo-processing tools, software, and standards has also been raised. Quantum-GIS (QGIS) and Geographic Resources Analysis Support System GIS (GRASS GIS) are open source software which are commonly used for geospatial data management and analysis. QGIS is the leading open source desktop GIS. It is composed of the core functions and plugins. Users are encouraged to develop their own applications for the software. Due to the increasing contribution from users, the capabilities of the software are growing continuously. For instance, QGIS has integrated the SentinelHub plugin for using the latest Sentinel Satellite data. However, this function has not been included in the commercial software ArcGIS.

GRASS GIS is a sister project of QGIS. Whereas QGIS has an easy user interface similar to other common GIS software, GRASS GIS is built upon a location concept to benefit a team to simultaneously work in the same project database. They complement each other as well as share their toolbox and processing commands. Like QGIS, GRASS GIS has been under continuous development because of the user community.

Open source software is driven by and relies on volunteers. This feature does not impair its quality and user experience. Taking the 3D data visualization function from GRASS GIS as an example, it runs much faster and presents a better 3D effect than using the 3D Analyst tool ArcScene from ArcGIS.

Compared to QGIS and GRASS GIS, which focus on general geospatial data analysis and map making, the Sentinel Application Platform, usually referred to as SNAP (Sentinel Application Platform), is another open source software that is tailored for processing Sentinel data and data from similar sensors. It is provided by the ESA and integrates the necessary functions to download, pre-process, and classify satellite images.

Open Geospatial Consortium (OGC) Standards “support interoperable solutions that ‘geo-enable’ the web, wireless and location-based services and mainstream IT” (OGC, 2019). It aims to enable spatial search engines to discover and access web-based geospatial data, geoprocessing web services, and data from web-connected sensors. In the same way that OGC facilitates the sharing of spatial data, Infrastructure for Spatial Information in Europe, usually referred to as INSPIRE, aims to provide necessary standards across EU (European Union) member states. It established an infrastructure for searching, viewing, and downloading spatial data.

Open geospatial data, software, and standards together have created an “open” movement (Bakillah and Liang, 2016), promoting the availability of up-to-date, reliable, and interoperable open geospatial data. This movement has produced a significant impact on the sustainable urban research based on open geospatial data.

1.2. The role of open geospatial data in sustainable urban development

With the emergence of vast open source data, they have been integrated into urban research. This subchapter provides an overview of the studies which have used open geospatial data to address key environmental issues in the development of sustainable cities. According to the different types of data sources, the subchapter is divided into three sections.

1.2.1. Remote sensing images

Due to the increasing number of operational satellites from international space agencies, the amount of data produced by satellites is increasing exponentially. Remote sensing satellite images have some features, such as global coverage, high revisit frequency, and long term acquisition plans, which are particularly beneficial for monitoring urban development. Therefore, they are considered as the most important open source data and the focus of this thesis. Depending on the sensors equipped on the satellite, various types of data can be produced.

Optical remote sensing data deal with visible and near infrared observations, among which the visible part is similar to the human perception of objects. Thermal remote sensing sensors measure the emitted radiation of the Earth's surface as radiant temperature. Synthetic Aperture Radar (SAR) provides texture, geometry, and moisture-sensitive information, and cannot be directly interpreted by non-professionals (Pohl and van Genderen, 2017). Hyperspectral sensors have the advantages of finding objects and identifying materials due to "the acquisition of images in hundreds of contiguous registered spectral bands such that for each pixel a radiant spectrum can be derived" (Goetz *et al.*, 1985, p. 1147). Thermal images generally have coarser spatial resolution than other remote sensing images. Hyperspectral images are rare sources, as spaceborne hyperspectral imaging is still in the experimental phase, such as the Hyperion which is from a demonstration mission and was ended in 2017 (USGS, 2018a), as well as the Compact High Resolution Imaging Spectrometer (CHRIS) which is from the demonstration mission Proba-1 (ESA, 2019). Table 1 summarizes the available free optical, SAR, thermal, and hyperspectral data sources from different providers. This table shows that NASA is the main resource provider and most satellite images have coarse spatial resolution. Based on these open data sources, research about urban sustainable development have been conducted in various aspects.

Typically, multi-temporal Landsat images are employed to analyze urban sprawl and monitor urban changes. Features indicating urbanization are extracted from a series of multispectral images, then changes in these features are used as indicators of urban development. For instance, linear features which indicate buildings and roads are extracted to quantify and assess the patterns of urbanization, as city growth is typically demonstrated by the expansion of a city's infrastructure (Al-Ruzouq *et al.*, 2017). Similarly, edges indicate regular shape in the human-disturbed landscapes rather than natural landscapes; thus edge density can be used to quantitatively examine the fragmentation caused by urban sprawl (Tang *et al.*, 2006). Multi-temporal Landsat images can also be used to assess natural disasters such as flood risk in urban sprawl contexts (Franci *et al.*, 2015).

Often, images from Landsat are combined with images from other satellites to explore the spatiotemporal characteristics of urbanization in the long term. For instance, using Landsat Multi Spectral Scanner (MSS), Landsat Enhanced Thematic Mapper Plus (ETM+), and ASTER images, Liang *et al.* (2013) revealed urban landscape changes and also evaluated urban fractal characteristics of Indianapolis, IN. Mainly based on the data from Landsat and CBERS, Li *et al.* (2016) described the urban sprawl intensity in Chinese coastal zones. With the data from the same satellites, Gao *et al*. (2012) mapped the continuous impervious surface expansion using a series of images spanning four decades.

Table 1 Available open remote sensing data sources (based on Pohl and van Genderen, 2017, chap. 1).

Method	Sensor	Sattelite operator	Resolution in m
Optical	AVHRR	NOAA	1090
	Landsat 8 OLI	NASA	30/15
	Landsat 7 ETM+	NASA	30/15
	Landsat 4/5 TM	NASA, NOAA	30
	Landsat 1–3 MSS	NASA	60
	Sentinel-2	ESA	10, 20, 60
	MODIS	NASA	1000
	ASTER	NASA, METI, J-spacesystems	15/30
SAR	Sentinel-1	ESA	5
	Envisat ASAR	ESA	30
	STRM-C	NASA	30
	STRM-X	NASA	25
	JERS-1	JAXA	18
	ERS-1/2	ESA	30
	ALOS PALSAR*	JAXA	10/3
	Seasat	NASA	25
Thermal	Landsat TM, ETM+, OLI	NASA, NOAA	120/60/100
	Sentinel-6	ESA	1000
	ASTER TIR	NASA, METI, J-spacesystems	90
	MODIS TIR	NASA	1000
	AVHRR TIR	NOAA	1090
Hyperspectral	Hyperion (EO-1)	NASA	30
	CHRIS	ESA	17
	AVIRIS**	NASA	Unfixed

* Selected sites available. ** Airborne sensor (all others space borne).
ALOS: Advanced Land Observing Satellite. ASAR: Advanced Synthetic Aperture Radar. ASTER: Advanced Spaceborne Thermal Emission and Reflection Radiometer. AVHRR: Advanced Very High Resolution Radiometer. AVIRIS: Airborne Visible/Infrared Imaging Spectrometer. CHRIS: Compact High Resolution Imaging Spectrometer. EO-1: Earth Observing-1. ERS: European Remote Sensing Satellite. ESA: European Space Agency. ETM+: Enhanced Thematic Mapper Plus. JAXA: Japan Aerospace Exploration Agency. JERS: Japan Earth Resources Satellite. J-spacesystems: Japan Space Systems. METI: Japan's Ministry of Economy, Trade and Industry. MODIS: Moderate Resolution Imaging Spectroradiometer. MSS: Multi Spectral Scanner. NASA: National Aeronautics and Space Administration. NOAA: National Oceanic and Atmospheric Administration. OLI: Operational Land Imager. PALSAR: Phased Array type L-band Synthetic Aperture Radar. STRM: Shuttle Radar Topography Mission. TIR: Thermal infrared. TM: Thematic Mapper.

Since 2015, Sentinel-2 multispectral images have been freely accessible, with a higher spatial resolution and revisit frequency than Landsat. This data provides a viable complementary source to the pre-existing satellite images. It has been widely used all over the world for land cover mapping, such as in Europe (Abdi, 2020; Rujoiu-Mare *et al.*, 2017), Africa (Forkuor *et al.*, 2018), Asia (Xi *et al.*, 2019), and America (Clerici *et al.*, 2017). The added value of Sentinel-2 data with respect to Landsat 8 have been investigated: for land use and land cover mapping, Sentinel-2 bands produced overall accuracy which is better than Landsat 8 (Topaloğlu *et al.*, 2016); for global human settlement mapping, noticeable improvement of the classification quality was made (Pesaresi *et al.*, 2016); for extraction of green infrastructure, it was more effective at extracting green areas (Labib and Harris, 2018). However, due to the Landsat mission's long history and community maturity, the Landsat mission still benefits researchers worldwide (Papadakis and Milosavljevic, 2019).

Numerous studies focused on retrieving land surface temperatures from thermal images, aiming at UHI monitoring. Several open source platforms collect data continuously over several decades and are thus chosen for long-term thermal pattern analysis. Most popular thermal sources for UHI research include National Oceanic and Atmospheric Administration Advanced Very High Resolution Radiometer (NOAA-AVHRR) (Khorchani *et al.*, 2018; Stathopoulou and Cartalis, 2009), Landsat Thematic Mapper (TM), ETM+, Operational Land Imager (OLI) (Li *et al.*, 2011; Lo and Quattrochi, 2003; Tan *et al.*, 2017; Zhangyan *et al.*, 2006), and MODIS (Hutgens and Vohland, 2014; Mukherjee *et al.*, 2017). Due to the frequent repeated EO of these sensors, the retrieved images are beneficial for monitoring seasonal and annual temperature changes. Besides UHI mapping itself, the relationship between UHI and land cover and land use, built-up areas, vegetation, or impervious surfaces has also been investigated (Heldens *et al.*, 2013; Li *et al.*, 2011; Nie *et al.*, 2016; Weng *et al.*, 2004), as the effects of landscape pattern on UHI is crucial for understanding the impact of urbanization on urban climate.

SAR sensors have the advantage of data acquisition during both day and night, regardless of atmospheric weather conditions. Performing the same function as optical images, SAR images can also be used for urban area distribution mapping (Iino *et al.*, 2018) and urban change dynamics analysis (Trianni *et al.*, 2010). Currently, Sentinel-1 images have been used to detect buildings (Koppel *et al.*, 2017), as well as to generate the human settlement layer (Corbane *et al.*, 2018).

SAR images have proven to be a powerful tool for natural hazard risk analysis of urban areas. For example, Envisat Advanced Synthetic Aperture Radar (ASAR) and Sentinel-1 images have been used for flood mapping (Henry *et al.*, 2006; Plank *et al.*, 2017). Due to the high repetition rate of Sentinel-1, it is possible to build up a systematic data acquisition system to detect and monitor flood risk in near real-time. This system allows for the derivation of time-critical disaster information in less than 45 min after a new data set is available on the Sentinel data provision platform, and regularly informs users about the current flood conditions (Twele *et al.*, 2016).

Due to over-exploitation of ground resources, land subsidence affects many cities in the world. Different SAR data sets have been widely used to monitor urban surface deformations. The European Remote Sensing Satellites (ERSs) ERS-1 and ERS-2 acquired a combined database extending over two decades, and can thus be used for monitoring constant urban subsidence over years (Raucoules *et al.*, 2003). The newly launched Sentinel-1 is a reliable SAR source with higher resolution. It has been proven that the data is especially effective in identifying the subsidence behavior as well as the relationship between the occurrence of the subsidence and its main driving factors (Fiaschi *et al.*, 2017; Zhou *et al.*, 2018). Envisat and Sentinel SAR images can also be used to monitor ground deformation caused by earthquakes, landslides, and volcanic activities, and are therefore crucial data sources for cities vulnerable to such natural hazards (Funning *et al.*, 2005; Kyriou and Nikolakopoulos, 2018; Leighton *et al.*, 2013; Solari *et al.*, 2018). Combination of ERS and Envisat data is beneficial for the generation of long-term surface deformation time-series (Bonano *et al.*, 2012).

Hyperspectral remote sensing is an innovative development, which remains unfamiliar to many potential users due to the need of professional knowledge to process the data. Currently, the availability of free hyperspectral data is still limited. The most popular open source is Hyperion

from NASA which is a test instrument designed to demonstrate spaceborne hyperspectral imaging. CHRIS is a similar sensor from ESA and primarily for in-orbit demonstration and evaluation of the new spaceborne hyperspectral technologies. Hyperion has been investigated for extracting impervious surface and its effectiveness has been compared with using multispectral images from Earth Observing-1 (EO-1) Advanced Land Imager. The comparison results show that both data sources produced excellent impervious surface mapping and the hyperspectral image was more powerful in discerning low-albedo surface materials, which has been a major obstacle with multispectral images (Weng *et al.*, 2008). It has also been tested for many other applications such as fractional landscape mapping (Friedel *et al.*, 2018) and automated road extraction (Tiwari *et al.*, 2010).

Airborne Visible/Infrared Imaging Spectrometer (AVIRIS) is a hyperspectral instrument operated on aircraft platforms. The mission has flown across the USA, Canada, and Europe. Even though at moment, only data from 2006 to the present is available, data from 1992 to 2005 are planned to be directly downloadable (Jet Propulsion Laboratory, 2017). AVIRIS imagery has been tested for discriminating vegetation, impervious and soil surfaces, aiming at mapping the composition of urban areas (Golubiewski and Wessman, 2010). AVIRIS can also be used for identification of urban tree species based on their spectral character differences in AVIRIS imagery (Alonzo *et al.*, 2013; Xiao *et al.*, 2004), for the purpose of urban forest management.

The Hyperspectral Mapper (HyMap) instrument, which is an advanced aircraft-mounted commercial hyperspectral sensor, also supports data simulation efforts for the two future hyperspectral satellites from the USA and Australia (Kruse *et al.*, 2000). It is of great interest if this sensor can later be used on satellites to deliver (open) data, despite potentially coarser spatial resolution than commercial data. Nevertheless, this instrument has unique capabilities such as monitoring of mineral generated water pollution (Riaza *et al.*, 2015) and oil contaminated soil detection (Hörig *et al.*, 2001). The excellent performance is due to the fact that the sensor configuration provides both spatially contiguous spectra and spectrally contiguous image of the Earth's surface unavailable from other sources (Kruse *et al.*, 2000).

1.2.2. GIS data

Whereas remote sensing data provides specific measurements of urban areas, GIS data provide direct interpretation of urban objects. For instance, NASA SEDAC aims to support the integration of socioeconomic and earth science data, providing data that can be directly used for social, economic, and environmental analyses. It has a data category specific for the theme of urban areas, including data sets like Global Human Built-up And Settlement Extent from Landsat, Global Population Density Grid Time Series Estimates, Global Urban Heat Island, and Global Grid of Probabilities of Urban Expansion.

Many GIS user communities, organizations, and business sectors built up their online geospatial databases to share their data, information, and knowledge. Usually, the GIS data provision is realized through a web map service, a web feature service, and a download service, to ensure users can display and view the data on-the-fly as maps, graphs, and tables and/or download the data in different formats. Taking ArcGIS Hub Open Data (ArcGIS, 2019) as an example, through the category of web map application, projects like Kitchener's Urban Forest Strategy and Sustainability Walk can be found. The Kitchener's Urban Forest produced several tree

canopy coverage maps to help the city to protect, maintain, and plant the future urban forest. The Sustainability Walk demonstrates the places equipped with energy and resource saving facilities such as green buildings, permeable pavers, solar panels, and green roofs. Even though these maps cannot be downloaded, these projects show creative ideas about sustainable urban development and their implementation in specific cities. Meanwhile, there are also maps that can be downloaded in different formats and further processed with other datasets, such as Urban Sustainability Areas.

In the future, there will be increasingly more open GIS data related to sustainable urban development, since, for example, GEO has several urban sustainability development programs on their work agenda. The Megacities Observation and Monitoring program will provide the datasets for megacities in the world. Global human settlement layers will be generated at various international and national levels. In Europe, the GEO initiative is supported through the Copernicus program, which has adopted an open data policy facilitating the development of downstream services. From its core information services, urban related GIS datasets are listed in the following (Copernicus Programme, 2019a).

- Urban Atlas is a pan-European land use and land cover data for 319 cities with the reference year of 2006 and 693 cities with the reference year of 2012;
- Imperviousness captures the percentage and change of soil sealing for the reference years 2006, 2009, 2012, and 2015;
- European Settlement Map is a spatial raster dataset that maps human settlements in Europe;
- Street Tree Layer includes contiguous rows or a patch of trees covering 500 m2 or more and with a minimum width of 10 m, as well as
- Building Height contains height information generated for core urban areas.

These datasets are from Copernicus Land Monitoring Service's local component that focuses on areas that are prone to specific environmental challenges and problems. In the future, these datasets will be updated to the new reference years. Remarkably, all these datasets are free and easy to download as a data source for urban research.

1.2.3. Citizen science and sensor web

The geospatially enabled online portals build up the interface between geography and citizen science. Volunteered geographic information has great potential for environmental monitoring, especially for environmental agencies which have difficulties in data collection. Volunteered geographic information can also be mined from social media platforms. For instance, through feeding geotagged Flickr and Twitter data into a spatial relational database in the form of geographic coordinates, data can be displayed on a map and analyzed spatially (Connors *et al.*, 2012).

Without professional knowledge, there is a risk that volunteers will fail to collect the suitable data. Short training programs can greatly improve the volunteers' knowledge and the ability to identify research targets, so that volunteer information becomes a sufficient data source. Taking the case of Cartwright *et al*. (2015) as an example, citizen science is used to monitor habitat remains, improve urban ecosystem services, and maintain urban biodiversity.

However, compared to professional monitoring methods, citizen science environmental monitoring often relies on opportunistic, incidental contributions, and could thus suffer from a spatial bias, such as the uneven geographical distribution of sample sites. This bias could be caused by the location, accessibility, size, and general attractiveness of the sites (Jacobs and Zipf, 2017; Millar *et al.*, 2019). However, when the study area is a tourism site, enough data can be collected. For example, Buldrini *et al*. (2015) engaged multiple types of users in monitoring the biodiversity of a wetland which has many tourists, where the data collection was successfully achieved from volunteer contributions on a local scale and during a considerable time span.

Sensor web contribute to urban sustainability development in terms of real-time and *in situ* observations, and thus may be used for real-time alarming. Zheng *et al*. (2012) proposed and tested a method to integrate the hydrological sensor into Web Feature Service for environmental monitoring. Wang and Yuan (2010) explained the challenge of using sensor web for disaster management and provided a solution for multi-purpose disaster management. Hillen *et al*. (2014) demonstrated the use of *in situ* sensors to model people dynamics during major events to support avoiding tragedies. Ali and Choi (2019) reviewed the current application of sensor web for monitoring underground pipeline leakage and sinkhole monitoring.

1.3. Research question

The above review indicates that the application of open geospatial data in sustainable urban research is separated into four fields: remote sensing, GIS, citizen science, and sensor web. Each field developed preferred data sources and its own methods based on the characteristics of these data sources. This results in obvious gaps in the research of urban sustainable development. From an urban planner's point of view, these four fields have no difference in the role they play in urban sustainable development, as they are four different tools which can be used together depending on the requirements of the application. To achieve this aim, fusion is an effective way to integrate all sorts of data aiming at exploiting the full potential of open geospatial data to solve urban issues.

The term "data fusion" has been widely used in many research areas. In the remote sensing context, in the early stage, data fusion mainly takes place between images. Thus, image fusion is defined as "the combination of two or more different images to form a new image by using a certain algorithm" (van Genderen and Pohl, 1994, cited from Pohl and van Genderen, 1998, p. 825). Later, remote sensing data was often combined with other information. In this case, data fusion is recognized as "a process dealing with data and information from multiple sources to achieve refined/improved information for decision making" (Hall and McMullen, 2004, cited from Pohl and van Genderen, 2017, p. 41).

In the GIS community, data fusion is also expressed as data concatenation, meaning the "integration of two or more different data sources, such that the contents of each are accessible in the product" (Longley *et al.*, 2015, p. 123). One of the simple forms of concatenation is a polygon overlay operation. According to geoinformation experts, spatial data fusion usually refers to the synthesis of spatial data from multiple sources to extract meaningful information with respect to a specific application context (Wiemann and Bernard, 2016).

In this thesis, fusion will be conducted between images as well as between multiple data types. Thus a broader definition of data fusion is taken as "a formal framework in which are expressed the means and tools for the alliance of data originating from different sources. It aims at obtaining information of greater quality; the exact definition of 'greater quality' will depend upon the application" (Wald, 1999). From this point of view, data fusion is a work plan and a powerful tool to analyze urban development problems. It could contain, but is not limited to, image fusion, data combination, synthesis, overlay, and integration.

A straightforward benefit of using data fusion is to improve the spatial resolution of images, which can also be called image sharpening technique. As indicated earlier, remote sensing images are the most important source for sustainable urban development research. They have been applied in many topics, including urbanization, urban sprawl, UHI, land cover, and land use change analyses, as well as natural hazards monitoring. However, in recent years, commercial satellite images have been increasingly used to study the same urban issues, such as using IKONOS or QuickBird satellite images for urban feature and urban vegetation extraction (Aytekın *et al.*, 2012; Long and Zhao, 2005; Mayunga *et al.*, 2010; Nichol and Lee, 2005).

The main reason for using commercial satellite images is their higher spatial resolution, which is practically favorable for accurate measurement. Even though some issues can also be solved by using commercial data, manual measurement, or drone surveys, this thesis persists on using open source geospatial data for sustainable urban research, for the following reasons:

- Usage of open geospatial data is in line with the principle of sustainable development. If usage of commercial data is prevailing, a city with a high budget will be encouraged to buy commercial data to build up their spatial information services, whereas a city without such a budget will not be able to provide the same services for its citizens. In this way, the unbalanced development is related to wealth inequality.
- Usage of open geospatial data will promote governments to support data sharing policies, which will avoid duplication of spatial data produced from central and local environmental agencies.
- Usage of open geospatial data encourages more researchers to be involved in the related research topic. In the long term, open data users will increase and push the development of open data initiatives. In this way, a virtuous circle of geospatial data development will be built up, resulting in increasingly more open data sources.
- Usage of open geospatial data could help to promote an open research culture, where scientists recognize the value of transparency, openness, and reproducibility (Nosek *et al.*, 2015).

Open source satellite images such as Landsat 8 thermal images have an original spatial resolution of 100 m, which is not sufficient when analyzing urban areas in detail. Therefore, the spatial resolution needs to be improved. Data fusion techniques, in particular image fusion, have been used to enhance the spatial resolution of images. However, the existing image fusion methods are not suitable for sharpening thermal images. Here, the first main research question of this thesis is raised: *How can the spatial resolution of multi-type remote sensing images be effectively improved?* This main question includes three sub-questions.

- *How to develop a new fusion algorithm which can sharpen all kinds of images, including images from different sensors, having the number of bands from one to hundreds, or covering different spectral regions?* (sub-question 1.1)
- *How does the image sharpen quality of the newly developed algorithm compare to existing image fusion methods, and which assessment methods can be used and why?* (sub-question 1.2)

Even if image resolution can be effectively improved, it is not clear whether the fused images can eventually benefit sustainable urban research. It is worth to know which kind of problems can occur during the implementation in practice. Due to the many aspects of sustainable development, it is impossible to illustrate image fusion performance in every aspect. Therefore, UHI is taken as an application case to present the fusion technique in depth. This leads to the second main research question: *How do image fusion techniques better serve UHI analysis and then sustainable development research?* It is then extended by the following sub-questions:

- *What are the factors that influence the fusion effect during the implementation of the developed image fusion algorithm?* (sub-question 2.1)
- *How does the developed image fusion algorithm improve the performance of open source images in UHI analysis?* (sub-question 2.2)
- *How can the image fusion result benefit sustainable urban development?* (sub-question 2.3)

Even if the improved, higher spatial resolution images are helpful, there are some sustainable development aspects where using just remote sensing images is not sufficient. For urban sustainability research, other obstacles include the analysis of complex issues, particularly those influenced by human activities. Typically, land use related information cannot be directly derived from remote sensing images despite very high spatial resolution, as images themselves can only show land cover differences. This kind of information cannot be extracted by using remote sensing images alone, but needs to be coupled with other existing open source data from GIS, citizen science, or sensor web. In this case, it is necessary to use data fusion instead of image fusion. Taking vacant land as an example, a vacant site could have trees, grass, bare soil, or buildings on the surface. Using remote sensing image classification can group these elements into urban green areas or built-up areas. However, these vacant sites are important resources for urban development and need to be extracted separately. This leads to the last main research question: *How to fuse various geospatial data together to detect a complex urban object for sustainable urban development?* Taking vacant land as the second application case, this research question is studied in four steps, which then forms the following sub-questions:

- *How to define vacant land in a way that makes it possible to be extracted by using geospatial data?* (sub-question 3.1)
- *How to select and use open data sources to include possible vacant land?* (sub-question 3.2)
- *How to make an effective data fusion procedure to detect vacant land?* (sub-question 3.3)
- *How does the data fusion result benefit sustainable urban development?* (sub-question 3.4)

Overall, this thesis takes two application cases to illustrate the data fusion technique and its contribution to sustainability research, as these applications demonstrate the real-world utility of the developed technique. During the data fusion process, use of open source software is emphasized, aiming to show the extent to which geospatial data can be processed on open source platforms. The main objective of this thesis is to show how sustainable urban research can be conducted with free geospatial data, effective data fusion methods, and powerful open source software systems.

1.4. Structure of the thesis

Table 2 provides an overview of the content of each sub-chapter and the corresponding research question. Chapter 2, chapter 3, and chapter 4 respectively refer to the first, second and third main research question and the included sub-questions separately. The overall structure of the thesis follows an order that goes from method development, to its application in practical use, and then to a more complex application case

Table 2 The content of the sub-chapters and the correspondent research questions.

Sub-chapter	Topic	Research question	
2.1	Problems with existing image fusion algorithms	1.1	1
2.2	Development of simplified Ehlers fusion algorithm		
2.3	Fusion quality assessment and discussion	1.2	
3.1	Current research status of the UHI	2.1	2
3.2	Application of simplified Ehlers fusion		
3.3	Image fusion results for UHI analysis	2.2	
3.4	UHI mitigation strategies for sustainable urban development	2.3	
4.1	URBIS vacant land definition	3.1	3
4.2	Revised vacant land definition towards open data fusion		
4.3	Open geospatial data selection	3.2	
4.4	Sites identification using open data fusion	3.3	
4.5	Results of vacant land extraction	3.4	
4.6	Vacant land for sustainable urban development		

UHI: urban heat island. URBIS: URBan land recycling Information services for Sustainable cities.

Chapter 2 focuses on the first main research question. Much effort has been devoted to develop the simplified Ehlers fusion algorithm, since low resolution is a common feature of open source remote sensing images (indicated in Table 1) which generally limit their use in urban areas. The goal of the algorithm is to achieve flexibility for sharpening various types of images regardless of the sensor, platform, and source. Thus, the developed algorithm is tested to sharpen one band thermal images as well as hyperspectral images which have hundreds of bands. Also, the input high and low resolution images are from different sensors and have different spectral coverage. This algorithm paves the way for further open source remote sensing images to be applied to urban areas.

Chapter 3 mainly refers to the second research question. At the beginning of the chapter, it explains the reason why UHI is taken as the first case study and illustrates the current research state. It also explains why the city of Osnabrück, Germany was chosen as the study area. Then, suitable open source thermal images were chosen and the simplified Ehlers fusion was applied. The fused images were subsequently used for UHI analysis. It illustrates how the fused images improve the UHI study and also describes the factors which influenced the fusion effect. To

find the main causes contributing to UHI, thermal images from both day and night were used. At the end, mitigation strategies are proposed which are tailored to the sustainable development of the city.

In chapter 4, an EU funded project was taken as an example to find solutions for the third research question. The chapter starts with revisiting what caused the inaccurate vacant land identification results, and proposes a new definition of vacant land in a way that is possible to be extracted by using open geospatial data. Then, it demonstrates the data collection process and the roles the data play in site extraction. Afterward, the developed fusion framework and fusion procedure based on the properties of the selected data is presented. Finally, the extracted vacant land parcels are presented and validated with ground truth images. This chapter closes with the role that vacant land plays in social, economic, and environmental sustainability.

Chapter 5 summarizes the work carried out in this thesis, and answers the posed research questions. It draws a conclusion about how to conduct data fusion in the image, feature, and decision levels, as well as how data fusion can be further beneficial for sustainable urban development. It also points out the potential of open source software, to make geospatial data fusion more accessible to open source users. At the end, it lists some future work which could lead to wider application of open geospatial data.

2. Simplified Ehlers fusion

Open source remote sensing images are powerful but often have a coarse spatial resolution, which makes it difficult to apply these datasets to research urban sustainable development issues. This chapter focuses on the data fusion algorithms which aim at image resolution improvement.

2.1. Experiment on classic image fusion methods

In the usage of optical remote sensing technology, satellite sensors often generate a panchromatic band together with multispectral bands which include near-infrared (NIR) and visible bands. Visible bands consist of three bands—red, green, and blue (RGB)—which show the land in colors that correspond to their appearance to human eyes and can be easily interpreted by the human brain. The image fusion technique uses the high-resolution panchromatic band to improve the resolution of the multispectral bands, resulting in a color image with better spatial resolution. In this way, the panchromatic band is used to sharpen the low-resolution multispectral bands. This technique is called pan-sharpening. Nearly every optical satellite dataset includes both multispectral bands and a single panchromatic band.

Pohl and van Genderen (2017, chap. 3) provide a comprehensive picture of pan-sharpen algorithms. There are more than twenty possible methods that have been developed. Among these algorithms, principal component (PC), Intensity-Hue-Saturation (IHS), Gram-Schmidt, High-Pass Filter (HPF), Wavelet, Brovey, and Ehlers fusion have been applied as image processing tools in the most commonly used software. Part of them have also been integrated into open source geospatial application platforms such as QGIS and GRASS GIS. Commonly, open geospatial data users prefer to implement the data application on an open source platform. Since this thesis emphasizes open source data, the algorithms which are available in open source software are discussed in the following:

- PC: The algorithm first transforms the multispectral image into several components using PC transformation. Then the first component is replaced by the panchromatic image. Afterward, the improved first component together with the other components are transformed back into color space. This method assumes that the first component contains the information that is common to all bands and is an equivalent substitution of panchromatic data.
- IHS: This method applies an IHS color transformation to the three RGB bands. Then the intensity is replaced with the panchromatic image. Afterward, the inverse IHS transformation returns the fused image. In the beginning, this method was limited to pan-sharpening RGB three-band images. Later, it has been adapted to multispectral images.
- Gram-Schmidt: The algorithm is based on the Gram-Schmidt orthogonalization. It works in a similar way as PC does. Firstly, a simulated pan-band is created using a weighted average of the multispectral bands. Then, each band is taken as a vector and de-correlated so that all of them are orthogonal. The first vector, the simulated pan-band, is eventually replaced by the panchromatic band. In the end, the fused image is returned by an inverse transformation.
- HPF: The HPF here works in the spatial domain, which is different from the high-pass filter in the frequency domain. It assumes that pixel averaging in a neighborhood could

cause image blurring, while pixel differentiation can induce sharpening. The method runs a moving window pixel-by-pixel all over the high-resolution image. At each point, the moving window contains an operator whose strength is proportional to the degree of intensity discontinuity of the image. By differentiation, the operator enhances the edges and noise as well as minimizes slowly varying intensities. In this way, the high-resolution image is high-pass filtered. The filtered image is used to inject into and thus enrich the low-resolution image.

- Brovey: The algorithm first resamples the multispectral image to the spatial resolution of the panchromatic image. Then, each band is multiplied by a ratio of the panchromatic data divided by the sum of the RGB bands. This method works based on the assumption that the panchromatic band contains the information that is common to multispectral bands.

In conclusion, the above-mentioned pan-sharpening techniques focus on injecting the spatial information of the panchromatic image into a multispectral image. This information is taken as the first component by PC and first vector by Gram-Schmidt and is then merged into a resultant image after fusion. The injected spatial information will not introduce errors but enhance the images because the panchromatic band covers the spectral range of the RGB bands, which means spatial objects caught up by RGB bands are present in panchromatic bands with more details.

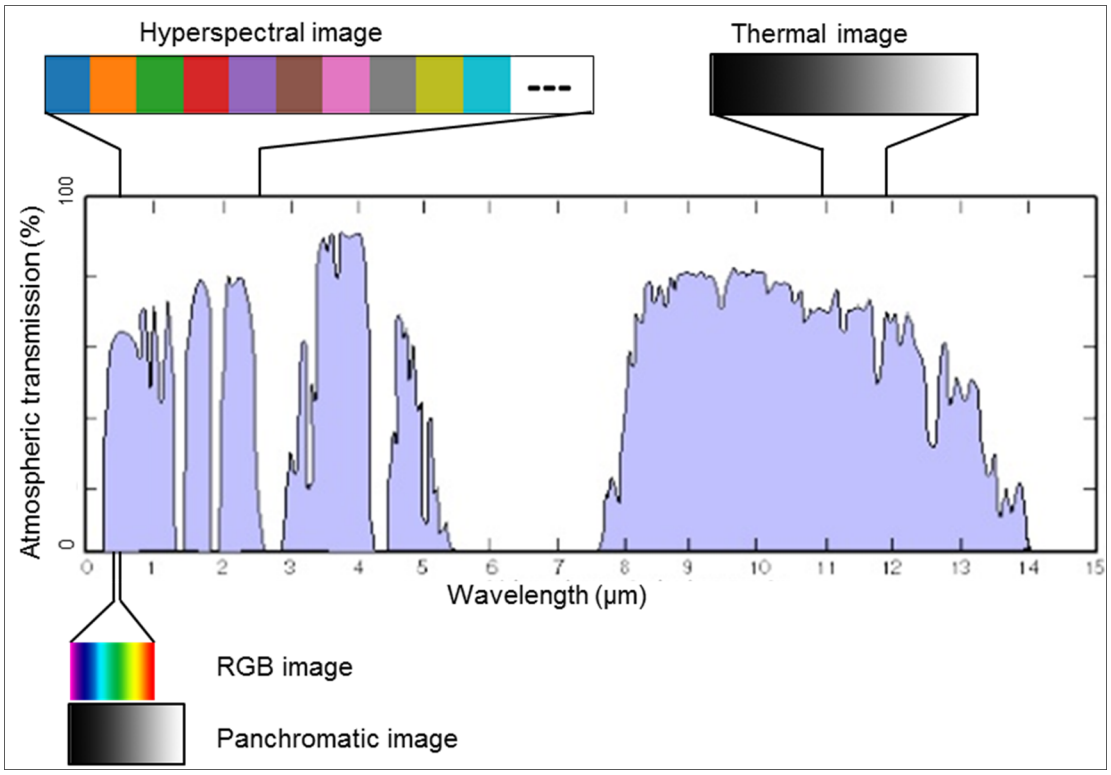

Figure 1 Atmospheric window and the wavelength ranges for remote sensing images. RGB: red, green, and blue.

Figure 1 shows the atmospheric window which allows remote sensing images to be captured in specific wavelength ranges. The panchromatic images often cover the spectral regions of RGB and NIR bands. Obviously, the spectral range of the panchromatic image is wider than the RGB image. But the panchromatic band does not cover the spectral range of thermal bands and only

has partial spectral overlap with hyperspectral bands. The mentioned algorithm works based on the assumption that the information appearing in high-resolution images also exists in low-resolution images. However, this can only be correct when using panchromatic and RGB band bundles but not when thermal images and hyperspectral images are involved. As remote sensing technology advances, high-resolution images are not limited to panchromatic images, and images with high quality such as aerial photos can be used as source data. The target image is also not always a multispectral image, but another type of a lower-resolution image such as a thermal or a hyperspectral image. Then, these classic algorithms face difficulties with the fusion between any high-resolution image and low-resolution image.

An experiment was carried out with these classic algorithms. A Landsat 8 thermal band was taken as the sharpening target and the panchromatic band in the same band bundle was taken as high-resolution image input. Firstly, it was found that it was impossible to directly apply the above-mentioned pan-sharpen algorithms in the remote sensing software, as RGB bands are needed to be specified as input. An indirect way is to stack thermal bands with RGB bands together and apply the pan-sharpen method to all bands, and then the thermal bands are extracted. However, even in this way, Gram-Schmidt and IHS produce empty images while Brovey and PC return poor results. Figure 2 shows part of the fusion results which is a close look at a city core. Brovey keeps the information from the panchromatic image but not the thermal image. The PC method produces an unsatisfactory pan-sharpen result due to the unclear spatial improvement. Only HPF provides a reasonable outcome. But the spatial improvement is achieved by a moving window going through the entire image without distinguishing between urban and non-urban areas. By the nature of the algorithm, it cannot produce spatial enhancement matching particular urban features.

A multi-sensor oriented data fusion approach could potentially overcome the limits of these classic algorithms. Typically, the focus has been on a general image fusion framework. This kind of framework can be first used to systematically classify, compare, and evaluate existing image fusion methods, then to analyze the cause of imperfect fusion performance on the theoretical level. In the end, based on these findings, the goal is to further develop a more advanced algorithm for multi-sensor data fusion.

Wang *et* a*l*. (2005) started from the acquisition of the pixel values of an image, then further examined the change of the values during image processing, finally summarizing the fusion procedure with a general image fusion (GIF) framework. Within this framework, fusion methods such as IHS, Brovey, PC, and HPF are simply the particular cases of the GIF method. In the end, through comparison, the authors claimed that the images produced by a multi-resolution analysis-based intensity modulation method are closest to the ideal multi-sensor data fusion result. However, there is no source code or software available to test this method. Based on the equations and descriptions of the method, the author of this thesis assumes that in principle, it makes use of the HPF in the spatial domain and the filter is modulated according to the ratio of the spatial resolutions of input images. If this is the case, similar to HPF, it will enhance the image throughout the entire image regardless of the difference between homogenous vegetation area and heterogeneous urban area.

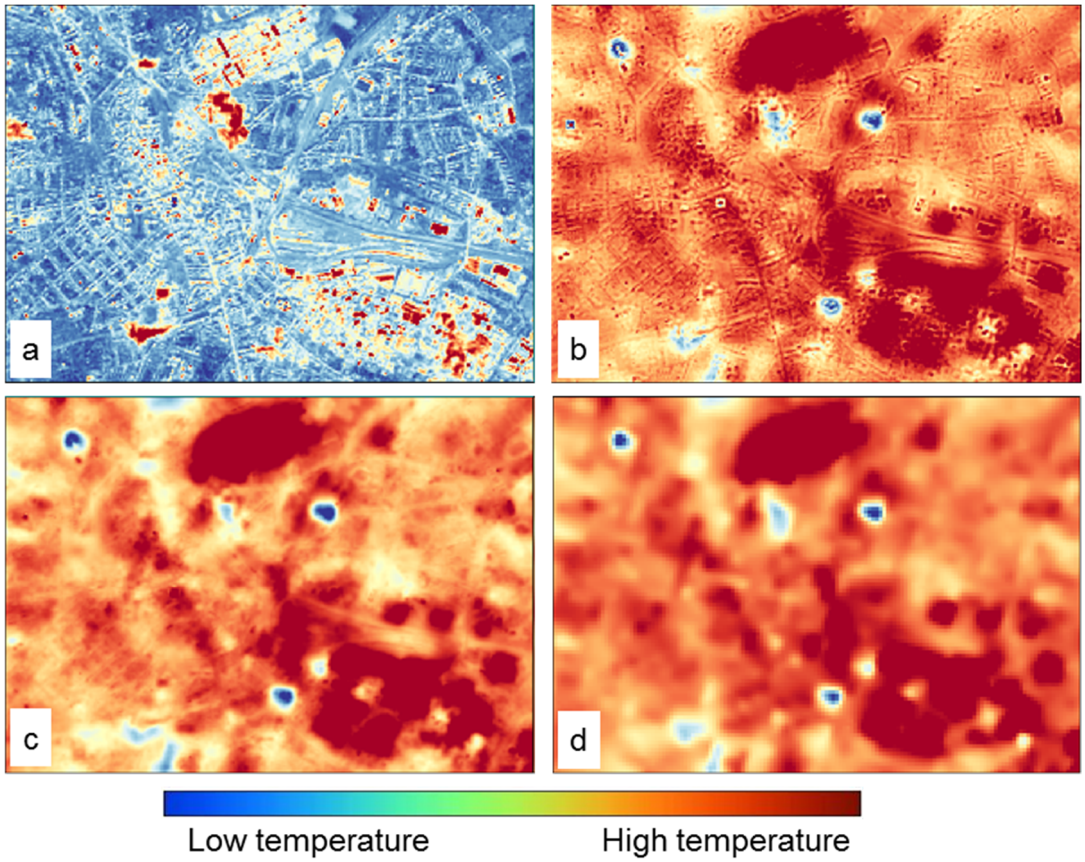

Figure 2 Pan-sharpened thermal band using classic image fusion methods: (a) Brovey, (b) HPF, (c) PC, and (d) original thermal image. All images were originally in grayscale but shown as a temperature color map. HPF: high-pass filter. PC: principal component.

Palubinskas and Reinartz (2011) took a similar approach but with a signal processing view and proposed a general framework for image fusion (GFF). Several known fusion methods can be presented using this framework. In the end, the authors proposed their GFF spectral fusion method, which was tested in the fusion between optical and optical images, as well as between optical and radar images. However, it is not well-documented how GFF was realized. The authors claimed that "GFF method performs image fusion in Fourier domain", but at the same time, the method also "avoids time-consuming Fast Fourier Transform computations" (Palubinskas, 2013). From the view of the author of this thesis, it shares many similarities with the HPF technique in the spatial domain.

Thomas *et al*. (2008) categorized the existing fusion methods from the physics perspective on remote sensing. The weaknesses of fusion methods are confronted with physical constraints. The authors suggested a new concept which offers a reliable framework for further development. However, the implementation of the method has not been presented in practice.

In the context of the application of open geospatial data, it is necessary to make full use of the available data sources. Therefore, the algorithm should be flexible with the input and target images, in terms of the different spectral cover range, as well as the number of bands for the target image. For example, if using a Landsat 8 panchromatic image to sharpen the thermal image, the target image has only one band; if using an aerial photo to sharpen the hyperspectral image, the high-resolution image and the low-resolution image have only a few overlaps on the spectral scale.

As the experiment shows, the classic algorithms cannot be directly applied to one band alone. Even after adding the target image together with RGB bands, the pan-sharpened results are not satisfactory. The above-mentioned general fusion frameworks are also not suitable due to their unavailability, uncertainty, or immaturity. Therefore, a new algorithm, simplified Ehlers fusion, was developed by the author and presented in this thesis.

In the above experiment, the used panchromatic image has a 15 m resolution and the thermal image has an original 100 m resolution. Due to the coarse resolution, even with a magnified view to the city core, the urban features are still difficult to interpret. This brings many inconveniences for visual evaluation of the fusion effect. For the efficient development of the new algorithm, in the following subchapter images with a very high resolution are used. However, in practical use cases, only open geospatial data were applied (see chapter 3 and chapter 4).

2.2. Simplified Ehlers fusion

Ehlers fusion was taken into consideration for three main reasons: firstly, it has been tested for multi-sensor and multi-temporal data fusion. Secondly, it results in outstanding pan-sharpen outcomes compared to multispectral images (Ehlers *et al.*, 2010; Jawak and Luis, 2013; Yuhendra *et al.*, 2012). Lastly, it is well known as an image processing tool integrated into the ERDAS IMAGINE software, which is one of the most commonly used software for the remote sensing research community (Gooch *et al.*, 1999; Kovářík, 2011; Long and Srihar, 2004). The image enhancement takes place in the image frequency domain after the Fourier transform. The transformation between RGB bands and IHS is additionally applied to manipulate images with multiple bands. To adjust the algorithm to be suitable for sharpening a more general image target, the IHS transformation is avoided. This is why the new algorithm is named *simplified Ehlers fusion*. Instead of IHS transformation, the fusion loop can move band by band for multi-band images. In this way, the computing time could increase. However, this is no longer an obstacle as modern computers capable of parallel computing can process such workloads. In the following, necessary information about images in the frequency domain are introduced, before explaining the newly developed algorithm.

2.2.1. Fast Fourier transform

A fast Fourier transform (FFT) fully converts an image from the spatial to the frequency domain. The FFT method preserves all original data (Harris Geospatial Solutions, 2019). In contrast to the spatial domain, an image in the frequency domain cannot be perceived directly, as illustrated in Figure 3 which is the power spectrum of an optical image in the 3D frequency domain. Usually, there are no direct associations between specific components of an image and its transform. Only some general statements can be made about the relationship between the frequency and spatial features of an image. Low frequencies correspond to the slowly varying intensity components of an image. Low frequencies contain the most information because they determine the overall shape or pattern in the image. In the same way, high frequencies correspond to fast intensity changes in the image, which are the edges of objects and other components characterized by abrupt changes in intensity (Gonzalez and Woods, 2007). In Figure 3, the large peak in the center represents the lowest frequency of the image, which is the average intensity value. As the distance from the center increases, the magnitude of frequency

increases. High frequencies are located at the borders and correspond to small scale variations in the image. They provide more detail in the image but can contain more noise.

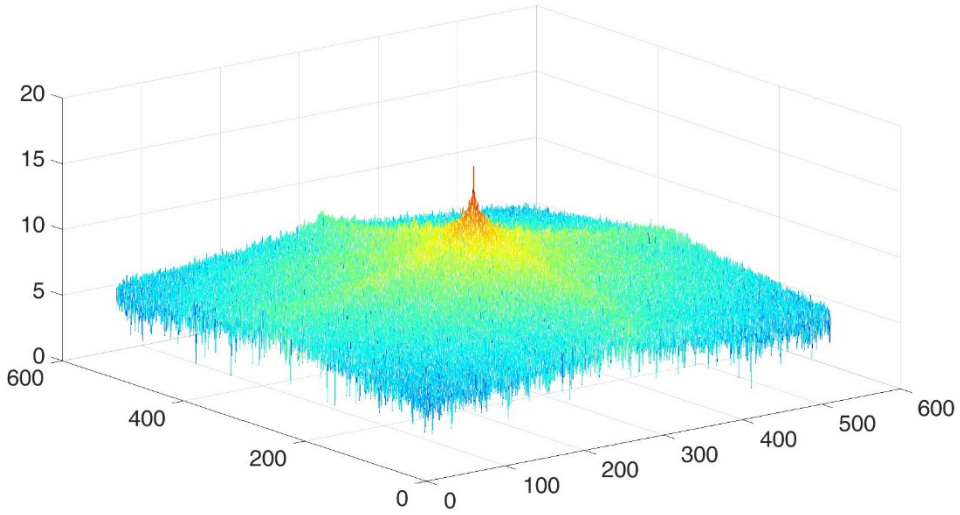

Figure 3 Power spectrum of an image with 512 × 512 pixels in 3D frequency domain (produced with MATLAB)

Commonly, images in the frequency domain are often shown by Fourier spectrum in the 2D view (Figure 4), where the high frequency and low frequency is shown in gradual greyscale. Low frequencies are near the center while high frequencies are away from the center. The linear features or edges (such as the outline of buildings) from the original image are represented as high frequencies. After an image is transformed into the frequency domain, various filters can be applied. In the pan-sharpening context, the goal of using a filter is to rearrange those high and low frequencies, by extracting high frequencies from high-resolution images and low frequencies from low-resolution images, in order to integrate them together.

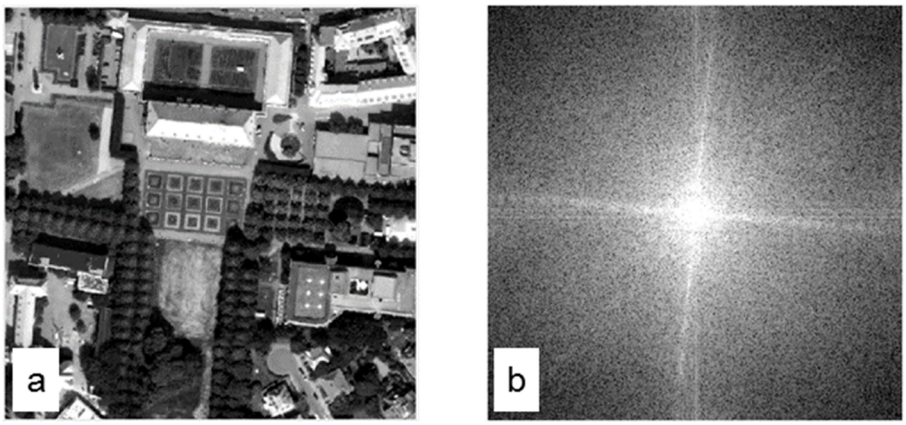

Figure 4 (a) A grayscale optical image and (b) the 2D power spectrum of this image after a Fourier transform.

These can be further illustrated by Figure 5. The spatial information such as edges is extracted from a high-resolution image. Meanwhile, the spectral information (color) is taken out from a low-resolution image. In the end, the separated spatial information and spectral information are added together to get the fused image. In this way, it reaches the ideal goal of pan-sharpening—the spatial details of the low-resolution image are enriched, and at the same time, its color is only minimally changed.

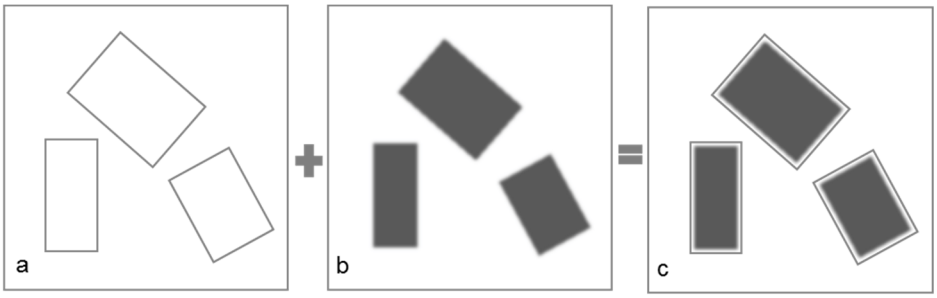

Figure 5 Ideal spatial enhancement procedure: (a) source image for spatial information input, (b) target image where spectral information should be preserved, and (c) the ideal pan-sharpened result (adapted from Xu and Ehlers, 2017).

2.2.2. Image filtering[1]

Image filtering in the frequency domain has been widely used in image processing for the purpose of image smoothing, reducing periodic noise, image sharpening etc. (Gonzalez and Woods, 2007). The major advantage of using frequency filters is that particular frequencies can be removed or preserved according to the spatial features within the images, which is not possible to realize with the spatial filters. As an FFT separates an image into its various frequency components, low and high frequencies can be manipulated independently. A low-pass filter passes all frequencies within a circle of radius D_0 from the origin and cuts off all frequencies outside this circle. The filter is a function whose variable is the distance between a point (u, v) and the center of the frequency rectangle. Within this circle, its value is 1 or approaching 1 whereas outside is 0. When displaying the filter as a gray scale image, black is 0 and white is 1. The low-pass filtering is realized by multiplying this function with the image frequencies. The cut-off frequency is also named as the size of the filter.

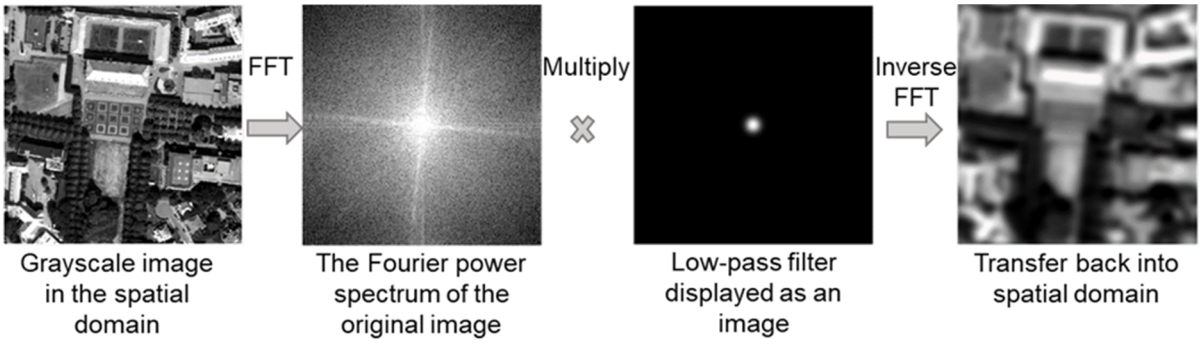

Figure 6 Image filtering procedure with a fast Fourier transform. FFT: fast Fourier transform.

The filtering procedure is demonstrated in Figure 6. A gray image with 512 × 512 pixels is firstly transferred into the frequency domain. Then the frequencies are multiplied by a low-pass filter. Afterward, the filtered frequencies are transferred back into the spatial domain. Because a low-pass filter is applied, and the features inside the image have lost their edges and spatial details. Here, the low-pass filter is taken as an example to illustrate the general filtering

[1] For this section, a similar filter test was carried out as presented in Xu and Ehlers (2017). While some of the following figures might look similar to the figures in the referred study, they are based on different data from the same data source. In the previous study, the high resolution image was the average intensity of RGB bands after using IHS transform; for the experiment presented in this section, the high resolution image is the red band without any transformation. They look similar because both of them are presented in grayscale. The filter test with new input data is still necessary and the testing results are present here.

procedure. The type of the filter can be replaced by others, such as high-pass or band-pass filter, and the filtering procedure follows the same order. In the following test, the image size was always kept as 512 × 512 pixels.

2.2.2.1. Filter types

Three different filter types are commonly used: Gaussian, Butterworth and Ideal filter. These are non-directional filters in the frequency domain. A directional filter is commonly used for edge detection. It is realized in the spatial domain and beyond the scope of this thesis. The three non-directional filters are realized by the following equations (Gonzalez and Woods, 2007), where equation (1) represents the Ideal low pass filter function, (2) the Butterworth low pass filter function, and (3) the Gaussian low pass filter function:

$$H(u,v) = \begin{cases} 1 & if\ D(u,v) \le D_0 \\ 0 & if\ D(u,v) > D_0 \end{cases} \quad (1)$$

$$H(u,v) = \frac{1}{1 + \left[\frac{D(u,v)}{D_0}\right]^{2n}} \quad (2)$$

$$H(u,v) = e^{\frac{-D(u,v)^2}{2D_0^2}} \quad (3)$$

where D_0 = cut-off frequency
n = order of the Butterworth filter
H (u, v) = filter function
D (u, v) = distance between a point (u, v) in the frequency domain and the center of the frequency rectangle

Corresponding to each low-pass filter function, there is a high-pass filter function. A high-pass filter is the opposite of the low-pass filter, and therefore its function can be generally expressed as:

$$H_{HP}(u,v) = 1 - H_{LP}(u,v) \quad (4)$$

where H_{LP} = low-pass filter
H_{HP} = high-pass filter

High-pass filter can also be realized by Ideal, Butterworth, and Gaussian filter functions. Parallel to the three types of high-pass filters, three band-pass filter can also be used to pass frequencies. The detailed functions of each type of band-pass filter are listed in the following, (5) Ideal, (6) Butterworth, and (7) Gaussian band-pass filter functions:

$$H(u,v) = \begin{cases} 1 & if\ D_0 - {}^{W}/_{2} \le D \le D_0 + {}^{W}/_{2} \\ 0 & otherwise \end{cases} \quad (5)$$

$$H(u,v) = 1 - \frac{1}{1 + \left[\frac{D \times W}{D^2 - D_0^2}\right]^{2n}} \quad (6)$$

$$H(u,v) = e^{-\left(\frac{D^2 - D_0^2}{D \times W}\right)^2} \quad (7)$$

where D_0 = cut-off frequency
n = order of the Butterworth filter
W = width of the band filter
H (u, v) = filter function
D = simplified notation of D (u, v)

The different filter types have different filtering effects on the image when high-pass filter or band-pass filter is used. The Ideal frequency pass filter has a sharp discontinuity that provides a clear cut-off between passed and filtered frequencies with the disadvantage of introducing ringing artifacts. In Gaussian and Butterworth filters, there is a smooth transition in blurring as the cut-off frequencies increase. The Butterworth function has an additional variable which is the order of the function. The higher the value of the order, the more ringing effects it will produce on the image. By adjusting the order of n, the Butterworth filter can achieve slightly smoother results than the Gaussian filter (Gonzalez and Woods, 2007).

Figure 7 shows the results of three types of high-pass filters applied to an image. With the same filter size, the Ideal filter has obvious ringing artifacts and the other two show much smoother filtering results.

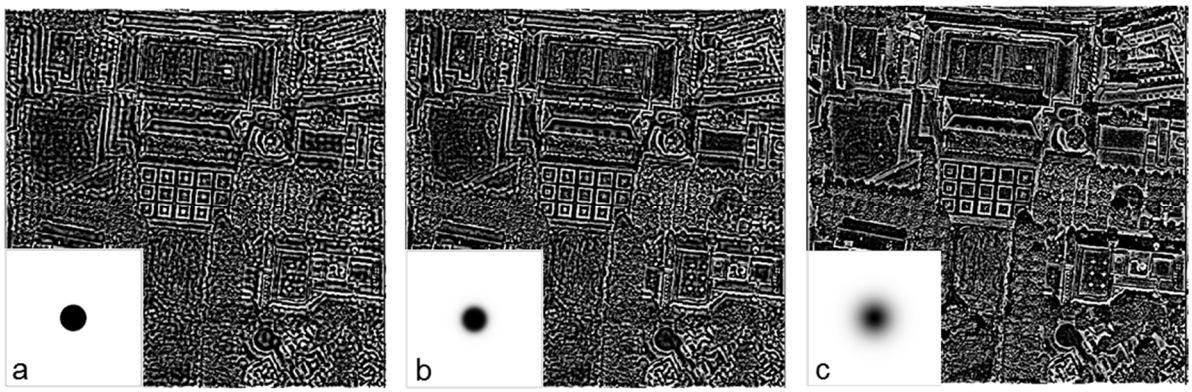

Figure 7 High-pass filtering effects with (a) Ideal (b) Butterworth, and (c) Gaussian high-pass filter. All three filters have a cut-off frequency of 100 (adapted from Xu and Ehlers, 2017).

Figure 8 shows the results produced by the three types of band-pass filters. In order to take a close look at the filtering effect, a garden area of the image is selected and presented in a magnified view (Figure 8a). Figure 8b, Figure 8c, and Figure 8d are the images after Ideal, Butterworth, and Gaussian filters were applied respectively. Similar to high-/low-pass filter, with the same filter size setting, the Ideal band-pass filter generates ringing artifacts. The Butterworth band-pass filter produces some artifacts, and the Gaussian filter produced the optimal result.

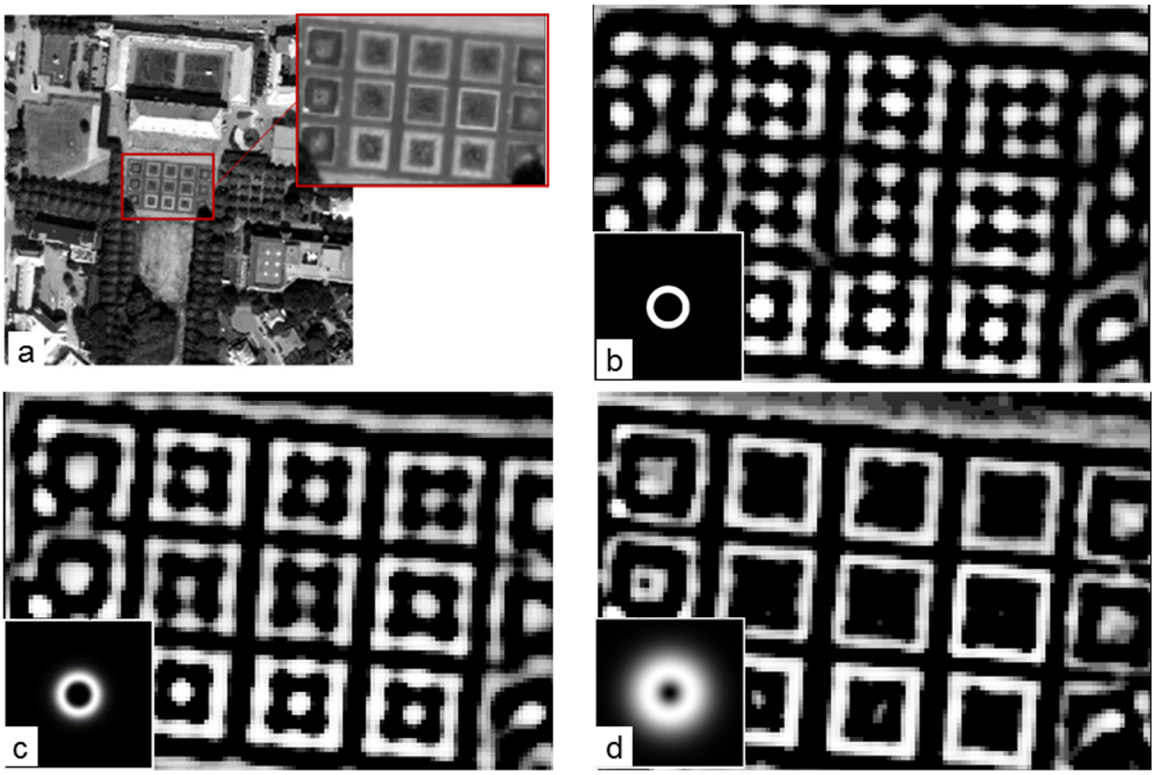

Figure 8 The garden area of the image and the filtered results: (a) original image, (b) result after using Ideal, (c) Butterworth, and (d) Gaussian band-pass filter.

Due to the filtering effect, in the subsection 2.2.2.2, the Ideal filter is discarded and not taken into consideration any more. The Butterworth filter is also intentionally ignored because it has more variables that need to be adjusted, and it achieves no better fusion effect compared to the Gaussian filter. The Gaussian filter is chosen as the test filter in order to further study the parameters which could improve the filtering effect.

In addition to high-pass filter, band-pass filter is emphasized here because a band-pass filter is a selective filter, which operates over a specific range of frequencies. While a high-pass filter only allows setting a lower limit for cut-off frequency, a band-pass filter can define both a lower and an upper limit. This means for the purposes of pan-sharpening, a band-pass filter can precisely assign which frequencies from the high-resolution image need to be added to the low-resolution image. As the lower and upper limit are adjustable, a band-pass filter can be adapted to exactly match urban features. Figure 9 shows the comparison between high-pass filter and band-pass filter for this purpose. To examine the filtering effects closely, the garden area in Figure 8a is presented in a magnified view. The garden area was built up in the way that the vegetation is enclosed by nine concrete frames (the nine squares in the middle of Figure 8a). In the high-pass filter produced image (Figure 9a), there are some white spots inside the nine frames. If using this image as input to sharpen the low-resolution image, these white spots are non-zero values and will therefore change the spectral values of the low-resolution image. The goal of using a band-pass filter is to extract only the outline of the garden frame while the inside vegetation should be left out. Figure 9b shows the perfect filtering result which preserves the edges of the garden and keeps the inside completely black (equal to the value of 0). As an ideal image sharpening algorithm it should enhance edges without changing the spectral information in the homogenous vegetation area (Ehlers *et al.*, 2010). The garden on the image represents the homogenous area by the vegetation inside the concrete frame. From this point of view,

Figure 9b is a cleaner input image than Figure 9a for spatial resolution enhancement. It extracts the outline of the garden area while generating no values for the inside vegetation part, so the low-resolution image will be spatially enhanced, and at the same time, the spectral information will not be altered despite this input.

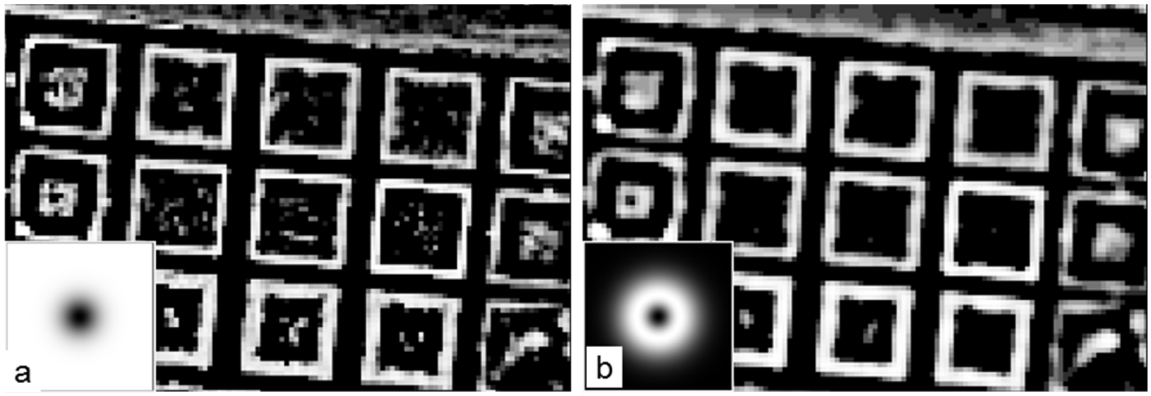

Figure 9 Comparison of filtering effect between (a) high-pass filter and (b) band-pass filter.

Besides computing the band-pass filter by the equations (5), (6), and (7), there is another way to realize band-pass filters. These filters directly calculated from the equations are named as *direct band-pass* filters. On the contrary, an *indirect band-pass* filter can be produced by the multiplication of a high-pass filter and a low-pass filter. In this case, the cut-off frequency of the high-pass filter must be lower than the cut-off frequency of the low-pass filter, so that there is a gap between the two cut-off frequency limits. That is why the size of the high-pass filter must be smaller than the size of the low-pass filter, so that there is a gap between the inner circle and outer circle. For instance, a high-pass filter with cut-off frequency of 100 (Figure 10a) was multiplied by a low-pass filter with cut-off frequency of 150 (Figure 10b). Then, an indirect band-pass filter is formed (Figure 10c).

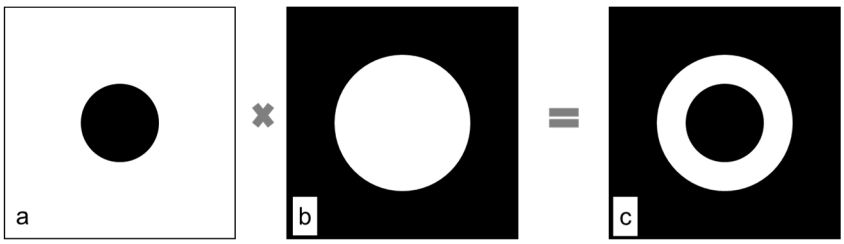

Figure 10 Realization of an ideal band-pass filter : multiplying a (a) high-pass filter with a (b) low-pass filter results in the (c) ideal band-pass filter. The cut-off size of the low-pass and high-pass filter are 150 and 100 respectively.

To compare the filtering effect between indirect and direct band-pass filters, both types of band-pass filters were applied to the image. From the filtered results, a building area and the garden area were selected and presented in a magnified view (Figure 11). The indirect filter was formed in a way of multiplying a high-pass filter with a size of 100 by a low-pass filter with a size of 150 (Figure 11a). The direct band-pass filter was set with a radius of 100 and a width of 100 (Figure 11b). Both filters are Gaussian filters. In this case, two filters produce a similar filtering effect, even though the width of the direct and indirect band-pass filters are 50 and 100 respectively. This is because the indirect filter produces a bigger blurring area than the direct filter. This bigger blurring area makes the width of the band filter bigger than its actual size. As

shown in Figure 11b, the filter is out of the image frame, even though the outer circle is 150 which is less than half the size of the whole image (512 × 512 pixels). In contrast to an indirect band-pass filter, the direct band-pass filter has a more precise bandwidth; the radius and width of the band are proportional to the image size.

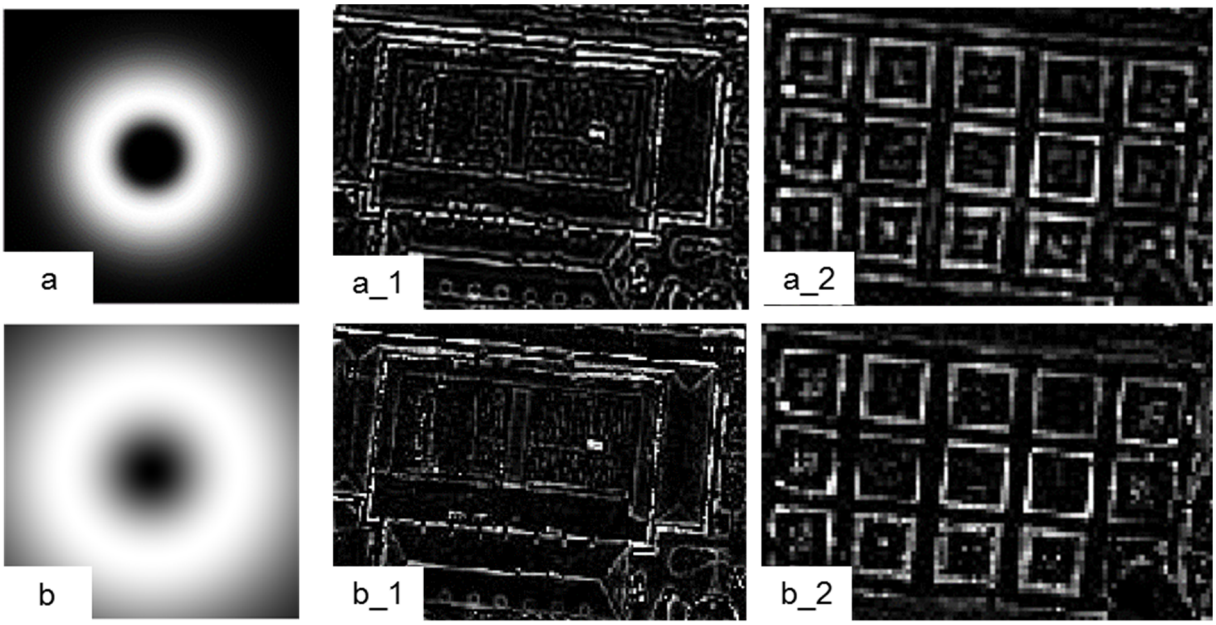

Figure 11 Comparison between a (a) direct and an (b) indirect band-pass filter, (a_1, a_2) two magnified areas from the direct band-pass filtered results and (b_1, b_2) two magnified areas from the indirect band-pass filtered results.

2.2.2.2. Filter size

The cut-off frequency or filter size of a filter can change the filtering effect completely. For a high-pass filter, if the filter size is too small, a high-pass filter will allow even low frequencies to pass through. In this way, the function of the high-pass filter fails because the low frequencies also appear in the filtered image. Figure 12a shows the results when a high-pass filter with cut-off frequency of 10 and 50 is applied respectively. Since the low-frequency concentrated area is bigger than 10, the low frequencies pass through even though the high-pass filter is applied. The passed through low frequencies show up on the filtered image as color information, such as the buildings on the bottom left corner presenting a lighter color than the trees (Figure 12a_1). Figure 12a_2 shows the filtering effect when increasing the cut-off frequency to 50. Obviously, the filtered image presents only the outline of the buildings and no color difference.

The principle works the same on the low-pass filter. If the cut-off frequency is too high, meaning the filter size is too big, then the low-pass filter will allow high frequencies to pass through. Figure 12b shows the results of filtering using a low-pass filter with a size of 10 and 50 respectively. When the cut-off frequency is 10, most of the low frequencies pass through. When the cut-off frequency is 50, the filter passes a portion of high frequencies through, even though it is a low-pass filter. The filtered image shows spatial details. In brief, the size of the filter is crucial as it determines whether a filter loses its function.

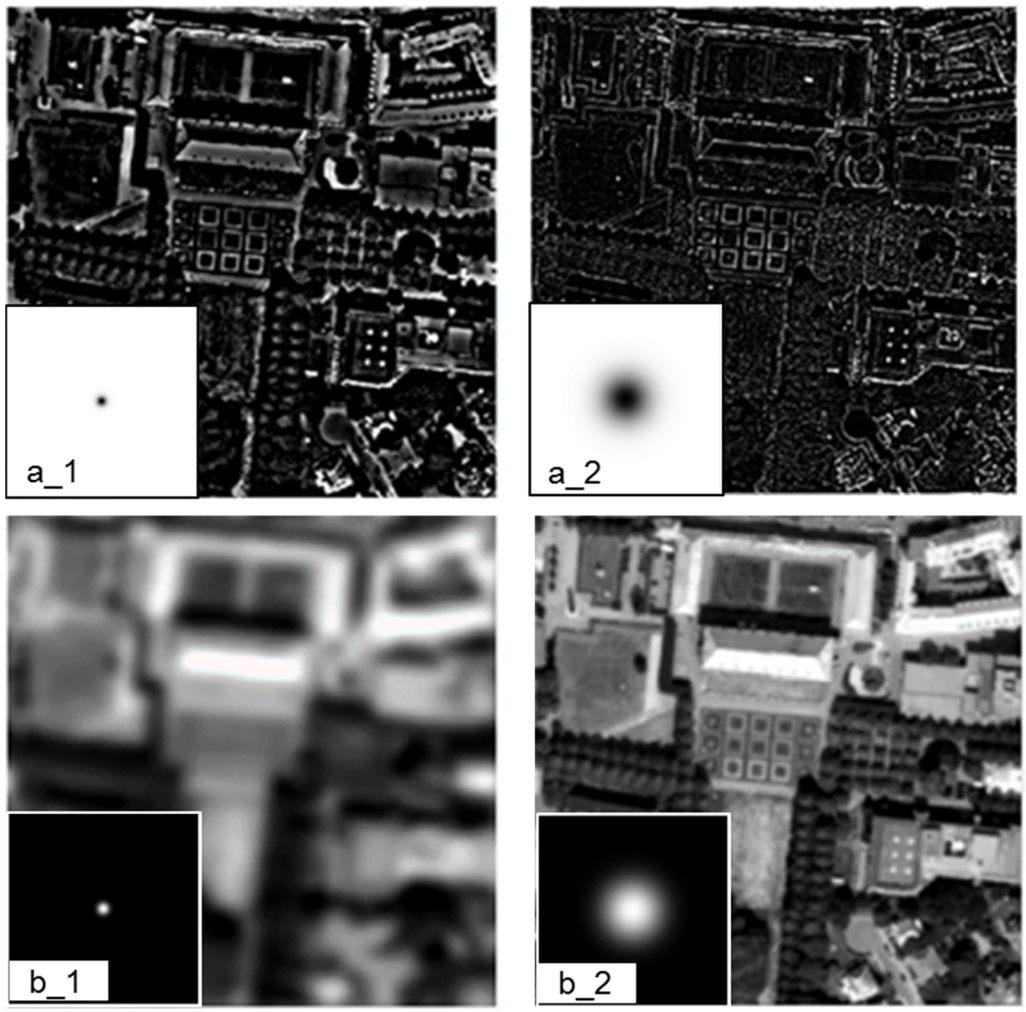

Figure 12 Influence of filter size on filtering effect: when high-pass filter with cut-off frequency of (a_1) 10 and (a_2) 50 are applied; when low-pass filter with cut-off frequency of (b_1) 10 and (b_2) 50 are applied.

For band-pass filter, the influence of the filter size on the filtering effect depends on two parameters. Because the band-pass filter has a “doughnut” shape, its size is determined by the inner and outer radius. Figure 13a shows the filtered image when the inner radius and width is 150 and 50 respectively. The result shows a blocky effect. This means when the inner radius is big and the width is small, it tends to produce blocky images. To reduce the blocky effect on the filtered image, the inner radius was reduced to 100 and the width increased to 100. The filtered result is illustrated by Figure 13b, which shows a much smoother image than before. To know if this setting produces the best result, both the inner radius and width are further adjusted to 50. Figure 13c shows the filtered result, which is also smooth, and no blocky effect appears. Compared to Figure 13b, the linear features in Figure 13c are in bold, which means the setting of the filter highlights these linear features.

In this subsection, all parameters which could influence the filtering effect were investigated. The filter selection procedure is summarized by the following statements:

- The basic filter type first needs to be fixed. The options include Ideal, Butterworth or Gaussian, where Gaussian is recommended.

- The next step is to choose the cut-off frequency of the low-pass filter. The exact value can be decided by trial and error in order to keep the spectral pattern and skip spatial details.
- After the size of the low-pass filter is fixed, it needs to be decided whether a high-pass filter or a band-pass filter should be used. For non-professional users, it might be easier to apply the high-pass filter. However, using a band-pass filter has the advantage of providing more precise spatial information. It is more challenging to use a band-pass filter, because there are two variables that need to be adjusted at the same time.
- Once it is decided to use a band-pass filter, another decision needs to be made between using a direct or indirect band-pass filter. A direct band- pass filter is recommended because it is more controllable.
- The last step is to set up the size of the high-pass or band-pass filter. The basic rule is that the size of the high-pass or the inner radius of the band-pass filter should not be bigger than the size of the low-pass filter. Furthermore, if a band-pass filter has been chosen, then the width should not be smaller than the inner radius. Otherwise, artifacts may appear.

It is also worth to mention that the filter size is not proportional to the size of the image. That is to say, even if 50 is the best cut-off frequency for the image with a size of 255, it does not mean that 100 is a suitable setting for the image with a size of 510.

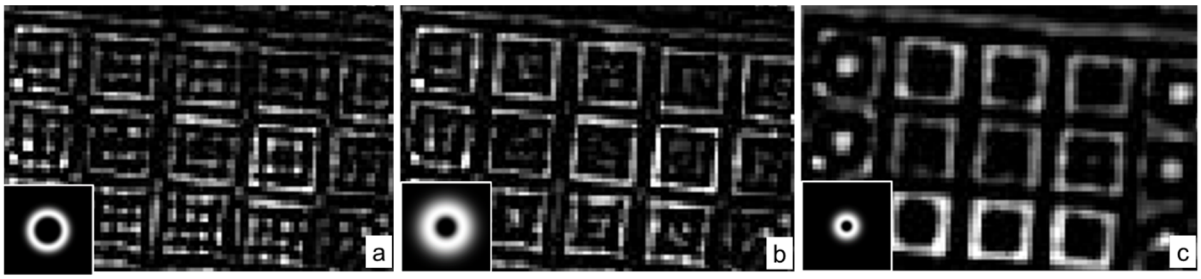

Figure 13 Band-pass filtered images when inner radius and width are (a) 150 and 50, (b) 100 and 100, and (c) 50 and 50, respectively.

2.2.3. Simplified Ehlers fusion workflow

The Ehlers fusion procedure includes the following: As a first step, the multispectral image is transformed into an IHS space. Afterward, the intensity component is further transformed into the frequency domain using an FFT. At the end, the intensity component is low-pass filtered while the pan image is high-pass filtered. The filtered frequencies are added together and then the reverse FFT is applied to obtain the new intensity. In the end, this enhanced intensity is transformed back into RGB space.

In brief, Ehlers fusion consists of a two-step transformation: IHS and FFT. The IHS transformation was built upon the perfect matching between RGB color space and IHS space. This perfect matching does not exist anymore when the target image has no RGB bands or hundreds of bands. Therefore, the intensity transformation can be omitted.

Simplified Ehlers fusion skips the IHS transformation and directly processes the image in the frequency domain. Therefore, the algorithm is more flexible with the number of bands. The fusion objective can be a one band image or a hyperspectral image with hundreds of bands.

Moreover, the algorithm further optimizes the procedure so that the image with bands of different spatial resolutions can also be fused at once. This will benefit the fusion of satellite images such as Landsat 8, which has multispectral bands with a resolution of 30 m and the thermal bands with an original resolution of 100 m, and Sentinel-2 with a band bundle of 10 m, 20 m, and 60 m resolution bands.

The overall work procedure of the simplified Ehlers fusion is shown in Figure 14. Firstly, no matter how many bands the target image has, all of them are grouped according to their resolutions. Then, all of them are resampled to the high resolution and transformed into frequency domain using an FFT. Later, for each kind of resolution, a low-pass filter is applied. Meanwhile, the high-resolution image is filtered by a high-/band-pass filter. Subsequently, the filtered low and high frequencies are added together. Finally, an inverse FFT is applied and each band is transformed back to the spatial domain. All processed bands together form the fused image.

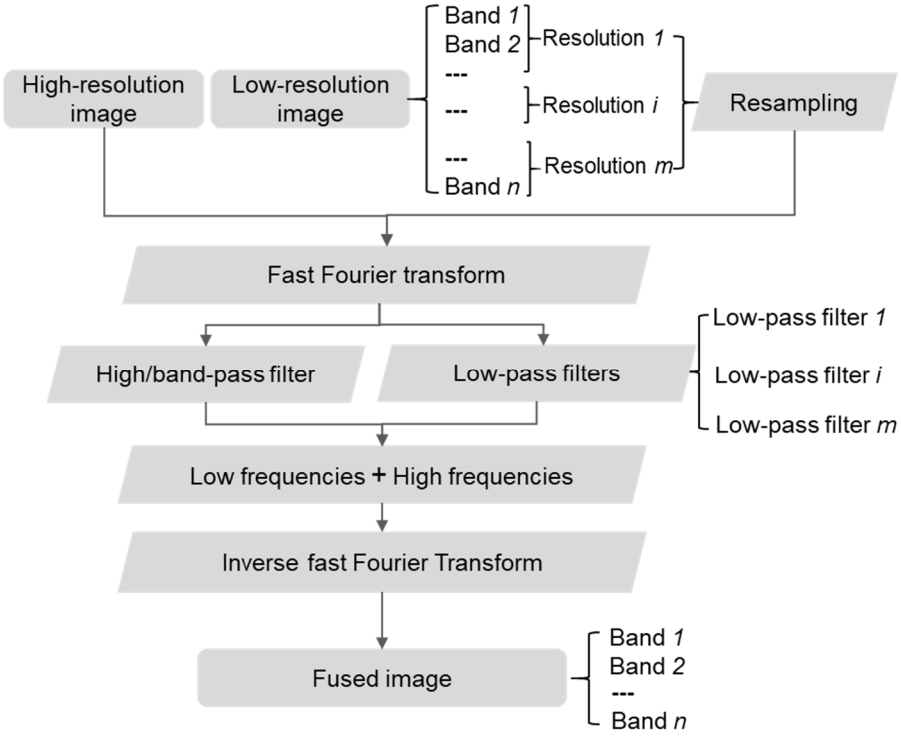

Figure 14 Overall workflow of the simplified Ehlers fusion.

This procedure can be understood when the image processing result from each step is presented with pictures. Taking a one-band image as an example, this procedure is shown in Figure 15. The spatial resolution of the source image and the target image is 0.5 m and 3.0 m respectively. The target image is firstly resampled to 3.0 m resolution. After an FFT is applied to the target and source images, the Fourier spectrum of the images provides a guideline of the spatial distribution of frequencies. Then the high-/band-pass filter can be tailored to allow a suitable amount of high frequencies to pass through, aiming at obtaining the edges and outlines of the image features. Correspondingly, the size of the low-pass filter can be adjusted to preserve the average intensity of the image. Lastly, the filtered edges and outlines will be added to the filtered intensity to construct a new image.

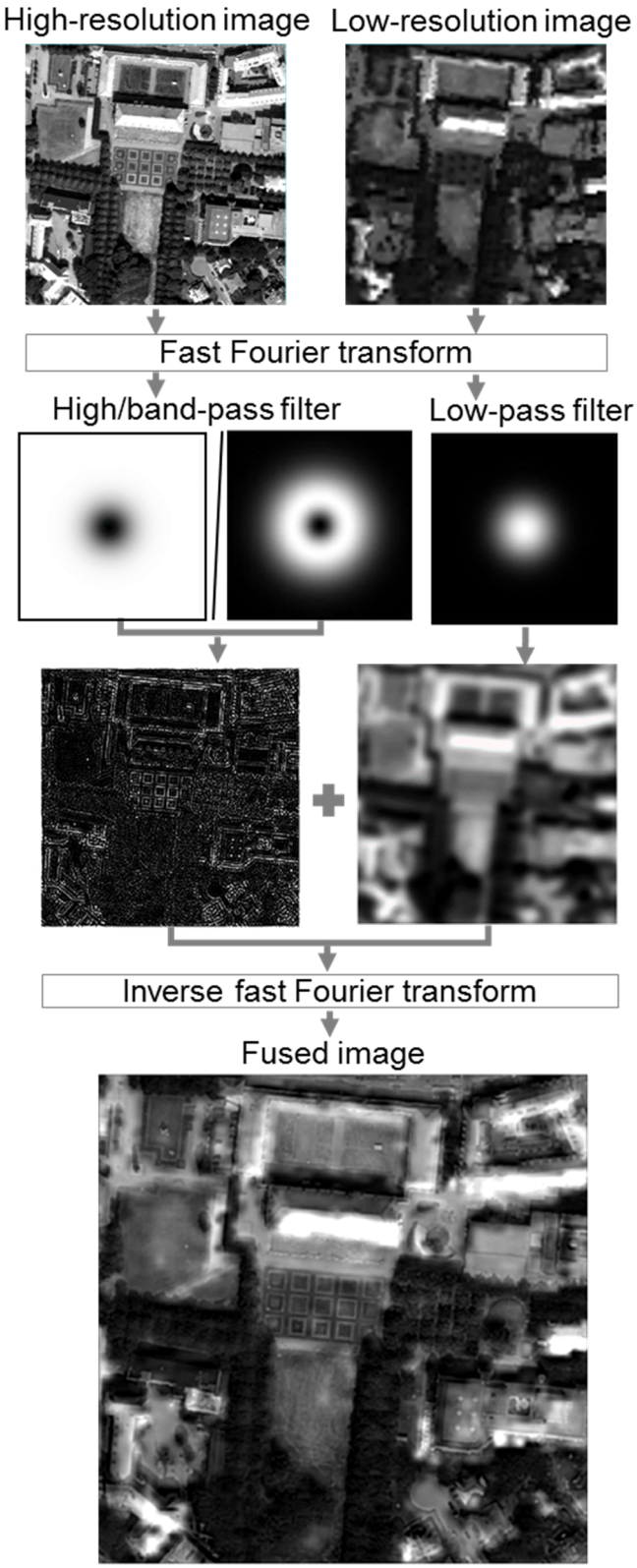

Figure 15 Simplified Ehlers fusion workflow, demonstrated with the simplest case, when both high resolution and low resolution are a one-band grayscale image.

The same workflow can be applied when the target image is not one-band but multi-bands, except that not only one but several low-pass filters might be needed to match the different resolutions. The number of bands does not play a role in this algorithm when the target image has hundreds of bands with the same resolution. The same workflow shown in Figure 15 can be conducted and repeated hundreds of times. Unlike the classic image sharpen algorithm, RGB

bands are not necessarily needed in this algorithm, because each band is processed individually and produces no impact on other bands. The spectral coverage of the image also has no influence on the fusion effect, only the edges and outlines of the high-resolution image are extracted, and the spectral information is excluded to the maximum extent. The crucial part is to test and adjust the type and size of the filters to achieve an ideal fusion effect.

2.2.4. Image fusion using simplified Ehlers fusion

To investigate the fusion effect of the newly developed image sharpening algorithm on multi-type remote sensing images, aerial photos, thermal images, and hyperspectral images are used in the following subsections. These images are produced from different sensors with a varying number of bands and spectral coverage.

2.2.4.1. Image fusion between hyperspectral image and aerial photo

The hyperspectral image is used as an example because its important and unique capabilities are not replaceable by other remote sensing techniques. Here, the instrument HyMap was used due to its high quality and the data availability for the study area. The first sensor of HyMap covers the wavelength range of 0.55 µm to 2.5 µm with 96 channels. Subsequently, it was modified to up to 128 channels, including 126 bands covering 0.44 µm to 2.5 µm spectral region and two additional thermal bands. The 126 bands in the spectral region are often discussed and the two thermal bands are usually neglected in previous research. The 126 bands are about 15 nm wide and separated into visible (VIS) and NIR, short-wavelength infrared (SWIR) modules, namely SWIR1 and SWIR2. The spectral configuration provides contiguous sampling across the spectral region except for the two gaps near 1.4 µm and 1.9 µm, due to the strong atmospheric water absorption. To have an orientation of the positions of these bands, it was compared with the location of the multispectral bands from Sentinel-2 produced by ESA (Figure 16). The HyMap sensor covers the spectral range of the Sentinel-2 sensor except band 9 which was designed for water vapor detection purpose.

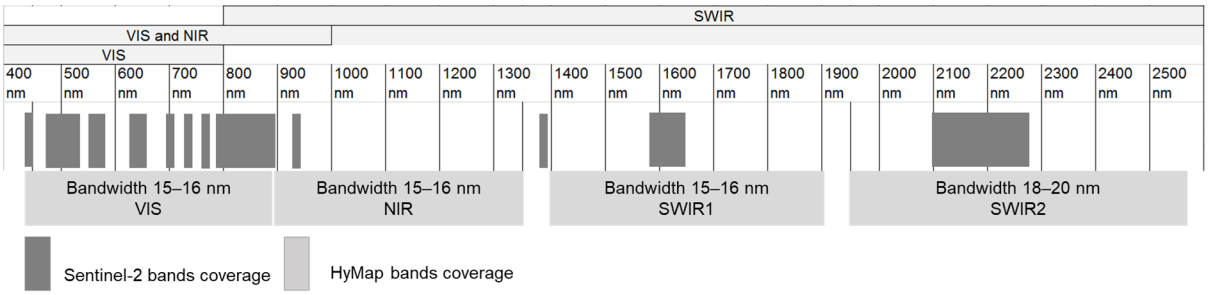

Figure 16 Comparison of the band locations between Sentinel-2 and HyMap bands. NIR: Near infrared. SWIR: Short-wavelength infrared. VIS: Visible.

The test image used in this thesis was obtained during a flight campaign carried out by the German Aerospace Center in 2003 over the city of Osnabrück. The data was collected by the HyMap airborne hyperspectral scanner and recorded as 3 m pixel size raster images.

The higher-resolution source image used here is an aerial photo produced by the Local Earth Observation system developed at the Bochum University of Applied Sciences (Bäumker and Heimes, 2002). It has RGB bands and has been ortho-rectified. The spatial resolution is 0.5 m, and the red band is taken as the high-resolution image input to sharpen other images.

After geo-referencing of these two datasets, the hyperspectral image is resampled to 0.5 m using a cubic convolution resampling method. The selected study area is the same area as in the section 2.2.2where the different filtering effects were demonstrated. Then the fusion algorithms were applied to all bands of the selected images. In the end, band 15, band 9, and band 4 were selected from the fused image to visually check the fusion results because they were located at the RGB spectral ranges, respectively.

To a certain extent, a pan-sharpening of hyperspectral images is an extension of pan-sharpening multispectral images. The classic algorithms such as PC, Gram-Schmidt, and Wavelet-PC were tested, as these methods were developed for pan-sharpening multispectral images. Figure 17 provides an impression of these fusion methods working on the dataset. The test was done with software packages ERDAS IMAGINE 2014 and ENVI 5.1. From visual inspection, PC and Gram-Schmidt methods produce obvious color distortion. Wavelet-PC produces no significant spatial improvement, yet produces color mismatches and obvious artifacts.

Figure 17 Pan-sharpened hyperspectral images using (a) Gram-Schmidt, (b) PC, and (c) Wavelet-PC. PC: principal component.

In contrast to the classic algorithms, simplified Ehlers fusion produced excellent color preservation. Compared to the original image, the color display of the fused image is identical, showing red castle, dark green trees, light green lawns, and gray road surfaces (Figure 18). The algorithm produces significant spatial enhancement. In general, the outline of the buildings, streets, lawns, and even tree canopies are much sharper after fusion. The magnified garden area shows that the boundary of the garden area is not visible in the original image yet clearly noticeable in the fused image (Figure 18a_1 and Figure 18b_1). The fused image keeps the color pattern of vegetation inside the garden area identical with the original image.

Taking a closer look at a building area (Figure 18a_2 and Figure 18b_2), the edges of the buildings together with the roof windows on top are clearly visible in the fused image, though they are not distinguishable in the original image. Within this building area, some buildings have a red color roof and the others have a dark or light gray color roof. All of these color differences were transformed into the fused image. This is in correspondence to the purpose of the algorithm, which is to enrich linear features while preserving the original color information.

Notably, the light-yellow part shows up as an unmistakable feature in the hyperspectral image but is not a feature in the aerial photo at all. After fusion, this light-yellow colored part

successfully transformed into the fused image (Figure 18a_3 and Figure 18b_3). This proves that all the original spectral information was preserved.

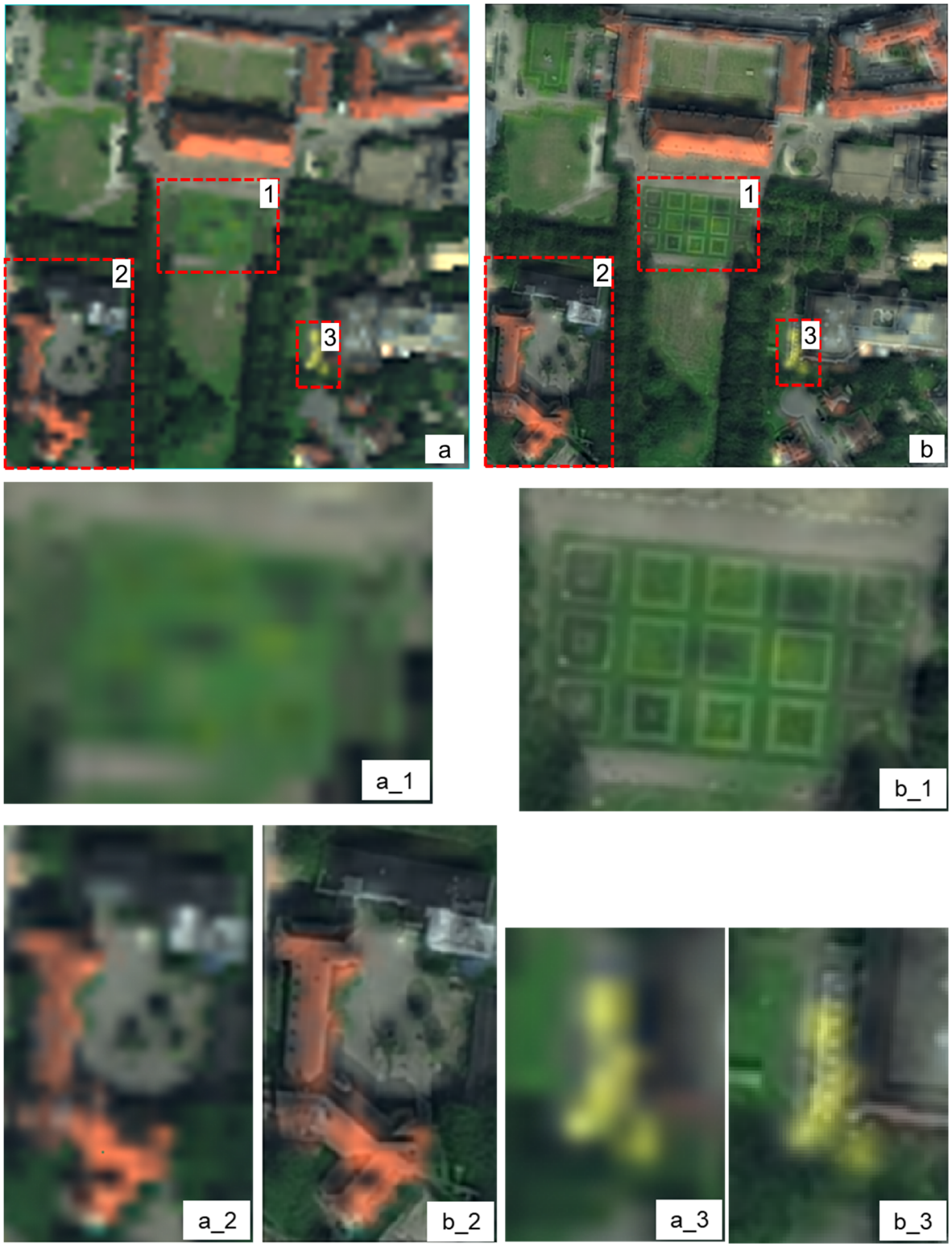

Figure 18 Using simplified Ehlers fusion to sharpen hyperspectral image: (a) original hyperspectral image with the true color display where RGB bands are represented by band 15, band 9, and band 4 respectively; (b) fused image with the same color display; (a_1, b_1, a_2, b_2, a_3, b_3) magnified areas marked in (a) and (b). RGB: red, green, and blue.

2.2.4.2. Data fusion between thermal image and aerial photo

Furthermore, the simplified Ehlers fusion is also applied to sharpen a one band thermal image. The source image is the same aerial photo from subsection 2.2.4.1. The thermal image is obtained from a thermography imaging flight mission with a Cessna 208B aircraft on February 18, 2015. The flight carried the thermal camera FLIR SC6000 HS, which uses the spectral windows in the 3.0 μm to 5.0 μm and 8.0 μm to 9.2 μm range. This spectral range does not have any overlap with the spectral coverage of the aerial photos.

As the FLIR products are designed for easy image viewing, the output data are pseudo color images instead of thermal radiometric data. However, the color map information which describes conversion between color value and radiometric value are not available from the camera producer. It is because the camera manufacturers do not want to let the other manufacturers know what data they were storing or not storing in their image files, and the customers have to use the software from the manufacturers to further process the data, so that the manufacturers can lock the customers into their product system (Goodman, n.d.).

Even though it is uncertain how the thermal radiometric value is converted to color, the basic information of the image can be found by reading the image in QGIS software. The produced thermal image is a three-band pseudo color image with 0.6 m spatial resolution. Usually, the thermal image is a one-band image with thermal radiometric value, such as the open source thermal images. Thus the three-band image is first converted into a one-band grayscale image. Then, this grayscale image is resampled to 0.5 m because it is the spatial resolution of the aerial photo and also the target resolution of the image sharpening. In this way, the 0.5 m thermal images can be used as a reference image (Figure 19a) to validate the fusion quality. Afterward, the “original” image before fusion is created by resampling the 0.5 m thermal image into 3 m (Figure 19b). Then, it was sharpened by the aerial photo, one with a high-pass filter (Figure 19c) and the other with a band-pass filter (Figure 19d).

Compared to the “original” thermal image, the fusion process keeps the original temperature distribution. The hottest places appear at the surfaces built up with concrete such as the steps in front of the castle, and the buildings with a concrete roof. The coolest places are covered with trees. An intermediate temperature can be found on houses with tile roof. Meanwhile, the fusion procedure enhanced the image sharpness significantly. All urban structures and details were clearly distinguishable.

The interesting facts come from the comparison between the “original”, reference, and the fused images. Some small thermal features from the reference image were lost after resampling to the “original” image, such as the six air vents on the roof of the building (Figure 19b_1). However, they appear again in the fused images due to the information from the aerial photo (Figure 19c_1 and Figure 19d_1). In another case, the opposite situation appears: the roof windows on top of the castle are not noticeable in the reference image but show up in the fused images (Figure 19c_2 and Figure 19d_2). This could be explained by two possible reasons: firstly, the high-resolution input image is the red band of the aerial photo and the roof windows also have red color. Thus, the strong spectral information of the windows cannot be completely excluded. Secondly, the frames of the windows were considered by the algorithm as sharp edges and were transferred into the fused image.

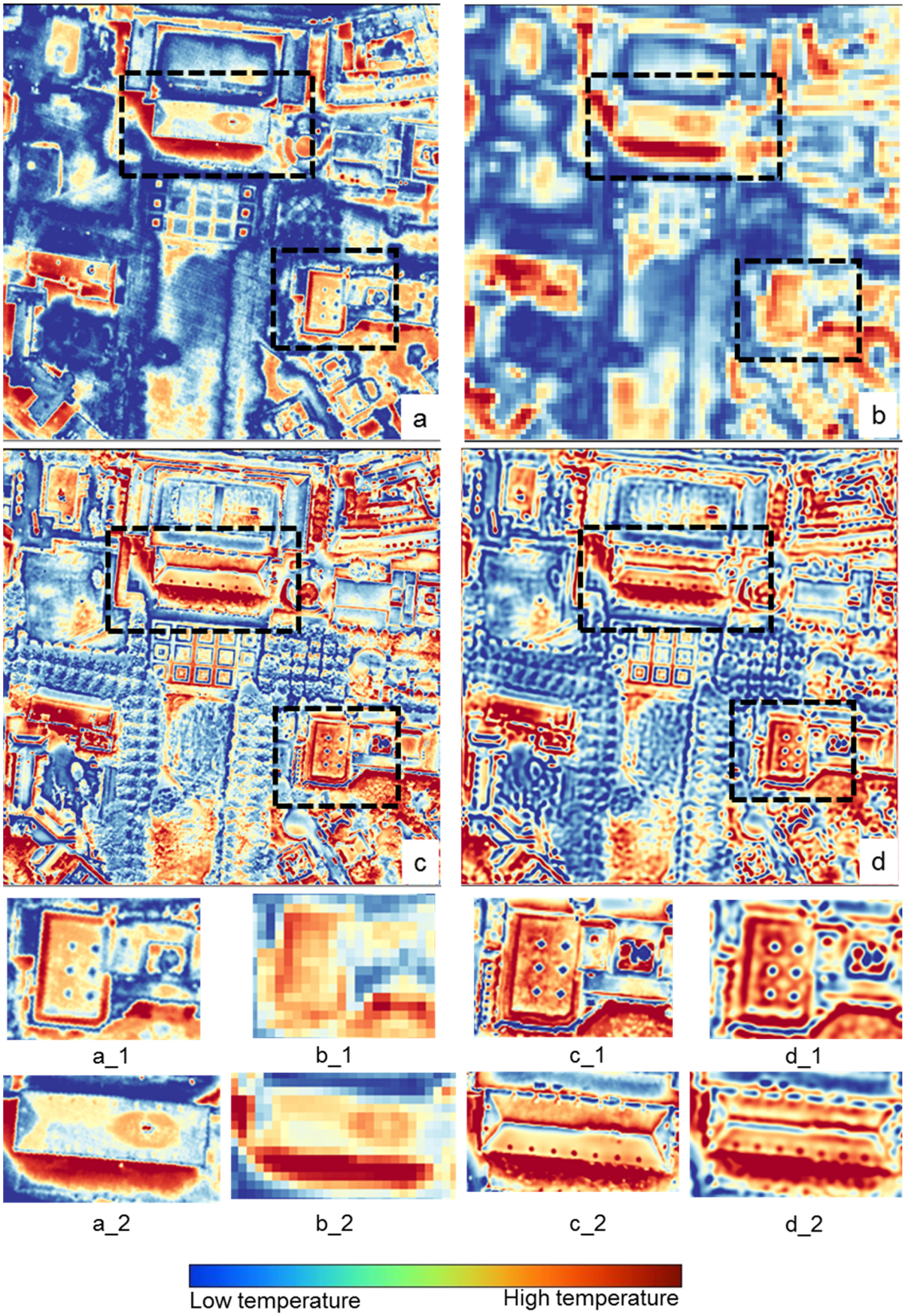

Figure 19 Using simplified Ehlers fusion to sharpen a thermal image. (a) Thermal image of 0.5 m resolution is used as a reference; (b) "original" image with 3.0 m resolution is resampled from (a); (c) fused image where the high-pass filter is applied; (d) fused result where the band-pass filter is applied. (a_1, b_1, c_1, and d_1), (a_2, b_2, c_2, and d_2) are the magnified building with air vents and the castle with dormer windows respectively.

There is a slight difference between the fused results from the high-pass filter and the band-pass filter. Using the high-pass filter generates sharp results in a way that the character of the aerial photo becomes dominant. In the result where the band-pass filter is applied, the component of the aerial photo is less dominant, and the elements of the thermal image are more pronounced. For example, the tree canopy in the image generated by the high-pass filter is clearly visible but might not be necessary for the thermal image, whereas in the band-pass filtered image the color of the tree area is blurred but smoother. However, further effort could be devoted to adjusting the size of the band-pass filter to achieve perfect fusion effects. By limiting the frequencies input from the high-resolution image, its influence on the fused image can be reduced. However, too few frequencies input could produce artifacts. For example, as shown in Figure 19d, the band-pass filter has an inner ring of 100 and a width of 100. If the size and width of the inner ring were changed to 50, the produced result was very blurry and artifacts appeared (data not shown).

In this subsection, the fusion effect was tested by using images without or with very few spectral overlaps. From a physics point of view of remote sensing, the fusion process could potentially introduce additional information which does not exist in the original image. For example, in Figure 19a_2, Figure 19b_2, Figure 19c_2, and Figure 19d_2, the roof windows were hardly distinguishable due to the similar temperature with surroundings, but clearly visible in red color on the fused thermal image. However, this red color does not necessarily mean high temperature. In other words, the fusion process produced an impact on the physical interpolation of the image. In this context, it is worth to discuss if image fusion still has physical meaning when the input images have separate spectral coverages. This question can be answered in three steps.

- Firstly, local dissimilarities happen not only when the input images have disconnected spectral coverage, but also when the spectral coverages overlap. In the study from Thomas *et al.* (2008), a ground object was not visible on the blue band image but clearly noticeable on the pan image, even though the pan and blue band share a common spectral coverage. This is because pan and the blue band have different bandwidths, which make them sensitive to different ground objects.
- Secondly, it is necessary to receive the added information from the high-resolution image. Without this information, there will be no spatial improvement. The enriched spatial details on the fused image consist of the added information. More figures in section 2.3.1 will further illustrate this point.
- Lastly, the physical meaning of fused images from separated spectral coverage can also be examined in practical use. FLIR, one of the industrial thermal camera companies, has developed a Multi-Spectral Dynamic Imaging technology to improve the clarity of the thermal images (FLIR, n.d.). This technology extracts the spatial details from the onboard RGB camera and inserts them into the thermal images, to produce a sharper thermal image or video in real-time. However, this technology is already patented and not open. Another example is the current study of UHI, where the thermal images from satellites also need to be spatially improved by using the vegetation index. The detailed literature review and applications are presented in chapter 3.

In brief, local dissimilarities generally appear on any images with different bandwidths, whereas image fusion is exactly between those images. Therefore, these dissimilarities could always

reappear after fusion regardless of whether the spectral coverage is connected or separated. It is necessary to keep dissimilarities when they represent improved spatial details. Additionally, it is very meaningful to have an algorithm that can realize the image fusion between images with disconnected spectral coverage due to many applications in practical use.

2.3. Quantitative fusion quality evaluation and discussion

The above fusion results have been validated with visual inspection. Quantitative methods are frequently used for checking fusion quality (Li *et al.*, 2010). The most commonly used quality index includes root-mean-square error (RMSE) which is a standard measurement of the value of differences, the relative average spectral error (RASE) which is the average RMSE of all bands and is expressed as a percentage, relative dimensionless global error of synthesis (ERGAS) which is a further development of RASE with additional consideration of the resolution ratio between the two image sets, and the universal image quality index (UIQI) which is a combination of its mean, standard deviation and correlation coefficient (CC).

Table 3 shows the results using these quality indices to evaluate the fusion quality of the fusion results in subsection 2.2.4.2. According to these indices, simplified Ehlers fusion shows better performance compared to the classic fusion methods, taking HPF and PC as examples. However, these statistical indices do not play an important role in fusion quality evaluation in this thesis. This is because there are some general problems of taking the commonly used statistical indices to evaluate fusion quality, as well as several image processing procedures influencing the fusion quality evaluation.

Table 3 Image fusion quality evaluation.

Fusion algorithm	ERGAS	UIQI	RASE	RMSE
Simplified Ehlers fusion	0.062	0.70	0.25	50.98
HPF	25.250	0.26	48.10	30721.00
PC	25.750	0.32	60.00	31323.00
Ideal Value	0.000	1.00	0.00	0.00

ERGAS: relative dimensionless global error of synthesis. HPF: high-pass filter. PC: principal component. RASE: relative average spectral error. RMSE: root-mean-square error. UIQI: universal image quality index.

2.3.1. Disadvantage of using statistical methods for fusion quality evaluation

Pixel-based image fusion aims at spatial resolution improvement while avoiding spectral distortion. Thus, the evaluation of image fusion quality emphasizes two aspects: *spectral preservation* and *spatial improvement*. The most direct assessment method is visual inspection. It can examine if the fused image retains the original color distribution and luminance, as well as if the fused image becomes blurrier or sharper than before. Through comparison between the high-resolution input image and the fused image, it can reveal how much spatial detail from the input image has been merged into the fused image and if artifacts exist. The disadvantage of this manner is that human observation is subjective and is problematic as a means of measurement.

100	100	100	100	100	100	100	100
100	100	100	100	100	100	100	100
100	100	100	100	100	100	100	100
100	100	100	100	100	100	100	100
100	100	100	100	100	100	100	100
100	100	100	100	100	100	100	100
100	100	100	100	100	100	100	100
100	100	100	100	100	100	100	100

100	100	100	100	90	90	80	80
100	100	100	90	90	80	80	80
100	100	90	90	80	80	80	90
100	90	90	80	80	80	90	90
90	90	80	80	80	90	90	100
90	80	80	80	90	90	100	100
80	80	80	90	90	100	100	100
80	80	90	90	100	100	100	100

Figure 20 Illustration of how spatial improvement will change pixel values.

Thus, it is necessary to use a quantitative approach for quality evaluation, and statistical methods have merged as the frontrunner. Li *et al.* (2010) conducted a survey and found a total of 27 measurements for quality assessment. From the calculation function of the list of measurements, 14 of them deal with mean, standard deviation, CC, and variance, which are basic statistical parameters. These statistical methods compare the pixel values between the original and fused images; the ideal fusion result should show close average and low standard deviation. For the original and fused images, identical pixel values mean same color, and same color implies good spectral preservation. This is true for images with large patches of homogeneous areas; for example, green forests after fusion should also remain green in color, but it is doubtful if the image is taken in an urban area. As urban space is a heterogeneous area, image fusion will integrate linear structures such as the outline of streets and roads into the fused image. These linear structures are distinguishable because of color changes. Many of these features will cause a higher percentage of color change than images which contain homogeneous land cover. These changes are necessary and desired but will be recognized as poor fusion results using statistical methods. Figure 20 shows an example: a lawn in the original image is represented as a piece of blurred dark green area. After fusion, the outline of this lawn can be clearly seen due to its rather light green color. Here, the original image is resampled into the same resolution as the fused image. Taking a close look at pixel values at the border of the lawn, in the original image they have the same pixel values, while in the fused image the pixel values have been changed, conceptually illustrated by the values presented. If using statistical

measurements, the lawn border parts will show a high deviation. Such kind of spatial details will also appear on houses, gardens, roads, or any features in urban areas. All of them will contribute to the high deviation of pixel values.

Image fusion methods show a trade-off between color preservation and spatial improvement performance. This is because statistical measurements are applied as quality evaluation. The more spatial details added into the fused image, the more color change will happen. Zero deviation, one hundred percent CC equals to absolute color preservation but leads to no spatial improvement. From the author's point of view, it is not beneficial to pursue perfect statistical values as the goal of developing fusion methods, when the fusion method will be applied to urban areas. However, in agriculture and forest-dominated areas, a rather high degree of similarity measured by statistical values might reflect a good spectral quality of the fused image.

Though statistical measurement is not a perfect method for spectral quality assessment, it is even more difficult to quantitatively assess spatial quality improvement. In general, spatial details are built up by a group of pixels—spatial improvement cannot be measured by looking at a pixel-by-pixel basis. It is claimed that the fusion quality indices that have been developed can reflect both spectral preservation and spatial improvement performance. Among them, the most popular ones are UIQI, quality index based on local variance, usually referred to as quality index based on local variance (Aja-Fernandez *et al.*, 2006), average value of local variance (Beauchemin *et al.*, 2002), and structure similarity index metric (Wang and Bovik, 2002). A close comparison of the functions from these indices show that there are small differences in expression but are essentially the same. When these indices are implemented, a sliding window approach is applied. The measurements are computed locally based on the pixels within the window, then this window moves pixel by pixel horizontally and vertically through all the rows and columns of the image. In the end, the overall quality index is the average of all the local measurements.

$$Luminance\ distortions = \frac{2\mu_r\mu_f}{\mu_r^2 + \mu_f^2} \tag{8}$$

$$Contrast\ distortions = \frac{2\sigma_r\sigma_f}{\sigma_r^2 + \sigma_f^2} \tag{9}$$

$$Correlation\ loss = \frac{\sigma_{rf}}{\sigma_r\sigma_f} \tag{10}$$

$$UIQI = \frac{2\mu_r\mu_f}{\mu_r^2 + \mu_f^2} * \frac{2\sigma_r\sigma_f}{\sigma_r^2 + \sigma_f^2} * \frac{\sigma_{rf}}{\sigma_r\sigma_f} \tag{11}$$

where μ_r and μ_f are the local means of the image r and f
σ_r and σ_f are the standard deviation of image r and f
σ_{rf} is the local correlation coefficient between the image r and f

In the following, UIQI is taken as an example to present how this index works with a window of 3 × 3 pixels. It was claimed that the function reflects three parts: correlation loss, luminance distortions, and contrast distortions, equations (8), (9), (10), and (11). Thus, the calculation

results are displayed in three parts. Assume that blue color has a pixel value of 100 and white color has a pixel value of 50. In the original image, the blue color forms a geometrical cross feature (Figure 21a). After two fusion methods, part of the feature has been lost (Figure 21b and Figure 21c). Obviously, fusion result 1 retains more structure information than fusion result 2. Through the computed statistical values (Table 4), result 1 is more related to the original. Fusion results 1 and 2 have few luminance and contrast distortions. The overall index UIQI shows fusion result 1 has better quality than result 2. In this way, the index can reflect the fusion quality in a reasonable range.

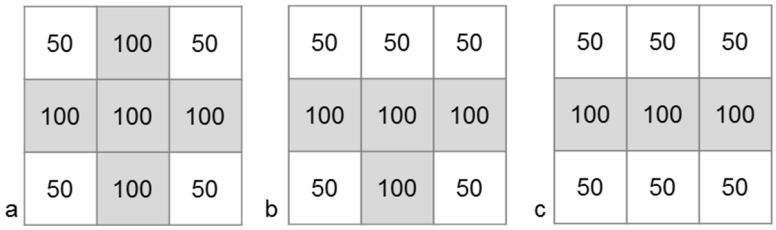

Figure 21 Loss of structure information caused by fusion, illustrated using a 3 × 3 pixel window; (a) original image and its pixel values, (b) fusion result 1 and its pixel values, and (c) fusion result 2 and its pixel values.

Table 4 Quality evaluation in the case of loss of structure information.

Result	UIQI	CC	Luminance	Contrast
Fusion result 1	0.7978	0.80	0.9972	1.0000
Fusion result 2	0.6241	0.63	0.9882	0.9986

CC: Correlation coefficient. UIQI: Universal image quality index.

However, this is just the case when the fused image has lost the existing structural information compared to the original image, while in the image sharpening context, the fused image will add extra structure information. Then the index does not work in the same way. Figure 20 shows that in the image sharpening context, an original image (Figure 22a) has no visible structures inside. After image fusion, a cross structure (Figure 22b) or a linear structure (Figure 22c) can be generated. CC shows both fusion results have strong contrast distortion and are also poorly related to the original image. Result 1 has better luminance preservation than result 2, but the luminance distortion from both are very low. The overall index indicates that both images have poor fusion quality. This means by the measurement of UIQI, if image fusion provides new structures into the original image, it will result in a poor evaluation of fusion quality. However, just due to these new structures, spatial details can be presented in the fused image. The goal of image sharpening should be enriching spatial details as much as possible, instead of producing good statistical quality results. Therefore, it is not appropriate to use this index to measure spatial improvement performance of the image fusion method. This is similar to other indices which are like the UIQI.

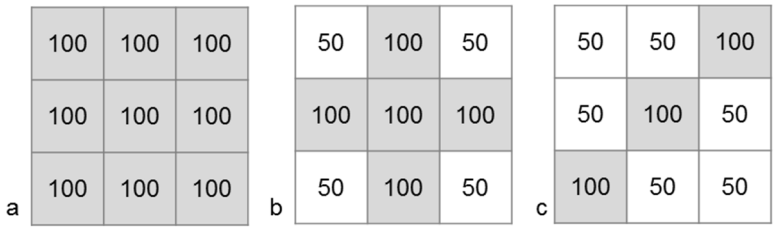

Figure 22 Enrichment of structure information caused by fusion, illustrated within a 3 × 3 pixel window; (a) original image and its pixel values; (b) fusion result 1 and its pixel values; and (c) fusion result 2 and its pixel values.

Table 5 Quality evaluation in the case of enrichment of structure information.

Result	UIQI	CC	Luminance	Contrast
Fusion result 1	0.000775	0.3162	0.9692	0.0025
Fusion result 2	-0.000615	-0.2500	0.9230	0.0026

CC: Correlation coefficient. UIQI: Universal image quality index.

2.3.2. Image processing procedures which influence the fusion quality evaluation

By checking the function with which the quality evaluation index is calculated, all the functions are computed based on pixel values. Therefore, any factor resulting in pixel value change will also influence the result of the quality evaluation. However, during image fusion and quality evaluation, nearly every image processing procedure modifies pixel values. Before image sharpening starts, the input and target images need to be registered to the same coordinate system. Then an area of interest can be clipped out. Lastly, the low-resolution image needs to be resampled to the same pixel size as the high-resolution image.

Image co-registration is the first step in image fusion. Images can be retrieved from various sources where no or different coordinate systems were used. For image sharpening, it is crucial that the input and target image are co-registered correctly so that the data is comparable on a pixel-to-pixel basis. There are different ways to co-register two images: in the optimal case, both images are registered to one map coordinate system where each pixel is in its geometrically correct position and has coordinates. Pohl and van Genderen (2017) provide detailed descriptions of image registration. This thesis emphasizes that regardless of the way in which the images are registered, the pixel size of the images can be changed to fit the new map grids. For example, a square image with a pixel size of 0.5 × 0.5 m will be modified to 0.511272 × 0.511272 m, or a rectangular image with a pixel size of 15 × 15 m will be adjusted to 15.2088 × 14.7993 m. The change of the pixel size necessitates image resampling in geo-registration, while resampling will modify the pixel values. Table 6 shows the pixel value changes of an 8-bit image and Table 7 of a 16-bit image. After geo-registration, the mean and the standard deviation of the pixel values have been slightly changed, albeit less than one percent. The minimum and maximum have been changed more, particularly for the 16-bit image, up to 20%. As these changes are nearly not visible by visual inspection, they are often ignored.

Table 6 Geo-registration causing the statistical change of pixel values (8-bit-image).

Results	Original	Geo-registration	Changes in %
Maximum	255	255	0
Minimum	1	0	-100
Mean	100	96	-4
Standard deviation	66	68	-2

Table 7 Geo-registration causing the statistical change of pixel values (16-bit-image).

Results	Original	Geo-registration	Changes in %
Maximum	32766	26094	-20
Minimum	-6280	-1072	-83
Mean	1631	1488	-9
Standard deviation	1144	1104	-3

Image clipping is often used in the application of spatial data on urban research, as the urban area needs to be clipped out from a raster image. For image sharpening purposes, a subset of the high-resolution and low-resolution image will be cut together by the border of an urban area. In the case that the border crosses half of the pixel size of the low-resolution image, it is impossible to cut half of the pixels, as a pixel is the minimum unit of a raster image. Then, the row above or below the border will be taken as the starting line of cutting. At the same time, due to the smaller pixel size, the urban border can go through underneath a row of pixels of the high-resolution image. Therefore, the row under the border will be taken as the starting line of cutting. In the end, the two subsets of the images are not precisely overlaid. Figure 23 illustrates this situation. It serves as an example to show that when clipping is applied to the high-resolution and low-resolution image together, the generated images may not be completely aligned. Assuming the low-resolution image has a resolution of 30 m, in the above case, a shift of 15 m will be generated. In the urban context, a shift of 15 m could mix up one building with another or result in a street deviating from its original direction. If fusion is conducted between the two shifted images, the image features will also be shifted within the fused image. In this way, the fusion quality is reduced.

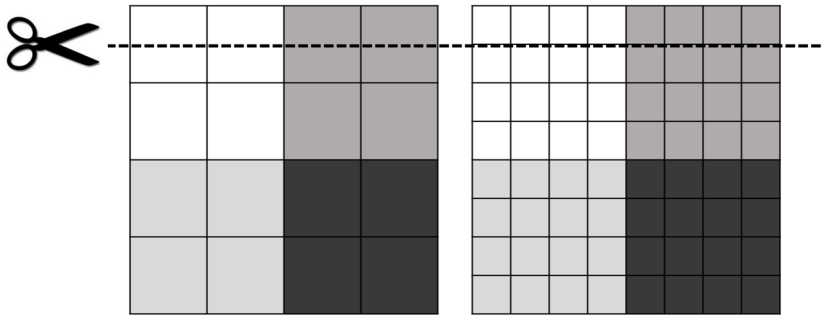

Figure 23 Pixel mismatch caused by image clipping.

To avoid this problem, this thesis suggests resizing the low-resolution image to a higher resolution before cutting the subsets. This means the image will go through geo-registration, resize, and then clipping. It is worth mentioning that during geo-registration, resampling already occurred once, so resizing constitutes another resampling. Thus, before image sharpening occurs, the image has already been resampled twice, modifying the pixel values (see the following paragraph). Strictly speaking, not the original image but a modified image is used for the sharpening procedure.

Resampling is used for geo-registration and resizing in image sharpening procedures. The common resampling algorithms include nearest neighbor, bilinear interpolation, and cubic convolution. Different resampling techniques change the pixel values differently. For the case of resampling, Figure 24 shows the use of nearest neighbor or cubic convolution to reduce the pixel size of an image. After resampling, the resolution of the image has been increased, which is also called up-sampling. Cubic convolution produces a smooth color change, and nearest neighbor retains the original pixel values but can produce blocky artifacts. Comparing two resampled images pixel by pixel, very few pixels have the same color, equal to the same pixel values. Certainly, this is an extreme example where the strongest color contrast, black and white, is applied. In a real situation, the difference is not likely to be so stark but can exist.

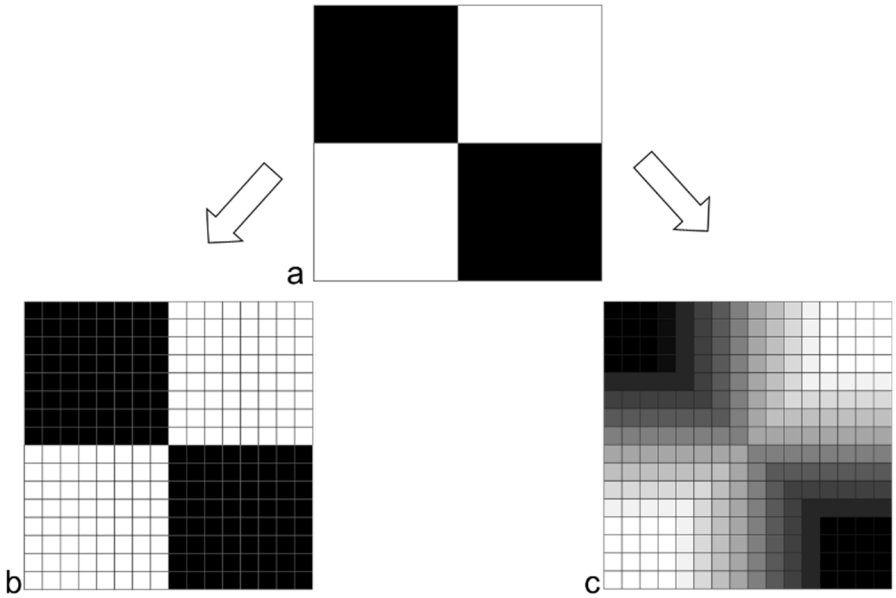

Figure 24 Change of pixel values caused by different resampling methods: (a) original image is resampled using (b) nearest neighbor or (c) cubic convolution. The colors used in (b) and (c) aim to display differences in resample effects but not precise interpolation results.

Resampling is not just used before image sharpening but also afterward. As there is no matched reference image to validate the pan-sharpened image, the fusion quality evaluation needs to be conducted indirectly. Two different strategies have been commonly used. The first one takes an up-sampled original image and then compares it with the fused image. In the second method, both the original high-resolution image and the low-resolution image are firstly down-sampled to even lower resolution, then the down-sampled image is sharpened to original resolution and compared with the original image. Figure 25 illustrates the two procedures with a pan image of 15 m resolution and a multispectral image of 30 m resolution. The quality assessment can be conducted on 15 m resolution level, where the fused and up-sampled multispectral images are compared to each other. On the down-sampled level, the original pan is resized to 30 m resolution and the multispectral image is resized to 60 m resolution. After image fusion, the generated multispectral image has a 30 m resolution. Then the original multispectral image with 30 m resolution is used as a reference for quality assessment. Here, the pan image represents the general high-resolution image and the multispectral image represents the general low-resolution image. No matter which strategy is applied, resampling is required, either up-sampling or down-sampling. Even though the original image is geo-registered and resized using cubic convolution before image sharpening, the quality assessment is performed by using the

nearest neighbor up-sampled original image as a reference. In this case, the comparison will be conducted in the situation described by Figure 24b and Figure 24c. Then, no matter whether the fusion algorithm produces perfect color or poor preservation effects, the statistical evaluations will conclude a bad fusion quality.

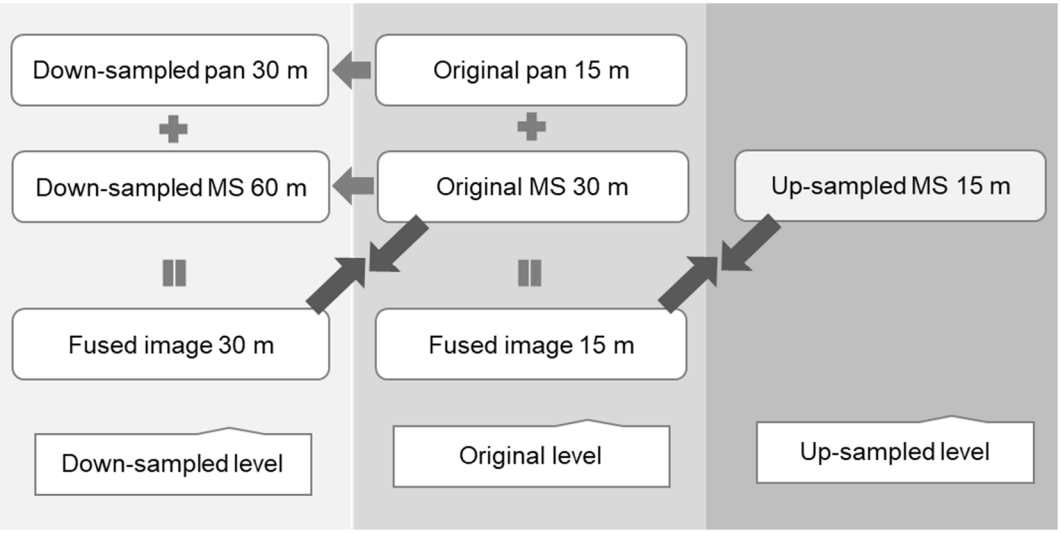

Figure 25 The strategy of comparison between original and fused image, in the context of fusion quality evaluation. MS: multispectral.

Resampling plays an important role in image sharpening applications, even though very few studies report which algorithms were used for image sharpening and quality assessment. To avoid misjudgment about the fusion quality, this thesis draws attention to resampling and suggests that resampling methods before and after fusion should be kept consistent.

In summary, in this chapter, various filters in the frequency domain were tested and based on that, the simplified Ehlers fusion was developed. Through adjusting the type and size of the filters, the exact amount of high frequencies and low frequencies can be extracted and mixed together to achieve ideal fusion results. The algorithm was successfully applied in sharpening the one-band thermal image and 126-bands hyperspectral image. The source image is an aerial photo which has different spectral coverage as the target images. In both cases, the algorithm shows strong color preservation and spatial enhancement performance. Quantitative indices were used but not considered as effective methods for assessment of fusion quality. It was found that these indices are statistically measuring the changes in pixel values: more changes reflect lower quality or in other words, changes are considered as errors. However, the author of this thesis proposes that the changes in pixel values do not always represent errors. Instead, they could indicate increased spatial detail. Additionally, many image processing procedures also contribute to the change in pixel values but their influence on fusion quality has not been discussed by the research community. The fusion quality check is mainly done by visual inspection as quantitative indices do not provide the complete picture of the fusion quality.

In the next chapter, the developed algorithm is applied to open source remote sensing images. Due to the limited source of free hyperspectral images, the only free thermal images are taken as the target images for image sharpening purposes. To investigate the function of the developed algorithm in practical use, UHI is taken as an application case. The goal is to examine to which

extent the simplified Ehlers fusion can improve the performance of open source thermal images in UHI analysis and benefit sustainable urban development.

3. Data fusion applications on urban heat island analysis

UHI describes the temperature near the ground in cities as higher than those of nearby non-urban areas. High temperatures seriously affect the quality of life, particularly those with a high proportion of elderly people sensitive to uncomfortable heat (EEA, 2017, p. 26). It occurs in winter and in summer, when it is more severe and could be a threat to human health within cities. UHI also has a strong impact on energy demands and fossil fuel consumption, required for air-conditioning and refrigeration in hot seasons. This in turn results in higher emission of air pollutants and greenhouse gases, which make urban areas increasingly vulnerable to climate change (Lauriola, 2016).

UHI is chosen as a case study because firstly, it generally produces discomfort to urban dwellers in summer. Secondly, it is one of the most typical phenomena of urban climates that challenge living. Thirdly, it is increasingly affecting cities in the central and north-western Europe (EEA, 2017), as well as in the whole world.

Causes of UHI include the replacement of soil and vegetation with urban structures, such as buildings, pavements, and roads. The urban fabric surface is sealed with concrete, asphalt, metal, and other impervious materials. These materials absorb heat during the day and re-emit it after sunset, leading to higher temperatures than in rural areas. High-rise buildings and narrow streets impede airflow, contributing to a further increase in surface temperature (Ngie *et al.*, 2014). Additionally, the UHI effect is enhanced by anthropogenic heat produced from artificial heating and cooling of buildings, transportation, and industrial processes. Additional causes consist of the reduction of evaporation surface, urban “greenhouses”, and surface albedo (Priyadarsini, 2009). Priyadarsini (2009) considered building masses as the main reason for UHI because on one hand they increase thermal capacity, and on the other hand, reduce wind speed.

UHI measurement can be done with ground-based observations, where air temperature and surface temperature are recorded separately. The air temperature is usually read from a thermal probe which stands at about 1 m distance from the surface. Infrared radiometer and contact thermistors are often used for surface temperature measurement (Nichol, 2005). Other than some air temperature data which can be collected from weather stations, ground-based observations are mainly generated from fieldwork, which is time and energy consuming. Additionally, high human resource costs are incurred, particularly when the study area is a megacity. It is also difficult to make ground-based measurements well-distributed over the city, especially if the data is taken from weather stations, as it depends on where the instrument is set up. The limits of using ground-based measurements to assess a heat island also include changes in instrumentation, sampling, and data recording methods (Ngie *et al.*, 2014).

3.1. Current research regarding urban heat island

The limitations of ground-based measurements can be overcome by using thermal remote sensing data which provides wider spatial and temporal coverage over urban environments. Thermal remote sensing is based on the principle that infrared radiation is emitted by all objects with a temperature above 0 K. The thermal infrared range of the electromagnetic spectrum covers roughly wavelength from 3 μm to 14 μm. But only the 3 μm to 5 μm range and 8 μm to

14 μm ranges are commonly used by thermal sensors because of the atmospheric transmittance or atmospheric windows (Curran, 1985). Remote sensors in the thermal domain or thermographic cameras can detect the thermal infrared radiation within the atmospheric windows, thus making it possible to derive thermal radiance images of objects on the Earth's surface. Such images are used to observe the variations in temperature due to the amount of radiation emitted by objects with different temperatures. Thermal remote sensing can be operated through airborne, unmanned aerial vehicle, usually referred to as UAV, borne, as well as spaceborne sensors or cameras. The most commonly used data for UHI analysis are produced from satellite-based sensors, including Landsat 7 ETM+, MODIS, and ASTER. The related research mainly covers the following four topics:

Comparison of the temperature difference between the satellite-derived land surface temperature (LST) and ground-based measurements show that they are strongly correlated and are more similar at nighttime (Nichol, 2005). Coll *et al.* (2010) proved that ETM+ derived LST has a good agreement with the ground-measured LSTs, with differences in the range of ±1 K. Tan *et al.* (2017) showed that the differences between the LST retrieved from Landsat 8 thermal bands and ground temperature sensors were less than 1.2 K for water and less than 0.75 K for buildings and vegetation.

The relationship between UHI and land use and land cover illustrates that commercial, industrial, and services facilities present a higher temperature at daytime than water, agriculture, and vegetation (Lo *et al.*, 1997). As land cover is measured by vegetation coverage, usually by the normalized difference vegetation index (NDVI), it is proved that there is a negative linear relationship between NDVI and LST (Chen *et al.*, 2006; Li *et al.*, 2011; Lo and Quattrochi, 2003; Weng *et al.*, 2004). Apparently, the replacement of forest and cropland with concrete and asphalt enhanced the development of UHI (Li *et al.*, 2011).

UHI thermal patterns are the subject of research aimed at finding the main contributor to UHI, even though different conclusions have been drawn. Residential areas are considered as the biggest contributor to UHI by Li *et al.* (2011) and Priyadarsini (2009). However, Lo and Quattrochi (2003) show that residential areas have intermediate temperature due to partial coverage by trees. Nichol (2005) concluded that a high density of tall buildings is not the reason causing high temperatures, but the sky view plays a more important role, as the area with a high sky view but no tall buildings such as open spaces and car parks are the hottest areas in built-up area. Li *et al.* (2011) found that even though industrial areas have the highest LST, they are not the main cause of the overall UHI—the biggest contributors are the residential areas.

Thermal image sharpening-related methods are different from the general image sharpening techniques. Kustas *et al.* (2003) developed a method to increase the resolution of surface temperature imagery using vegetation index (VI) techniques. The algorithm relies on the least-squares relationship between NDVI and radiometric temperature. By taking the VI into surface temperature calculations, the minimum computation unit is revised from the pixel size of the thermal image to the pixel size of the NDVI image. In this way, the calculated surface temperature image will have the spatial resolution of the NDVI image. Agam *et al.* (2007) applied this method to sharpen simulated MODIS and Landsat thermal images; the yielded LST has a very low RMSE (about 1 K to 2 K) compared to the field measurement. Jeganathan *et al.* (2011) utilized this method on ASTER and MODIS thermal images, and the sharpened LST

images achieved less than 2 K difference using the aggregated ASTER thermal image as a reference. Using the same principle, Nichol (2009) took a 10 m SPOT 5 NDVI image into the calculation of emissivity, resulting in the generation of a 10 m LST image from a 90 m ASTER thermal image. The sharpened image was highly correlated with *in situ* surface temperature. Downscaling of thermal images is another name used for the technique to improve the spatial resolution of LST images. Hutgens and Vohland (2014) summarizes the general downscaling procedure: the high-resolution image is first aggregated to the coarser resolution of LST data fields, then a regression model is built up to relate input variables to LST data. Afterward, the regression model is applied to the high-resolution input variables to predict LST at high resolution. The difference of various downscaling algorithms depends on which kind of regression model is applied. Possible options include random decision forests (Hutgens and Vohland, 2014), co-kriging (Mahour *et al.*, 2017; Rodriguez-Galiano *et al.*, 2012), linear relationship between LST and impervious percentage (Essa *et al.*, 2013), linear relationship between LST and surface types (Yang *et al.*, 2017), semi-empirical regression (Zhan *et al.*, 2012, 2011), and a pixel block intensity modulation model (Stathopoulou and Cartalis, 2009).

3.2. Using simplified Ehlers fusion to sharpen open source thermal images

The existing thermal image sharpening techniques make use of VI images to improve the spatial resolution of thermal images. Consequently, the resolution of the thermal image can be maximally improved to the resolution of the VI image, which may not be enough for application in urban areas. Additionally, most of these algorithms rely on the linear relationship between LST and VI. Since the consistent relationship between LST and VI may be limited to homogeneous vegetated areas (Hutgens and Vohland, 2014), the methods face difficulties in urban areas which have heterogeneous landscape and mixed surface types.

Simplified Ehlers fusion was developed based on general image sharpening and also works for the spatial improvement of thermal images (see subsection 2.2.4.2). With simplified Ehlers fusion, the spatial resolution of thermal images can be improved to a much higher level, because an image with higher resolution than VI images can be used as input data and the final resolution depends on this input data. Furthermore, simplified Ehlers fusion is not limited to fusing images of homogeneous vegetated areas, as the filter technique within the algorithm can be used to match particular urban features. In the following, this algorithm is applied to sharpen open source thermal images.

The city of Osnabrück, Germany, is taken as the study area of this thesis due to two reasons: Firstly, ground truth data is accessible for the author and this is favorable for the validation of the research results. Secondly, most studies on UHI phenomena are focused on areas where the tropical climate is dominant and with hot summers lasting several months like in Asia (Ngie *et al.*, 2014), or specifically relating to megacities such as Beijing (Zhangyan *et al.*, 2006), Shanghai (Li *et al.*, 2011), Singapore (Nichol, 1996), or Hong Kong (Nichol, 2009, 2005). However, the effect of UHI on cities with other scales and climate is uncertain. In the context of global climate change, extreme heat waves are increasing in frequency and intensity in many European regions (EEA, 2017) which are located in a temperate climate zone. The city of Osnabrück has a population of 169,108 main residents as on December 31, 2018 (Stadt Osnabrück, 2018) and is located in north-west Germany. Whether such a small city in Europe is also influenced by UHI effects is of particular interest.

3.2.1. Thermal images from open geospatial data sources

Satellite thermal images are the most important open source data to analyze UHI phenomena. Table 8 provides an overview of the available thermal data sources for the city of Osnabrück. It is remarkable that several sensors collect thermal data during the night, which is particularly important for UHI analyses as the UHI effect has been considered more obvious at night (Graham, 1993; Nichol, 2009).

Table 8 Available open source thermal images for the city of Osnabrück.

Satellite	Band number	Spectral range in µm	Resolution in m	Availability time for the city of Osnabrück
Landsat 7	6	10.400–12.500	60, resampled to 30	Day and night
Landsat 8	10	10.600–11.190	100, resampled to 30	Day
	11	11.500–12.510		
ASTER	10	8.125– 8.475	90	Day and night
	11	8.475– 8.825		
	12	8.925– 9.275		
	13	10.250–10.950		
	14	10.950–11.650		
Sentinel-3	S7	1.000– 5.000	1000	Day
	S8	5.800–20.000		
	S9	6.500–20.000		
MODIS	20–23	3.660– 4.080	1000	Day and night
	31–32	10.780–12.270		

ASTER: Advanced Spaceborne Thermal Emission and Reflection Radiometer. MODIS: Moderate Resolution Imaging Spectroradiometer.

As the above table indicates, MODIS and Sentinel-3 thermal data have a rather coarse spatial resolution. Considering the studies focusing on urban areas, the spatial resolution of 1 km will not be suitable. Thus, Landsat thermal data were taken into first consideration. Landsat 7 has the issues of stripes (USGS, 2019) which appears as non-value data gaps on the images. At the same time, Landsat 8 has only day time data. Therefore, ASTER nighttime data was also used in this study. Considering the low cloud coverage, low temporal frequency of nighttime data, and the close data acquisition date, the final chosen data were Landsat 7 band 6 with the acquisition date April 18, 2011, Landsat 8 band 10 with the acquisition date February 26, 2015, and ASTER with the acquisition date April 22, 2015.

3.2.2. Data pre-processing

Standard satellite thermal products consist of digital numbers (DN) and need to be converted to temperature value. Usually, it takes three steps to process the raw data. Taking Landsat 8 thermal data as an example, Figure 26 illustrates the data processing procedure and equations (12), (13), and (14) provide detailed mathematical calculations. Firstly, the DN values need to be rescaled to radiances using the rescale factors provided in the respective metadata file. The rescale function is linear, see equation (12), defined by two rescale factors M_L and A_L. Then, the calculated top of the atmosphere (TOA) radiance is converted to TOA brightness temperature using equation (13) with the thermal constant distributed with the raw data. Equation (12) and equation (13) are provided by the Landsat 8 production description (USGS, 2018b, p. 63). Finally, through different atmospheric and emissivity correction algorithms, the temperature of a surface in Kelvin or Celsius can be retrieved. Atmospheric and

emissivity retrieval algorithms based on NDVI have been used extensively (Li *et al.*, 2013; Tan *et al.*, 2017; Weng *et al.*, 2004). The various atmospheric and emissivity correction algorithms are not discussed here because the differences between TOA and LST in urban areas are very small. As Lo and Quattrochi, (2003) argue that "TOA is just adequate for use in surface temperature mapping from thermal infrared images, thus saving an extra computation[al] step". This thesis uses equation (14) (Artis and Carnahan, 1982) as the atmospheric and emissivity correction method because it is one of the simplest.

$$L_{\boldsymbol{\lambda}} = M_L * Q_{cal} + A_L \qquad (12)$$

where $L_{\boldsymbol{\lambda}}$ = TOA spectral radiance (W/ (m^2 × srad × μm))
M_L = band-specific multiplicative rescaling factor from the metadata
A_L = band-specific additive rescaling factor from the metadata
Q_{cal} = quantized and calibrated standard product pixel values, DN

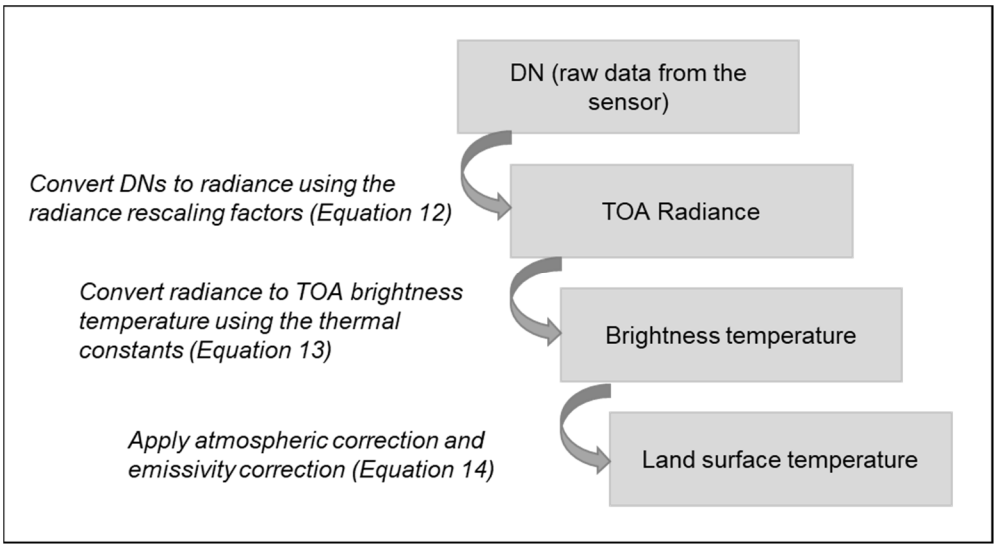

Figure 26 The Land Surface Temperature retrieve procedure adapted from Humboldt State University (2018). DN: digital numbers. TOA: top of the atmosphere.

$$T_B = \frac{K_2}{\ln\left(\frac{K_1}{L_{\boldsymbol{\lambda}}} + 1\right)} \qquad (13)$$

where T_B = top of atmosphere brightness temperature
K_1 = band-specific thermal conversion constant from the metadata
K_2 = band-specific thermal conversion constant from the metadata

$$LST = \frac{T_B}{1 + (\boldsymbol{\lambda} T_B / \alpha) \ln \varepsilon} \qquad (14)$$

where LST = Land surface temperature
$\alpha = 1.438 \times 10^{-2}$ mK
ε = surface emissivity

According to the general workflow of image fusion (Pohl and van Genderen, 2017, p. 74), the image sharpening should take place after the atmospheric correction process. However, this only works when using a panchromatic image to sharpen multispectral images. Because after

atmospheric correction, both data sets consist of surface reflectance values (range from 0 to 1) which are dimensionless. In case of atmospheric correction of thermal images, the pixel values of the corrected image will be in Kelvin or Celsius. If using an atmospheric corrected panchromatic image (dimensionless) to sharpen the temperature image, the units of the value range of two image sets are different, which can lead to unexpected results.

Therefore, it needs to be reconsidered when data fusion should be conducted during the atmospheric correction procedure. Figure 27 shows the unit changes of the panchromatic and thermal image in the process of atmospheric correction. In this process, the images can be divided into three levels: DN level, radiance level, and reflectance level. The thermal image and pan-image have the same pixel value range only at the first two levels, which means it is possible to fuse the two images. However, the thermal image is in Kelvin or Celsius and the panchromatic image is dimensionless at the reflectance level, which means it is not suitable for pan-sharpening. Within the first two levels, there is no difference when fusion is implemented. Because from the first level to second level, only a linear equation is applied to rescale the DN values to radiance. In the end, in this thesis, data fusion is carried out on the first level, where images still have DN as their pixel values. In this way, the downloaded raw images can be directly used for pan-sharpening. It is more convenient and time efficient.

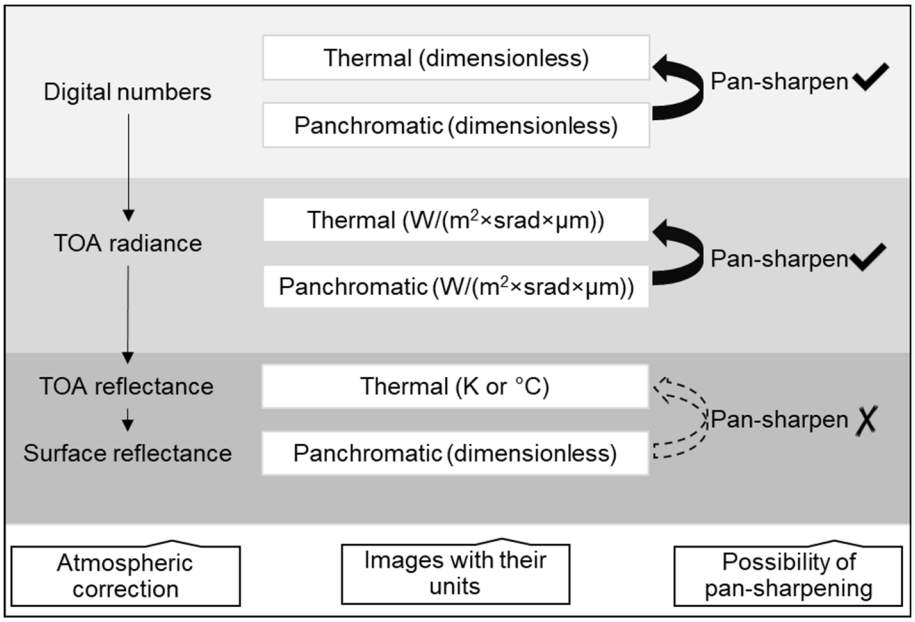

Figure 27 The change of pixel value units during the atmospheric correction procedure and possible data match for pan-sharpening.

3.2.3. Data fusion process using simplified Ehlers fusion

In this section, simplified Ehlers fusion is applied between Landsat 7, Landsat 8, and ASTER images, aiming to improve the spatial resolution of thermal images at daytime and nighttime, to be used in UHI analysis.

3.2.3.1. Sharpening Landsat 8 thermal image using Landsat 8 panchromatic image

Landsat 8 currently provides the highest resolution of thermal images from both daytime and nighttime. However, as mentioned before, there is no Landsat 8 nighttime data available for

Osnabrück, thus only the daytime data is used here. The simplified Ehlers fusion was applied to Landsat 8 band 8 and band 10.

The thermal image needs to be resampled to the same resolution as the panchromatic image in the first place, to avoid mismatch of pixels caused by image clipping with different resolutions. This was done by using the QGIS raster align tool, which generally includes four steps: re-projecting to the same coordinate system, resampling to the same cell size and offset in the grid, clipping to a region of interest, and rescaling the values when required (Documentation QGIS Testing, n.d.). Here, cubic convolution was selected as the resampling method. To find a suitable low-pass filter, the selected area of interest has 512×512 pixels following the experiments in section 2.2.2.

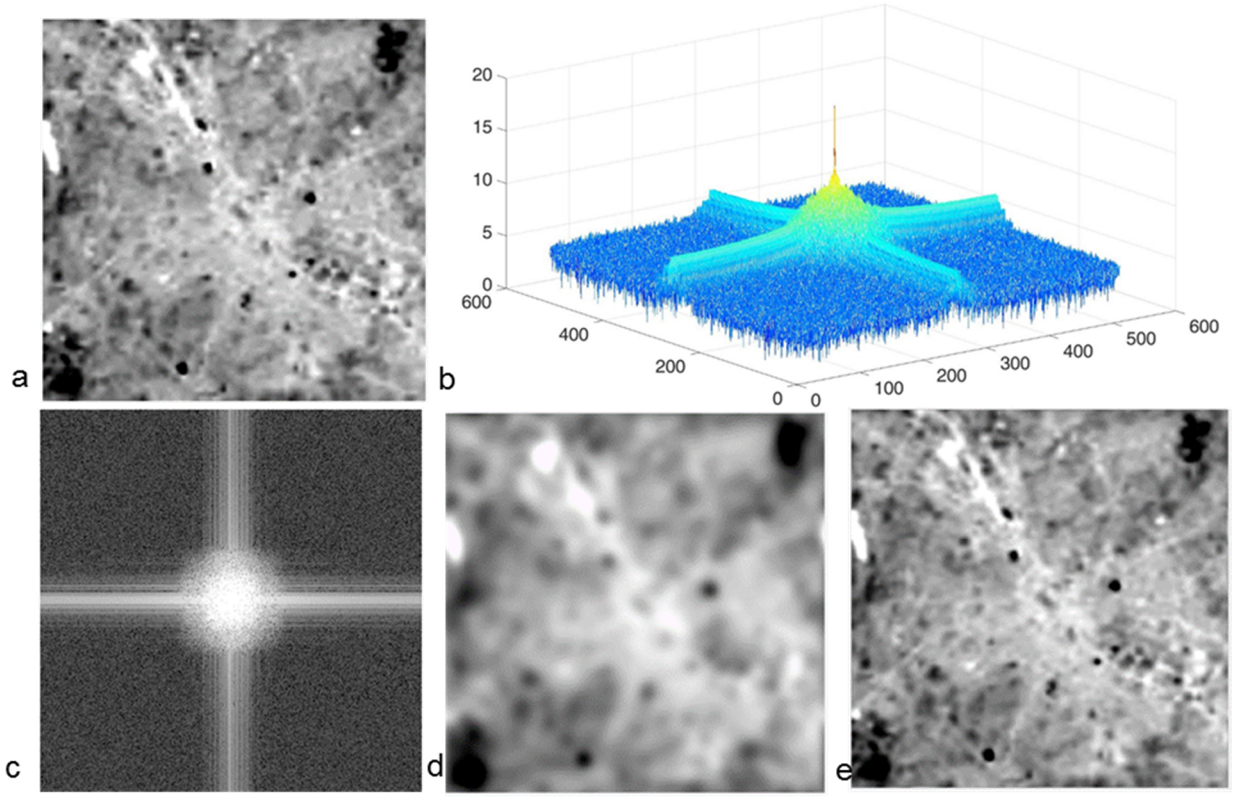

Figure 28 The procedure of adjusting low-pass filter for thermal images; (a) original thermal image; (b) power spectrum of the thermal image in frequency domain; (c) 2D display of (b); (d, e) filtered images when filtered with cut-off frequency of 10 and 50 respectively.

The selected test area was transformed into the frequency domain using an FFT. The low-pass filter selecting procedure is illustrated in Figure 28. The frequency distribution of the thermal image was inspected in the 3D power spectrum. Then, a low-pass filter with a cut-off frequency of 10 was first applied. The filtered image was very blurry, meaning that too much thermal information was lost. Then, the low-pass filter was adjusted to a cut-off frequency of 50. With this filter size, the filtered image kept almost all of the information of the original thermal image. Thus, a low-pass filter was taken with a cut-off frequency of 50.

Subsequently, the high-pass filter was also tested. After transforming the pan-image into the frequency domain, it showed that the low frequencies were concentrated in a rather small range. The high-pass filter was tested with cut-off frequencies of 50, 100, and 200 separately. The filtered results showed a cut-off frequency of 50 retained much undesired information; from a

cut-off frequency of 100 to 200, fewer linear features were left. Until a cut-off frequency of 200, enough information was kept as high-resolution input.

Afterward, a direct band-pass filter was tested. It started with an inner radius of 50 and bandwidth of 50, as this filter setting produced the perfect filtering effect on the aerial photo in section 2.2.2. However, even with the same image size as the castle image, artifacts appeared in the filtered image. A possible explanation is that the pan-image had a spatial resolution of 15 m which was much coarser than the 0.5 m resolution aerial photo. Here, it can be concluded that the spatial resolution will influence the selection of the filter size. In the end, the band-pass filter was adjusted to an inner radius of 100 and a bandwidth of 100. The artifact effect was reduced, but still occurred on the filtered image. Then, the inner radius was further modified to 10. The final setting for the band-pass filter was an inner radius of 10 and a bandwidth of 100. Clearly, it is more complex to choose a suitable band-pass filter than a suitable high-pass filter. Figure 29 shows the original image and the band-pass filtered result.

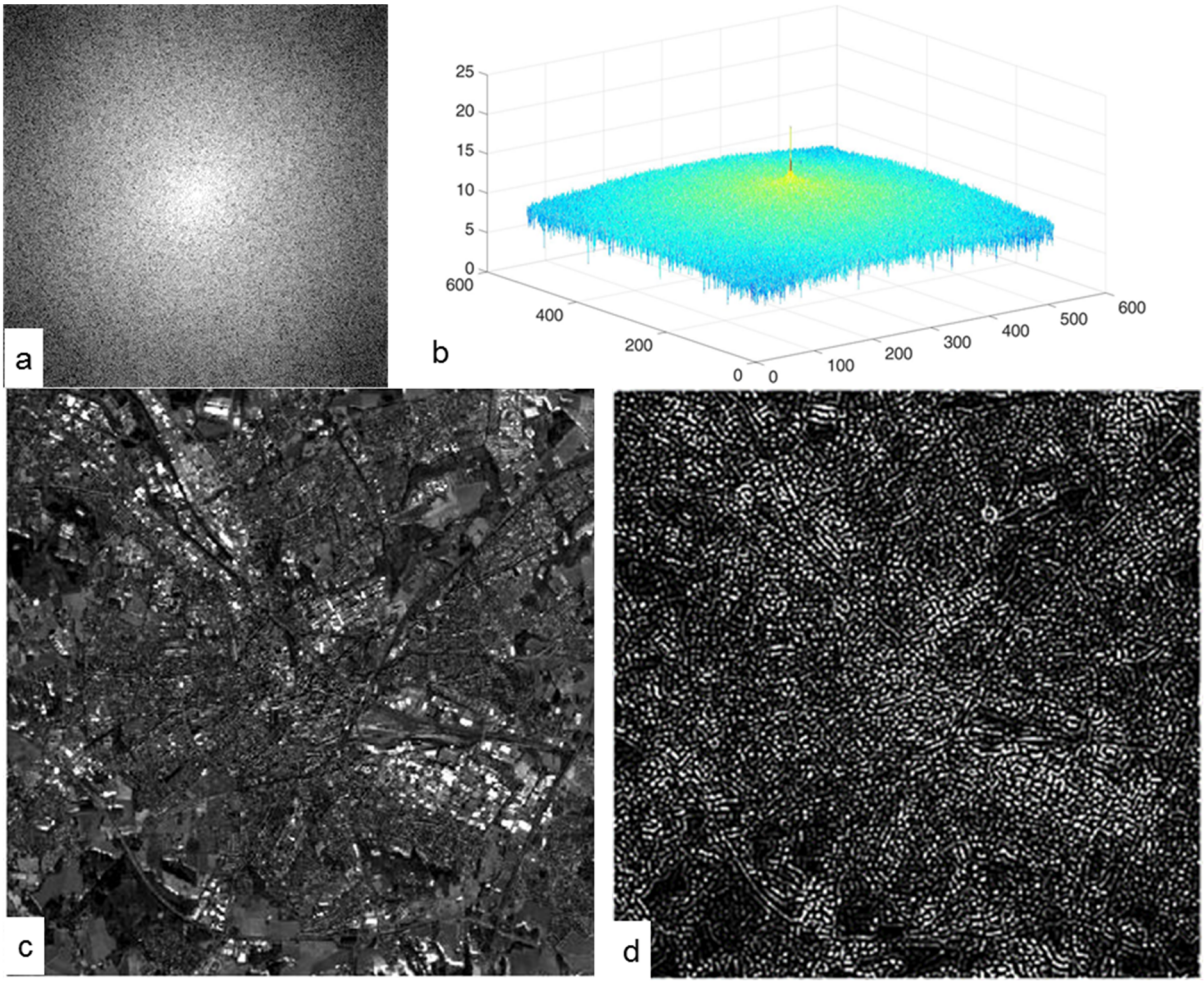

Figure 29 Results of adjusting band-pass filter for panchromatic images; (a, b) power spectrum of the panchromatic image in 2D and 3D respectively; (c) original panchromatic image; (d) filtered image when using band-pass filters with an inner radius of 10 and width of 100.

Subsequently, the indirect band-pass filters were also tested. As it was described in section 2.2.2, the same filtering effect can be reached through both indirect and direct band-pass filters. Therefore, the similar filter size adjusting procedure and filtering results are not repeated here. In the filter test, the focus area has 512 × 512 pixels. When applying the filter to

the complete study city which has 1140 × 901 pixels, the size of the filters needs to be adapted again correspondingly. In the case of the indirect band-pass filter, it was adapted to the cut-off frequency of 420 and 450.

To pursue the best fusion results, a histogram matching technique was also tested here. Histogram matching has been used widely in image sharpening algorithms, such as Wavelet-IHS fusion and Wavelet-PC fusion (indicated by the workflow of the fusion algorithms described by Pohl and van Genderen (2017, subchap. 4.7). Commonly, the histogram matching technique transforms the high-resolution image so that the histogram of the output image approximately matches the histogram of the low-resolution image. Then, the histogram-matched image is taken as the actual input to perform image sharpening. MATLAB provides a tool *imhist* to approximately match the histogram of target images (MathWorks, 2019). Figure 30 shows the histograms of resulted images where *imhist* was applied. With histogram matching, the fused image was closer to the original than without histogram matching.

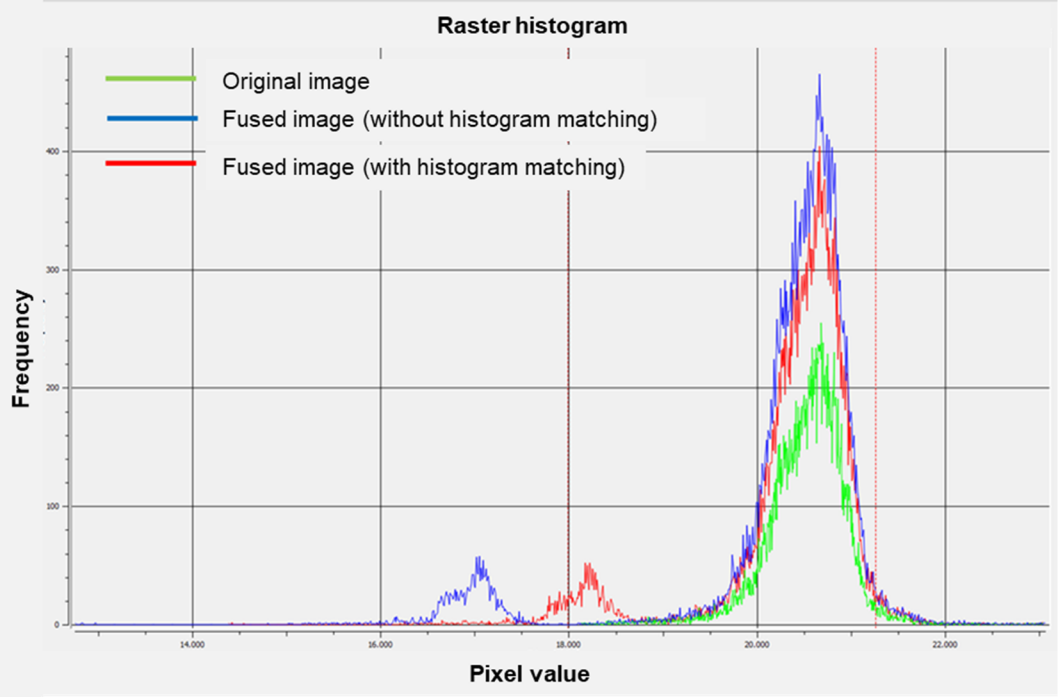

Figure 30 The comparison of histograms between the original and fused images with and without histogram matching.

However, histogram matching only works perfectly when all input images are band bundles. The images were obtained at the same time under the same atmospheric conditions in the case shown in Figure 30: the panchromatic image and thermal image used were band bundles from Landsat 8. On the opposite side, when the input images were from different sensors with different acquisition times, the histogram matching produced unexpected results.

For example, a Landsat 8 panchromatic image and a Landsat 7 thermal image were taken as input and histogram match was applied in the fusion procedure. Figure 31 shows the comparison between input data and the fused result. In the panchromatic image, there are parts covered by the shadow of clouds as well as the shadow of forests, which do not appear in the thermal image. After fusion, these shadows were highlighted in the fused image. These are the undesirable fusion effects generated by histogram matching.

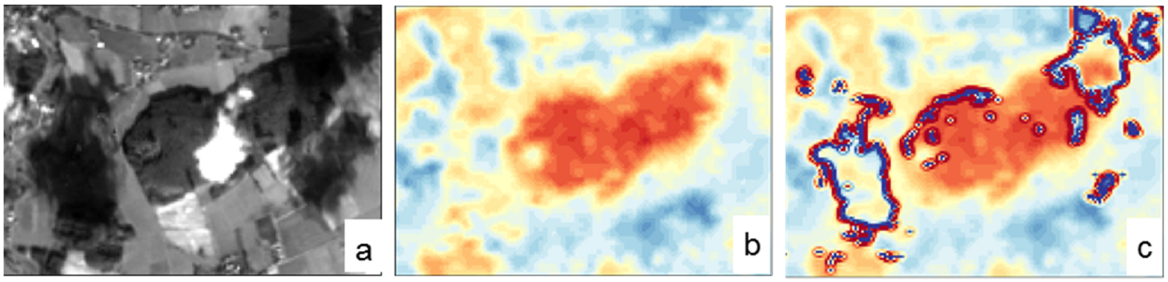

Figure 31 Histogram matching highlighted shadows in the fusion result: (a) original panchromatic image; (b) original thermal image, and (c) fused image with histogram matching.

Therefore, to make it more flexible for the various open data sources, histogram matching was not applied in the simplified Ehlers fusion algorithm. This aspect was not discussed in chapter 2 because the test images were not influenced by the atmospheric condition.

The final fused image is shown in Figure 32a. The color legend displays from blue to red, indicating temperature from low to high. Taking a close look at the city core, obvious spatial improvement and color preservation has been reached compared to the original image (Figure 32b and Figure 32c). Spatial details such as railways, road infrastructure, and urban blocks, which could not be seen before fusion, can be easily recognized in the fused image. Meanwhile, the thermal distribution was retained as in the original, as shown in both Figure 32b and Figure 32c there are two blue dots indicating the lowest temperature, and a large red area indicating the highest temperature. All the temperature information has been successfully transformed into the fused image.

The fusion effects on spatial reinforcement are even more obvious when the original and fused images are further clipped with a building footprint layer (Figure 32d and Figure 32e). The spatial resolution of the original thermal image is too coarse for the clipped results to fit the outline of many buildings, whereas the clipped result from the fused image can illustrate the temperature difference between the buildings.

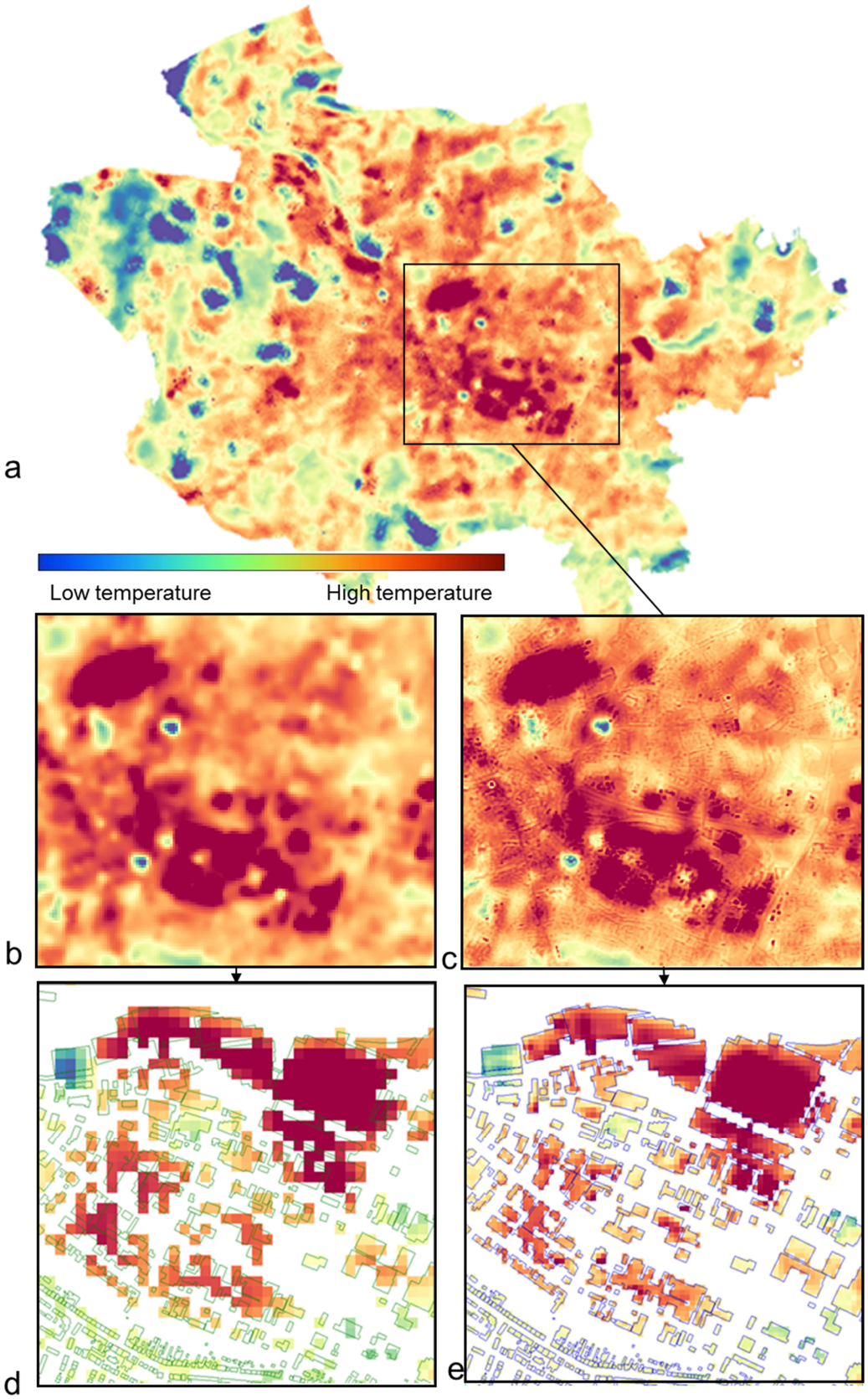

Figure 32 Comparison between the fused thermal and the original image: (a) overall fused image; (b, c) magnified city core from the original image and the fused image respectively; (d, e) clipped results from the original image and the fused image respectively.

The fusion effect was also investigated in a magnified vegetated area, shown in Figure 33a. The data fusion process has enhanced the lines and edges in this area, which are mostly borders of the forest and agricultural fields. Through data fusion, the temperature difference between forest and farmland could be distinguished.

In chapter 2, it was mentioned that the goal of image sharpening is to introduce the spatial details into the fused image, while at the same time keeping the original color information. Figure 33 shows an example where this goal was achieved. There are two different agricultural fields but with the same temperature. In the original image, this area is displayed as one piece of homogeneous land due to a similar temperature. After fusion, the two agricultural fields can be distinguished. The fusion process introduced the border between these two fields while keeping the original color pattern.

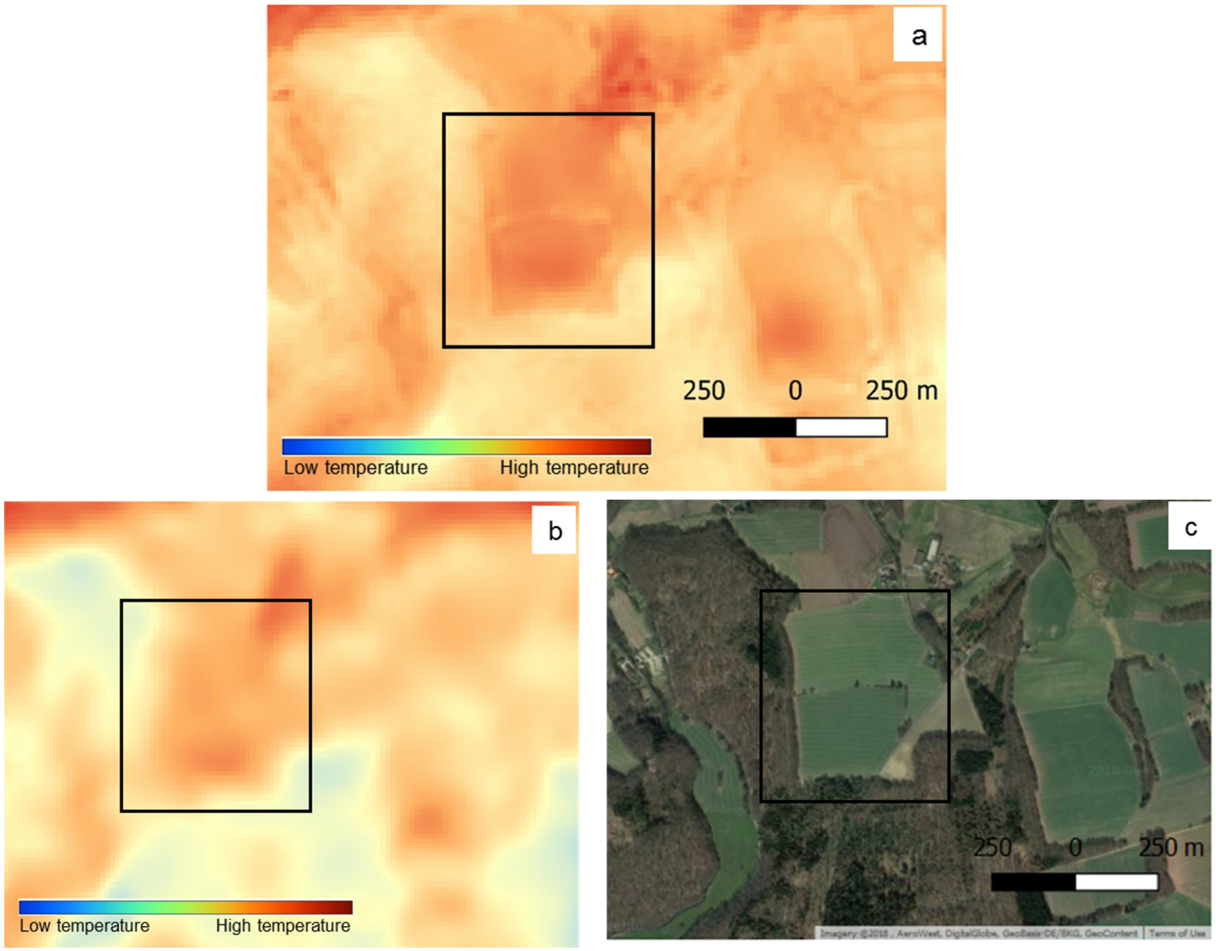

Figure 33 Fusion effect investigation in a vegetation area: (a) fused image, (b) original image, and (c) area shown in Google Maps.

3.2.3.2. Sharpening ASTER thermal image using Landsat 8 panchromatic image

The ASTER nighttime thermal band 13 was used for the study area. Since there were no panchromatic images available during the night, the panchromatic image used in the subsection 3.2.3.1 was applied. The fused results showed that the clouds from the panchromatic image were also transformed into the thermal image, even though there were no clouds before. The clouds had no impact on the fused Landsat 8 thermal image in subsection 3.2.3.1 because the clouds appeared at the same location in all the input images. It resulted in a strong impact due to the following reasons: Firstly, regardless of clouds, vegetation fields, or built-up areas,

the fusion algorithm considers them as identical important features. Through image sharpening, the spatial details of these features could be enhanced to a certain extent depending on the selected filters. Secondly, in the fused Landsat 8 thermal image, the clouds could have been enhanced but did not become a problem because they were features in both original and fused thermal images. Finally, in the fused ASTER thermal image, the clouds influenced the overall appearance of the fused image to a large extent, because compared to the original ASTER thermal image the clouds added unnecessary features.

To reduce the influence of the clouds, the size of the high-pass filter was adjusted from 500 to 700, then to 800, where the complete image has 1141 × 902 pixels. From the fused image (Figure 34b, Figure 34c, and Figure 34d), it can be seen that the impact of clouds is gradually reduced but are not completely erased. To point out the locations where clouds exist, the grayscale panchromatic image is shown with pseudo-color where clouds are highlighted in red.

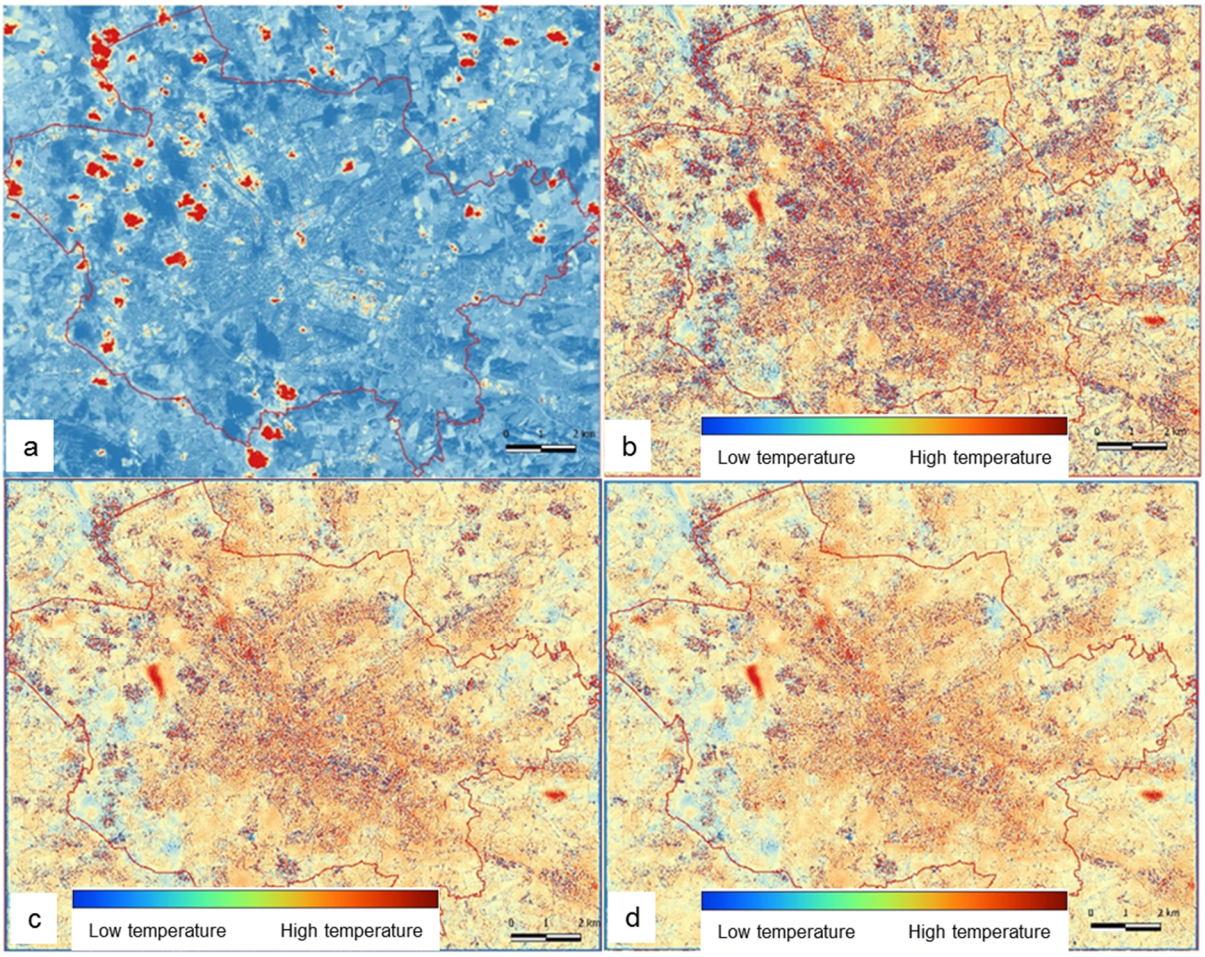

Figure 34 Adjustment of filter size to reduce the influence of clouds: (a) pseudo color panchromatic image which was covered by clouds which affected the fused image; (b, c, d) fused images by adjusting the size of the high-pass filter to 500, 700, and 800 respectively.

Even when obscured by the clouds, the fused images still kept the original temperature distribution of the ASTER thermal image. When taking a closer look at places where a water body is located (Figure 35) in the original thermal image, the water body stands out from the surroundings due to their highest temperature. After fusion, the water body remains the warmest feature in this area. Similarly, the other parts in blue and orange were maintained in their original color pattern in the fused image. In the pan-image, the borders of several features, such

as the agricultural fields, streets, roads can be seen). These linear features do not exist in the thermal image but are recognizable in the fused image.

Comparing Figure 35c and Figure 35d, the impact of the panchromatic image on the fused image was reduced by the increase of the size of the high-pass filter from 500 to 800. Comparing the results produced from these two filters, in the first one, the influence of the pan-image is more dominant, thus resulting in stronger linear features. In the second image, the ASTER thermal image color pattern is more obvious and thus closer to the goal of image sharpening.

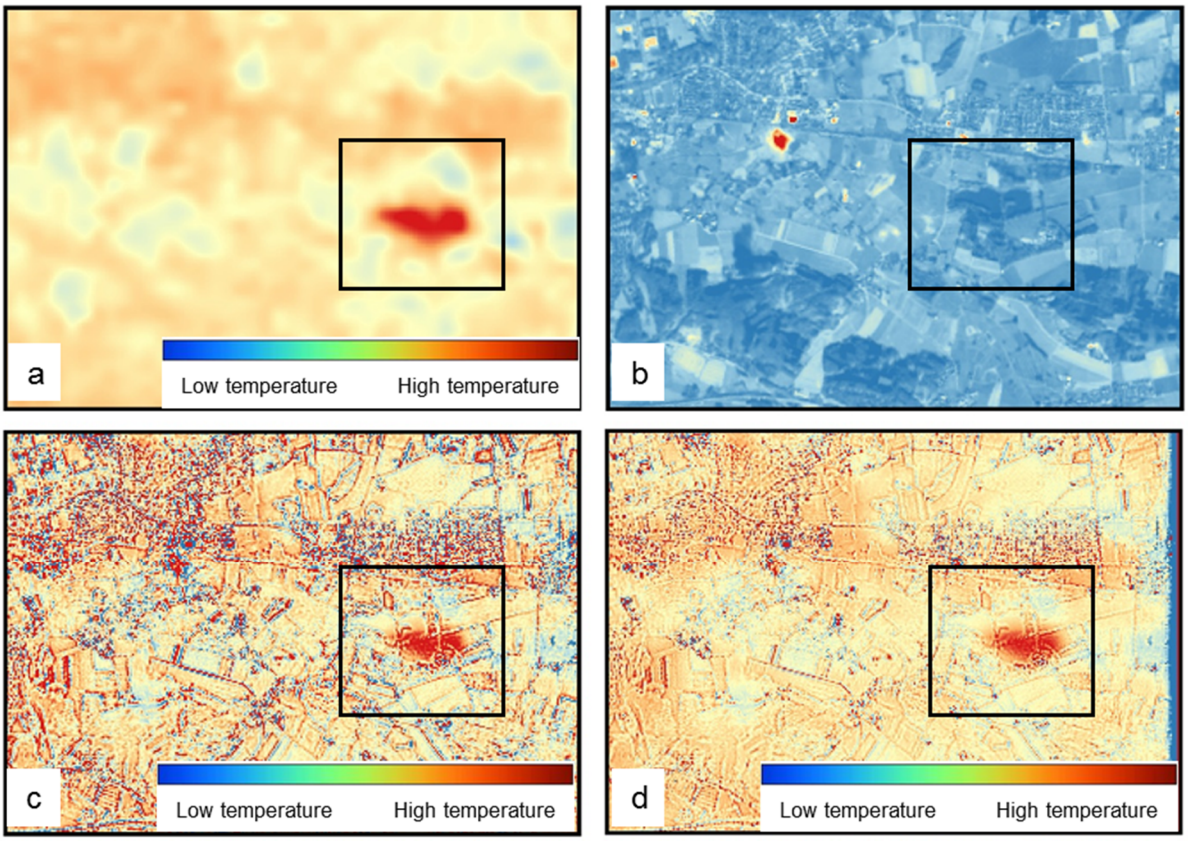

Figure 35 A close inspection of the fusion effect: (a) original ASTER thermal image; (b) pseudo color Landsat 8 panchromatic image; (c, d) fused images using a high-pass filter with a size of 500 and 800 respectively.

As the fused image Figure 34 was heavily influenced by clouds, another Landsat 8 panchromatic image without clouds was taken into the test. This time, the fused image (Figure 36a) shows that at the northeast corner of the image, some strong lines and edges appear. But there were no similar features that could be distinguished in the original ASTER image (Figure 36b). With closer inspection of this area in the panchromatic image, it was found that this area consisted of farm fields covered by snow. Like clouds, the features representing snow were also introduced into the fused image. Figure 36c uses pseudo color to present a panchromatic image where snow is highlighted in red.

It is possible to find a panchromatic image which is not covered by snow or cloud, particularly during summer time. However, the ASTER thermal image was taken in the cold season. Land use and land cover will be different during cold and warm seasons. The literature review from subchapter 3.1 reveals that LST is strongly related to land use and land cover. Since during cold

seasons, the city is often covered by clouds or snow, the test was not further continued with another panchromatic image.

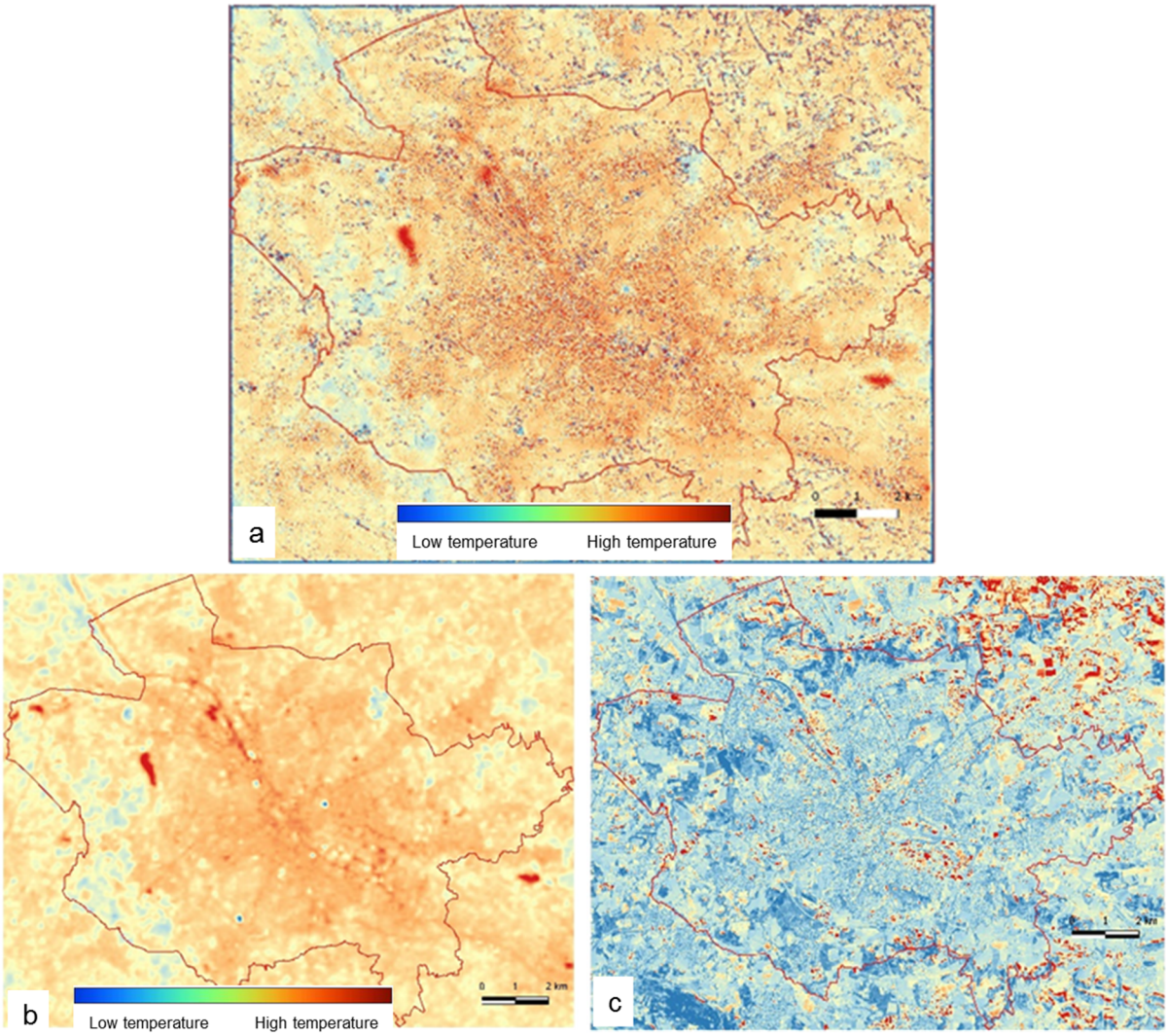

Figure 36 Fusion effect influenced by snow: (a) fused ASTER thermal image: (b) original ASTER image; (c) pseudo color panchromatic image where snow is highlighted in red.

3.2.3.3. Fusion between a Landsat 8 panchromatic image and a Landsat 7 thermal image

Since May 31, 2003, the Landsat 7 scan line corrector failed. Thus, the produced data have data gaps which are represented as stripes in the image (Figure 37). Using the FFT, the stripes appear as energy bursts occurring in 135° of the vertical axis in the Fourier spectrum (Figure 37b). If a low-pass filter was applied to the image, the filtered image kept or even widened the stripes (Figure 37c). Without destriping, the fused results were heavily influenced (Figure 37e). For destriping, another image was needed with close acquisition time to fill in the data gaps. However, as Landsat 7 does not often take global nighttime data, it is hard to find another thermal image suitable for the study area. It might be possible to remove the stripes using notch reject filters, which is beyond the research scope of this work and was therefore not applied.

Even the fused image was strongly influenced by the stripes, where the color pattern of the original image was preserved. The city center had a higher temperature than the surrounding vegetation area. The urban spatial features such as railways and roads were also enhanced in the fused image. However, Figure 37e shows that these line features are so strong that in

contrast, the thermal pattern becomes less dominant. This could be changed by adjusting the size of the filters. When the cut-off frequency was set as 800 for both high-pass filter and low-pass filter, the result was what Figure 37e shows. If the cut-off frequencies for both filters were altered to 50, in the fused image the thermal pattern got stronger, but the stripes were stronger as well. The overall result was even worse than Figure 37e shows and thus is not presented here.

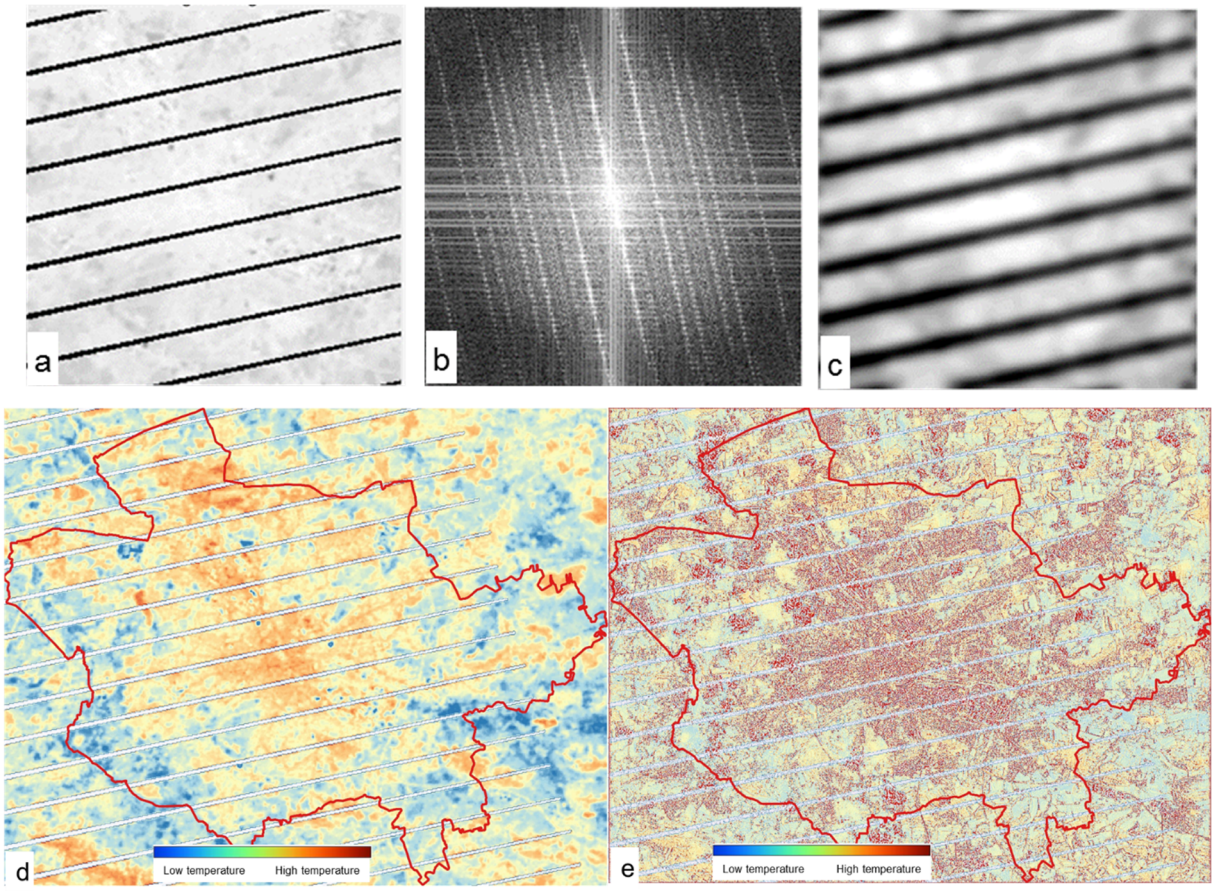

Figure 37 Data fusion between a Landsat 7 thermal and a Landsat 8 panchromatic image: (a) original thermal image in grayscale; (b) Fourier spectrum of the original image; (c) filtered thermal image using low-pass filter; (d, e) original and fused thermal images respectively.

3.3. Fused thermal image used for urban heat island analysis

The above fused images from the Landsat 8 panchromatic and thermal bands were used for daytime UHI analysis while the fused images from Landsat 8 and ASTER were used for nighttime analysis.

3.3.1. Urban heat island effect during daytime

The city of Osnabrück is situated in a valley between two forested hills, namely Wiehen Hills and Teutoburg Forest. Figure 38 shows a transect running across the land surface temperature image taken in a hot season (June 14, 2017), specifically from the north forested hills to the south forested hills which passes through the city center. The profile suggests a significant UHI effect in the hot seasons. Temperatures were higher throughout the urban areas and temperatures were lower in the surrounding areas. The temperature difference between urban

and rural areas or suburban areas was about 5 K on average. Compared to the forested hills, the urban areas were nearly 10 K warmer (see Figure 38).

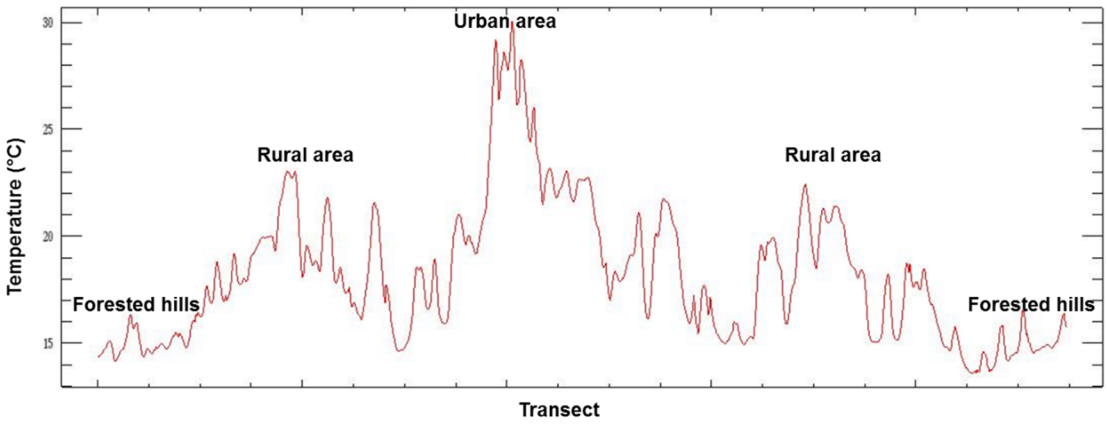

Figure 38 Land surface temperature transect at daytime in the hot season across the city of Osnabrück.

Figure 32a shows the overall surface temperature of the city of Osnabrück during daytime in the cold season (February 26, 2015). In such cold background, industrial sites stand out as the hottest sites in the city. It can be expected that in summer, these sites will have an even higher temperature with additional energy absorbed from the sun. Built-up areas including the city center, residential areas, and the transportation system show a higher temperature than vegetation areas. The coolest areas are found in water bodies.

In agricultural and forested mixed areas, forest always appeared cooler than agricultural fields. Larger agricultural fields showed a slightly higher temperature than those of smaller size. The size has the opposite influence on forests; the larger ones present slightly lower temperatures than those of smaller size.

Woodland within urban areas showed similar temperature as the forest in adjacent rural areas and much lower temperature than the built-up area. This makes the wooded land in the urban area appear as a cool island and a heat sink.

Overall, the built-up surface showed the widest distribution of high temperature. For a closer investigation of the thermal patterns in the built-up environment, the fused image was further clipped by a building footprint layer which represents most of the built-up area. The overall temperature map of buildings is shown in Figure 39. Without vegetated surface, the temperature difference within the built-up area could be easily distinguished.

Industrial areas show even more outstanding high temperature on the building temperature map. Taking the three hottest sites (marked as ❶, ❷, and ❸) into closer consideration, it was found that all three were industrial or industry-related areas. The first hotspot was where the company KME Germany GmbH & Co. KG is located. It is a large enclosed factory campus where copper and brass is produced. Within the factory campus, factory workshops are densely distributed. The high temperature was mainly caused by industrial waste heat, and further enhanced by the dense building structure which trapped heat (Figure 40).

Figure 41 shows the second location. It is near to the main train station, where many factories, as well as service and commercial companies are located, due to the convenient access to the

transportation system. The biggest building in the image has the highest temperature in this area. It is a car storage building without a roof from the car manufacturer Volkswagen Osnabrück GmbH. The lack of roof protection together with the building material both contributed to the high temperature. The overall high temperature of this entire area was partly caused by industrial production, and partly because of low green coverage. The whole surface is sealed within this area and almost no vegetation is visible.

The third location is an isolated factory surrounded by a vegetated field. It is the Felix Schoeller Holding GmbH & Co. KG which produces photographic and digital printing papers. It produced a hot spot in the nearby residential area. The east side of the factory was slightly cooler than the west side (Figure 42a), which resulted in cooler buildings on the right side and hotter ones on the left side (Figure 42b). This might be the case because the forest and empty farm field are located on the right side and left side respectively, which means that the forest could cool down the hot temperature produced from the industrial building.

Other industrial areas with a smaller size also showed high temperatures. There were also industrial companies located at low-density built-up areas. Even in such areas, if an industrial factory was present, the detected temperature was higher.

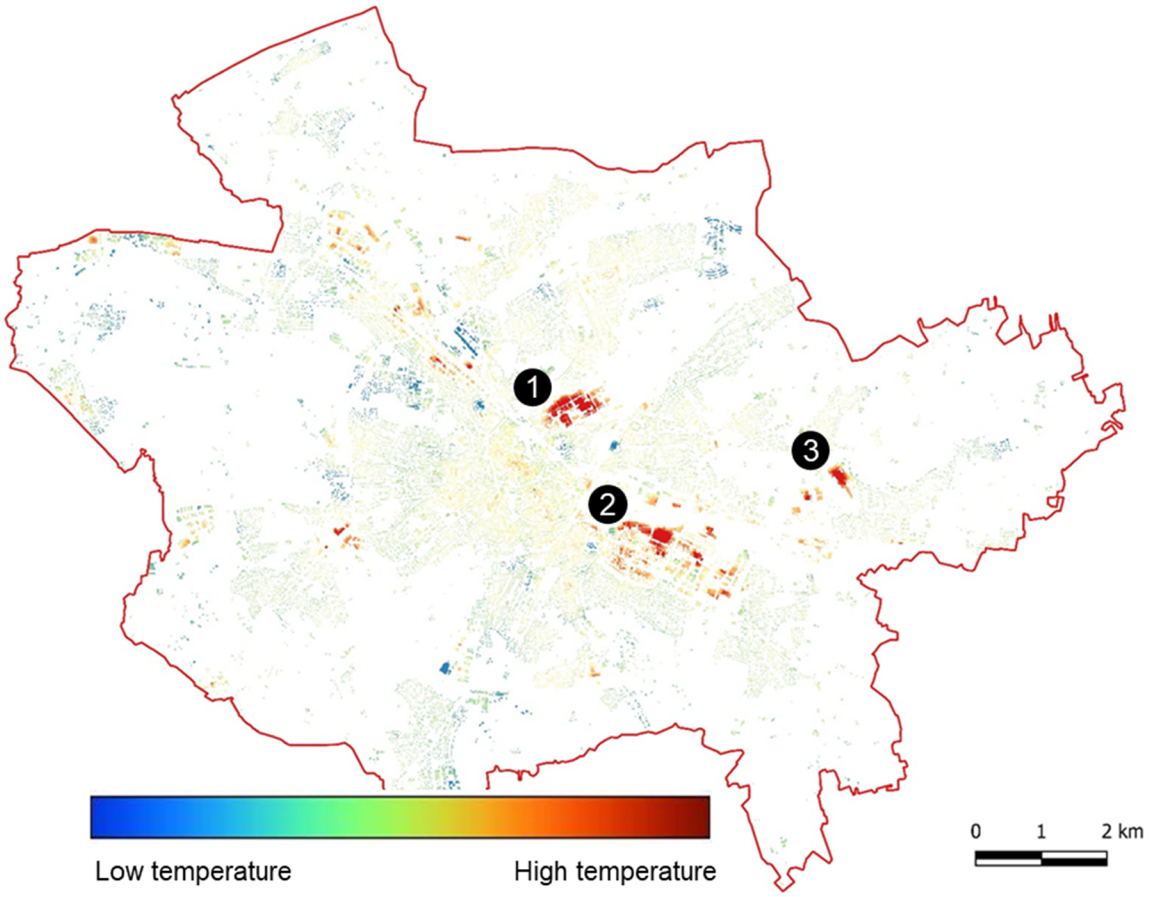

Figure 39 Building temperature during daytime in the cold season in the city of Osnabrück.

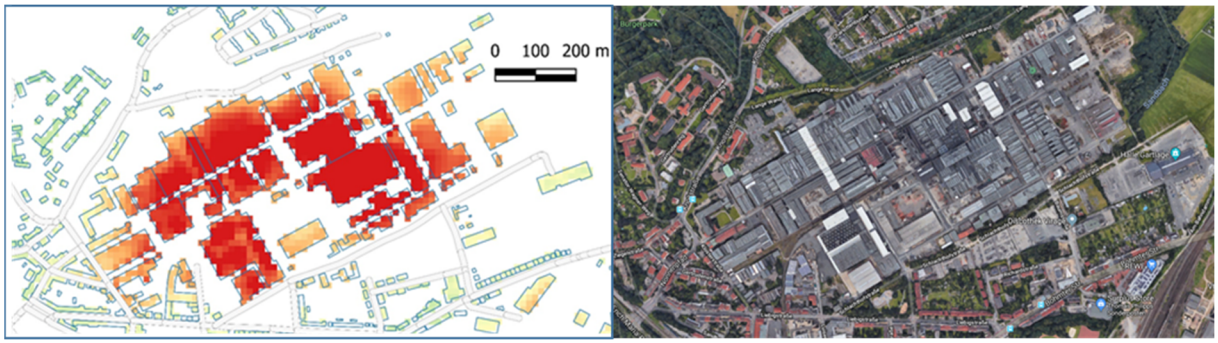

Figure 40 The high building temperature of a metal producing company and its appearance in Google Maps.

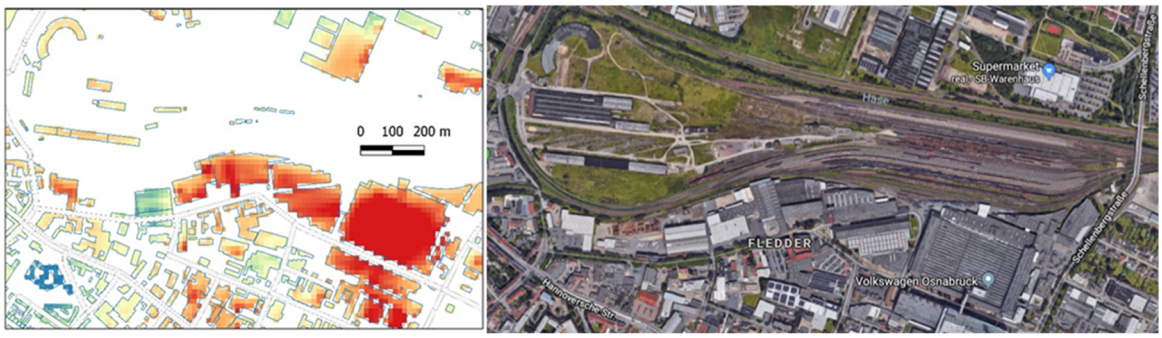

Figure 41 The building temperature of a dense industrial and commercial area near a train station and its appearance in Google Maps.

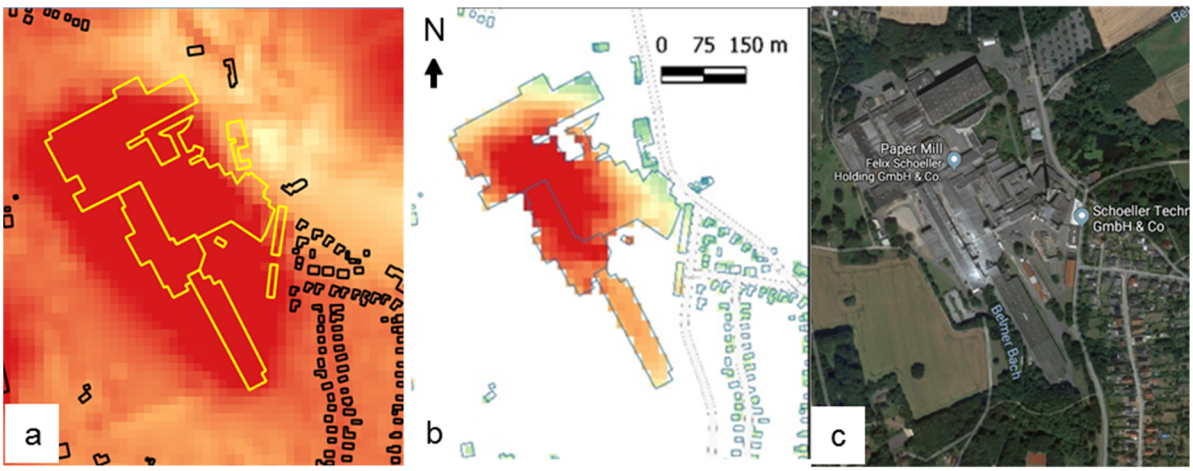

Figure 42 An industrial factory where high temperature was cooled down by the forest on the right side: (a) thermal distribution of all land cover in the industrial area; (b) building temperature of this area; (c) appearance of this area in Google Maps.

Non-industrial buildings show temperature dropping from the city center towards suburban areas, along the direction of the urban fabric extension (Figure 43). This is decided by the urban spatial structure of the city, which spreads outward from a central city ring. Within or near the city ring, businesses, commercial entities, public services, and university buildings are densely built-up, leading to high temperatures. In Figure 32a, two sites within the ring present comparatively lower temperatures; one is a public park named Schlossgarten, and the other is a vegetated river bank area beside the river “Hase”.

The residential buildings close to the city ring are also influenced by the high temperature. Further away from the city ring, the temperature decreases. Exceptions include a hospital, a

shopping center, the furniture shop “IKEA”, and vehicle marketplaces which are far from the city centre but exhibit high temperatures.

Figure 43 Temperature distribution of non-industrial buildings in the city of Osnabrück.

3.3.2. Urban heat island effect during nighttime

Figure 44 shows the thermal transect across the city and surrounding areas at night during the cold season (April 18, 2011). The average difference between urban and surrounding areas was about 2 K, which is much less than in summer time. Despite this, the UHI effect was still visible by the average warmer local climate of the urban blocks indicated by the fused ASTER image. The higher temperature distribution followed the urban fabric extension. At night, the water bodies showed the highest temperature in opposite to daytime. The open agricultural land presented the lowest temperature. Other than the city center, the contrast between built-up areas and woodland was not as strong as it was at daytime. A remarkable fact shown in the night thermal image is that the main streets, roads, and highways could be clearly seen due to their significantly higher temperature. This was because of the properties of the road surface material, which has high heat storage capacity. During the daytime, this phenomenon was not obvious because of the same high temperature from the surrounding urban blocks. However, the heat contribution from the streets should not be overlooked as a source of UHI.

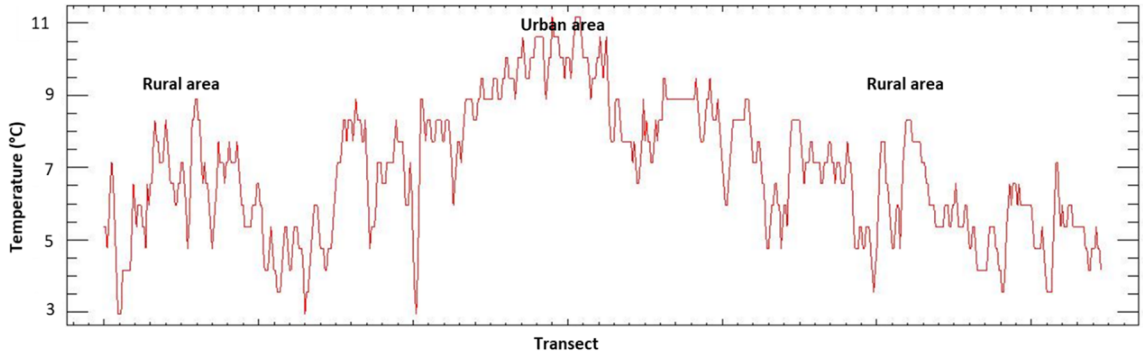

Figure 44 Land surface temperature transect at nighttime in the cold season across the city of Osnabrück.

Figure 45 shows that within the built-up areas, the extremely high temperature from industrial areas was absent at night. They presented the same or even lower temperature than the city center. Considering that the nighttime data was taken at about 9 pm, and industrial activities usually stop at 6 pm, the generated heat had been dissipating for 3 h by that time. However, industrial areas still remained slightly warmer than residential areas. The temperature difference

between buildings illustrates that built-up areas close to the city border were much cooler and the city center remained the warmest site. In general, in the cold season the correspondence between temperature and land use was less distinguishable than by day.

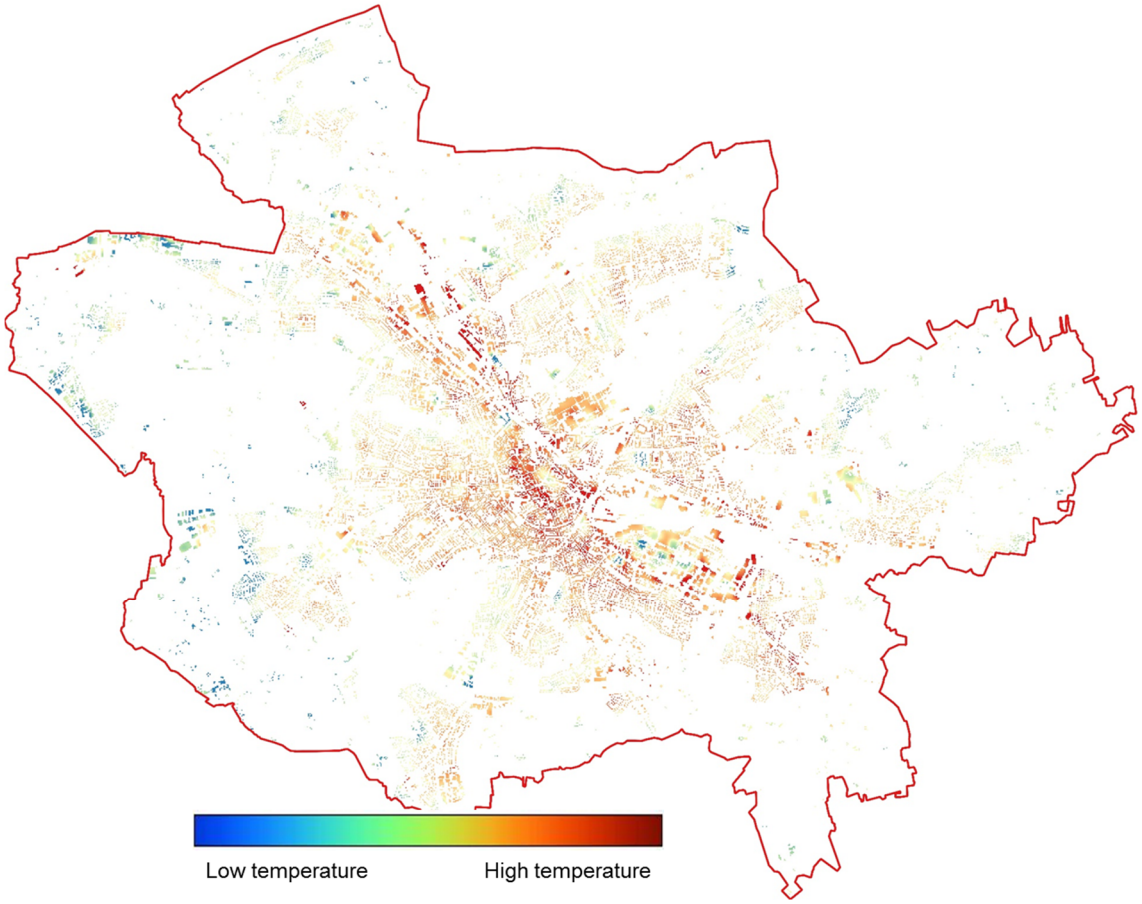

Figure 45 Building temperature map at nighttime in the cold season in the city of Osnabrück.

3.4. Urban heat island mitigation strategy based on data fusion results

Based on the fused images and the above analysis, the main factors contributing to the UHI effect in the city of Osnabrück are identified.

Anthropogenic heat introduced by industrial processes had the highest temperature and large distribution in the urban area. Even after operation ceased, it took time to cool down and continued to influence the evening temperature. Therefore, it is considered as the dominant heat source for the UHI effect of the city. The heat generated from industrial factories come mainly from the machines used for production. Most of the heat is released into the air and becomes waste heat because it is often considered as low-grade and difficult to harness for utility. In the last decade, many investigations into using industrial waste heat have been carried out. In Qatar for example, industrial waste heat has been used for fresh water production (Khraisheh *et al.*, 2013). Wagner (2004) presented two energy saving systems which can be used for industrial waste heat and described the operational experience. Depending on the industrial process, various options can be considered for waste heat conservation, such as waste heat recovery from steam boilers, coffee roasters, and chemical reactor exhaust (Bhattacharjee, 2010). Waste heat can also be stored and reused in the same way as the thermal energy storage of solar energy systems (Demirbas, 2006).

Road surfaces highly contribute to the development of UHI, indicated by the nighttime thermal image. The high temperature of paved surfaces can be reduced through pavement cooling techniques, including the following methods (Santamouris, 2013): (a) Increasing the albedo of the paving surfaces by using conventional cement concrete pavement, concrete additives like slag cement and fly ash, white topping, roller compacted concrete pavement, and light aggregates in asphalt concrete surface. (b) Increasing the permeability of the surfaces in order to decrease their surface temperature through evaporation processes. (c) Increasing the thermal storage capacity of the surfaces by adding ingredients or materials of high thermal capacity. (d) Using external mechanical systems to cool down the pavement materials. (e) Providing efficient shading of the paved areas, which can also make the outdoor pedestrian or driving environment more comfortable.

Dense urban fabric strongly influences the formation of UHI both during day and night. The heat distribution starts from downtown, then extends following the urban fabric in all directions. There have been many attempts to reduce the heat from urban blocks in order to mitigate the UHI effect. Akbari *et al.* (2015) provide an overview of the main technologies. Development of reflective materials has been intensively discussed. The material used in built-up areas absorb incident solar and infrared radiation and release the heat into the atmosphere, increasing temperature. The so-called "cool roof" can reflect some of the solar radiation, thus preventing overheating of the urban areas. Typically, the "cool roof" surfaces are clean, smooth, solar-opaque, and in light colors. The high solar reflectance value of silver-colored aluminum flakes makes them suitable for such applications. Figure 46 shows four examples of buildings with this kind of roof. They appear as "cold" spots in thermal images from Landsat 7, Landsat 8, and ASTER due to their reflective roofs. The polished shiny surface has extremely low emissivity in the wavelengths between 8 μm to 14 μm that is difficult to be detected by the thermal sensors. Therefore, these kinds of buildings will show up as "cold" spots despite their high temperature.

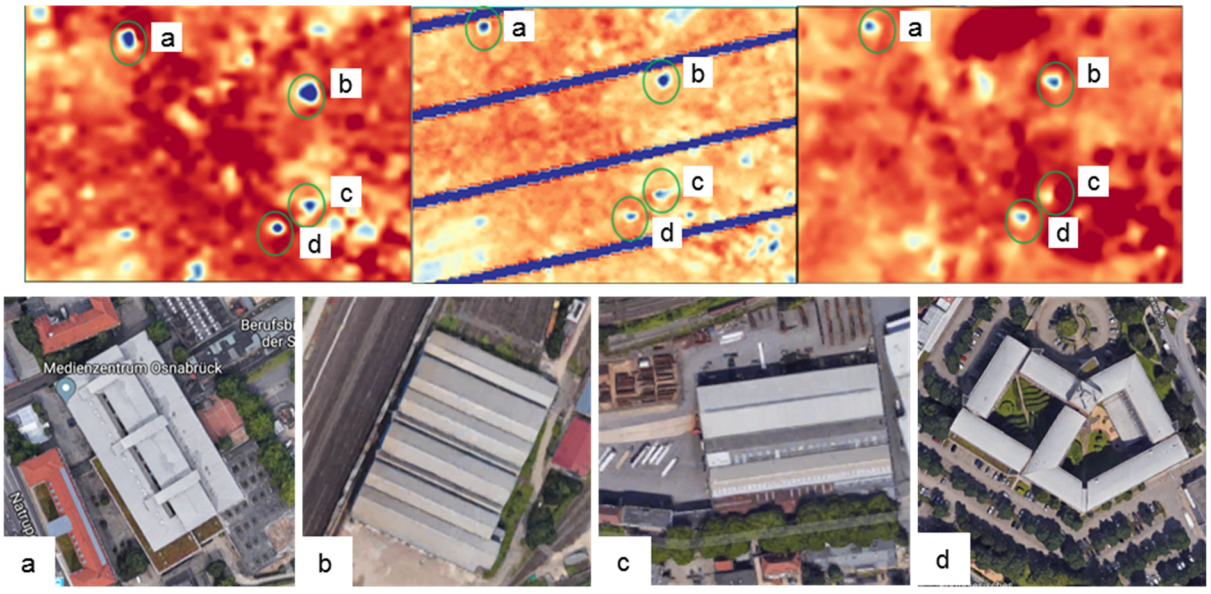

Figure 46 Four buildings with reflective roofs appear as cold spots in thermal images.

The normal solar reflectance material works in the same way in winter and summer. This is not suitable for low-latitude cities with cold weather in winter such as the city of Osnabrück since heat islands can be an asset in reducing heating loads. Therefore, some directionally reflective

roofs should be considered as a UHI mitigation strategy. In winter, they absorb sunlight with an absorptive side and in summer they reflect sunlight. This can be realized by the multifaceted surface, which changes its color and reflectance depending on the surface orientation (Akbari *et al.*, 2015).

The increase of green spaces also benefits the mitigation of urban high temperature. As mentioned in section 3.3.1, in the city center the park and wooded land appear as cool islands compared to the adjacent urban areas. Other UHI mitigation technologies include green roofs and shading of outdoor spaces (Akbari *et al.*, 2015) as well as creating air flow corridors (Baranka *et al.*, 2016).

To summarize, in this chapter the simplified Ehlers fusion was successfully used to improve the spatial resolution of open source thermal images. The experiment of filter settings that was presented in chapter 2 have been applied to Landsat 7, Landsat 8, and ASTER images. For daytime data, Landsat 8 panchromatic bands were used to sharpen the thermal band in the same band bundle. For nighttime data, Landsat 8 panchromatic images were used to sharpen Landsat 7 and ASTER thermal images. Compared to the experiment presented in chapter 2, this chapter shows that in application some practical issues need to be taken into consideration. Satellite images often face the challenge of atmospheric conditions such as clouds and snow. These atmospheric conditions make image fusion more complex when fusion is not between bands in a bundle, but from data of different sensors or different acquisition times.

Despite these difficulties, the simplified Ehlers fusion has successfully enriched the spatial details of satellite thermal images, as well as preserved the original thermal pattern. From the fused images, much more thermal distribution information could be gleaned compared to the original images. Based on the fused images, the main factors contributing to UHI impact on the city of Osnabrück during daytime and nighttime were identified. In the end, UHI mitigation strategies tailored for the study area are proposed, aiming at more efficient energy usage, more comfortable living, and an environmentally friendly urban development.

For UHI analysis, mainly remote sensing thermal images were used, only the building layer was additionally taken for further analysis of the thermal pattern in the built-up area. In the next chapter, another application case shows that using only remote sensing images could be insufficient for urban analysis. Therefore, a more complex fusion framework and more types of data are needed to be taken into consideration.

4. Data fusion application for urban vacant land extraction

The thermal images from chapter 3 show that in the northeast direction of the city of Osnabrück a group of buildings show a much lower temperature than the other built-up areas, both during day and night. On this site, barracks were built by the British army after the Second World War and abandoned after their withdrawal in 2006 (Stadt Osnabrück, 2019a). From then on, it has been a vacant site, with no heating system running in winter which contributes to the rather low temperature. The city of Osnabrück planned to reuse this site through a conversion project while the sale started in 2011. There are more similar vacant sites from former military barracks in the city. The low temperature in winter is only one sign indicating a site's vacancy. More data is needed to be fused together in order to automatically detect these vacant sites. In this chapter, the URBan land recycling Information services for Sustainable cities (URBIS) project is used to present how open geospatial data fusion can be applied in order to identify urban vacant sites. This project was completed in 2017 and reflects the current research status of vacant land extraction.

One of the main project tasks is to automatically detect vacant land. However, this task was not successfully completed. In subchapter 4.1, the main problems and the inaccurate project results were briefly introduced. To succeed in the identification of vacant land, the author of this thesis proposed a new definition of vacant land (subchapter 4.2) after reviewing the literature about vacant land. Afterward, the available data sources were investigated and selected (subchapter 4.3). Finally, the data fusion technique was applied to detect each type of vacant land (subchapter 4.4 and subchapter 4.5).

4.1. Confusing results caused by ineffective data fusion—reflection on the URBIS project

URBIS was an EU-funded research project aimed at building up an open source urban land use information system for vacant land. The project addressed a serious Europe-wide problem: on the one hand, increasingly more agricultural and natural areas have been converted into artificial surfaces; on the other hand, a number of built-up areas have been abandoned. URBIS proposed a sustainable urban development approach by recycling abandoned land and integrating fragmented land. Two main features are highlighted in this project: using various sources of open geospatial data and developing a site identification methodology applicable across Europe. Besides the city and county of Osnabrück, two more pilot areas were selected to represent European urban zones, namely Greater Amiens, France, and the Moravian-Silesian Region, Czech Republic. The main work content included developing best practices for vacant site inventory, automatic site detection, as well as building up the interoperable web services. In this chapter, automatic vacant site detection is emphasized from a data fusion perspective.

4.1.1. URBIS vacant land typology—unfavorable open data fusion conditions

Through a review of the recent EU projects which share the same topic, URBIS defined the following vacant land typology based on the outcomes of the Circular Flow Land Use Management project (Preuß and Verbücheln, 2013):

- *Greenfields with development perspective* have not been developed and connected to the city infrastructure but are located within the scope of the preparatory land use area. Typically, there is no sealing or building activity on site.
- *Vacant or underused land* was previously used and is now unused or used in a suboptimal way. The connection to the city infrastructure remains on site. Such sites are often covered by vegetation, but former activities are obvious, such as fragments of the sealed surface.
- *Gaps in built-up areas* are underused or unused areas that usually have a small size and are located within the existing urban fabric. They are suitable for construction due to the nearby infrastructure.
- *Brownfields* typically have construction on site and could have contamination problems. Previous types of use include for example industry, military, agriculture, or commerce. Due to these heterogeneous former land uses, the appearance and morphology of brownfields varies strongly.

The above classification is only feasible after the vacant sites have already been well-documented, together with their land use, size, contamination, and existing building information. However, in URBIS's case, it was the main objective to detect unknown urban vacant sites. Then the above typology challenges the identification of the vacant sites with a certain degree of automation. The main reasons are listed in the following.

- The classification approach was not built upon an explicit standard. For instance, the main feature of gaps in built-up areas is the rather small size, but other types of vacant land can also have a small size. This makes it impossible to follow a logic to separate them step by step.
- The contamination information is a crucial element that can be used to distinguish brownfields. It is possible to remotely detect oil-contaminated soil using hyperspectral data. However, the very limited free hyperspectral data makes it difficult to realize site detection based on open source data.
- The development perspective was involved in the definition. This produces an unfavorable condition for automatic site extraction because this perspective cannot be automatically detected.

In practice, it was proven that it is impossible to identify these sites according to the description of the typology, based only on one open data source. Therefore, the URBIS project team decided to take a broader scope to include all possible vacant land sites. However, that decision meant that besides brownfields, gaps, vacant land, and greenfields, also other green urban areas which are in use such as private gardens and public parks were incorporated. URBIS considers all of these sites as having the potential to be further developed and are therefore called potential development areas (PDAs). Additionally, URBIS provides PDAs with plentiful attributes such as the degree of sealing, the shortest path to highway, and vegetation coverage, for end-users to evaluate the use of the sites.

The URBIS project claimed to make use of open source data. During the implementation, various data sources, such as Copernicus Urban Atlas (UA), OSM, and social media data, were applied. UA was used to improve satellite land cover classification results; OSM was used to calculate transportation-related site attributes; social media data was used to create an additional

human activity map layer. These datasets were used separately for different purposes but not fused together. URBIS vacant land identification was done mainly by classification of satellite images, without the integration of these open data sources. However, using image classification alone cannot provide any information about land vacancy.

Through a deep investigation during the project, it was found that the problem was caused by the definition of vacant land. It could not provide a data fusion framework based on which the individual types of vacant land could be separated. The definition, specifically the vacant land typology, neither considered the properties of the available open data sources nor indicated an ineffective data fusion procedure to separate different types of vacant land step by step. The most unfavorable condition produced by this definition is that it mixed two data fusion levels (Pohl and van Genderen, 1998): the feature level for site detection and the decision level for the development perspective. In fact, vacant land identification should firstly be accomplished on the feature level and afterward, with additional criteria a few decision rules can be applied to determine the development potential.

Due to the above reasons, even though the project produced valuable results, such as sufficient maps and an interactive online tool for end-users, inaccuracy appears on some of the produced maps, which are demonstrated in the following section.

4.1.2. Inaccurate project results caused by ineffective data fusion

UA features were integrated into a SPOT-5 image land cover classification, to directly retrieve all the types of PDAs based on vegetation coverage and sealing degree. The major problems of the detection results are summarized as follows.

- *Greenfield with development perspective* was replaced by *urban green area* including any vegetated areas within the city such as street trees (see Figure 47, colored in green). This is not aligned with the original intention of site detection because these sites are not vacant and cannot be further developed.
- *Vacant land* was mostly mistaken for sports areas (see Figure 47, colored in brown).
- *Gaps in built-up areas* were very often confused with private gardens that are attached to the neighborhood (see Figure 47, colored in yellow).
- *Brownfields* were not automatically detected as originally planned but taken from the local government database.

Although the commercial satellite image SPOT-5 used has a high spatial resolution of 5 m, it produced incorrect classification results. The confusion of site identification and evaluation of land recycling property were the main reasons for imprecise project results. Vacant land re-development was one of the most important project goals, but it involved redefining vacant land (typology), data processing (classification), and site potential assessment. On the conceptual level, vacant land is the object and land recycling is the objective. Therefore, the definition of the vacant land typology needs a revision. The revised typology should take the available open source data and their properties into account, and be rooted in a clear data fusion framework so that each type of vacant land can be extracted separately.

Figure 47 Part of vacant land identification results from the URBIS project compared with Google Maps. PDA: potential development area.

4.2. Revised vacant land typology towards open geospatial data fusion

This subchapter first reviews the vacant land related definitions, among which one vacant land typology is taken as a base so that a new vacant land typology can be proposed. The advantages and reasons for using this typology are also provided.

4.2.1. Current research state of vacant land

The term "vacant land" is broad and diverse; every country, or even city, defines it according to their own land use situations. The land for development in the city of Philadelphia, PA, USA is also rare and expensive. Thus, the city ran a project to map garden use, as vacant lots could contain many gardens and farms going back generations which are no longer legally valid (Crowe and Foley, 2017). The Czech Republic had its transition from planned to market economy in the 1990s, which resulted in a rising number of abandoned industrial and agricultural complexes, production facilities, and warehouses. The country then built up a national brownfield database to register all these vacant sites (CzechInvest, 2018). As seen from the above examples, vacant land is usually associated with features such as derelict land, brownfields, abandoned buildings and structures, and greenfields. In practice, brownfields are very often confused with vacant land. By the definition of the United States Environmental Protection Agency (EPA), a brownfield is a property, the expansion, redevelopment, or reuse of which may be complicated by the presence or potential presence of a hazardous substance, pollutant, or contaminant (EPA, n.d.). In European countries, brownfield refers to any land or premises which has previously been used or developed and is not currently fully in use, although it may be partially occupied or utilized. It may also be vacant, derelict, or contaminated (Alker *et al.*, 2000). In summary, a brownfield describes the land or premises that has previously been used and is currently underused. Reusing brownfields may be complicated by the demolition of existing structures or the necessary treatment of contaminations.

Vacant land contains some green and open spaces (GOS) within the urban area such as "urban green areas" and "open spaces with little or no vegetation" classes from UA. This leads to a mix-up between vacant land and GOS, as it was done in the URBIS project. It started with vacant land identification but resulted in a "green and open space layer". This is necessary to make a clear distinction between vacant land and GOS to avoid excessively broad and imprecise

site extraction. The relationship between brownfields, vacant land, and GOS is shown in Figure 48. The "green and open spaces within an urban area" overlap between vacant land and GOS. In non-urban areas, there are more and larger GOS such as farming land and forests which are not vacant. On the other hand, vacant land also contains some features that do not belong to GOS, such as an industrial brownfield without vegetation coverage.

From a conceptual perspective, GOS and vacant land target different objectives. GOS focuses on the problem of urban sprawl. As a city spreads into its surrounding landscapes, it takes resources from the natural environment, such as conversion of agricultural land and urban green areas into built-up areas. Therefore, increasing imperviousness and decreasing GOS must be documented (Rashed and Jürgens, 2010). Thus, GOS includes all vegetated areas in both urban and non-urban areas. In contrast, vacant land addresses urban land use recycling and optimization. Brownfields are part of vacant land and they are a waste of land resources that could be recycled. Vacant land also takes into account the free spaces within the low-density built-up area; if urban land needs to be increased, these low-density areas could be further developed into a built-up area instead of taking land from outside the urban area. Even on the conceptual level, vacant land and GOS still partially overlap, as there is a strong relationship between land use recycling and urban sprawl. The more brownfields can be recycled, the more land resources will be available for urban land use.

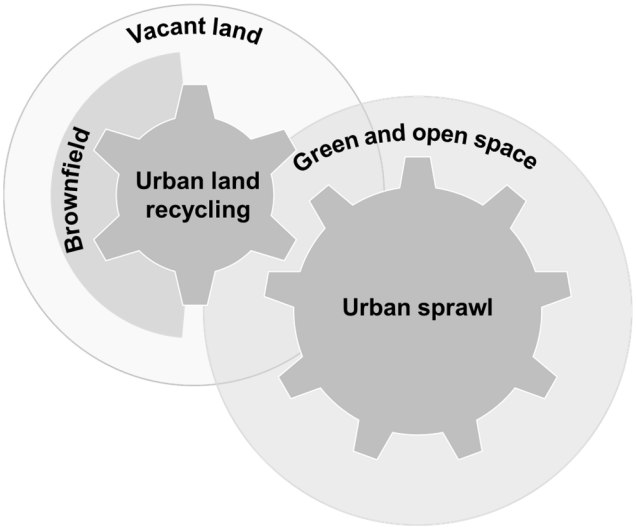

Figure 48 The overlap between brownfields, vacant land, and green and open spaces.

4.2.2. Proposed vacant land typology

Kim *et al.* (2018) define a comprehensive typology of vacant land which includes five categories: *post-industrial sites*, *derelict sites*, *unattended with vegetation sites*, *natural sites*, and *transportation-related sites*. From all five categories, *post-industrial sites* and *derelict sites* belong to the scope of brownfields but cover only part of them. *Transportation-related sites* are straightforward: they are the vegetated areas adjacent to the road infrastructure. The original definition of *unattended with vegetation sites* and *natural sites* are very similar in the sense that they can be further developed for enhancing the ecological and social benefits. This thesis further considers the arguments from Northam (1971) who points out that some vacant land are corporate reserved parcels for future expansion, transitional land for speculation, and land in institutional reserve for future development. These kinds of land can be integrated into

unattended with vegetation sites. This category should also include the gaps in dense built-up areas which are the leftover areas within the urban fabric. Along these lines, *unattended with vegetation sites* are revised as *unattended areas or remnant parcels*. Sites in this category are suitable for developing into built-up areas, as they are land without current use but already marked for use. In contrast, the *natural sites* are suitable for strengthening the ecosystem and use as an environmental protection zone. In this way, it enlarged the differences between *unattended areas or remnant parcels* and *natural sites*, which is beneficial for an effective site extraction.

In the phase of defining vacant land, the available data sources and their properties for site identification were also taken into account. The UA produced from the EU Copernicus Land Monitoring Service is freely accessible, reliable, and provides high-resolution land use maps for urban areas and their surroundings. The land use classification results have been validated as having high accuracy and quality (Gallaun *et al.*, 2017). Most importantly, UA contains several classes directly or indirectly related to vacant land.

Figure 49 provides an overview of the UA classes related to vacant land. UA classes *fast transit roads and associated land*, *other roads and associated land*, and *railways and associated land* include the railways, roads, and connected greenfields. The greenfields are the vacant parcels that need to be extracted. UA classes *herbaceous vegetation associations*, *open spaces with little or no vegetation*, *wetland*, and *forest* fit into the natural sites category. Certainly, not all of these natural areas are vacant land, only those located within dense built-up areas are focused on. Therefore, further selection is necessary to exclude the non-vacant part. *Land without current use* can be directly taken as vacant land. It is very often a small piece of forest or grass appearing within *sport and leisure* facilities. These grass surfaces and forests have no clear ownership and thus could be vacant land. *Green urban areas* are mainly places such as public parks, orchards, and allotments. But it also includes some attended vacant parcels without any usage which belong to vacant land. Brownfields are the most difficult category in terms of detection using UA classes. As only *mineral extraction and dump sites* fall into this category, detection of brownfields on other conditions need additional sources.

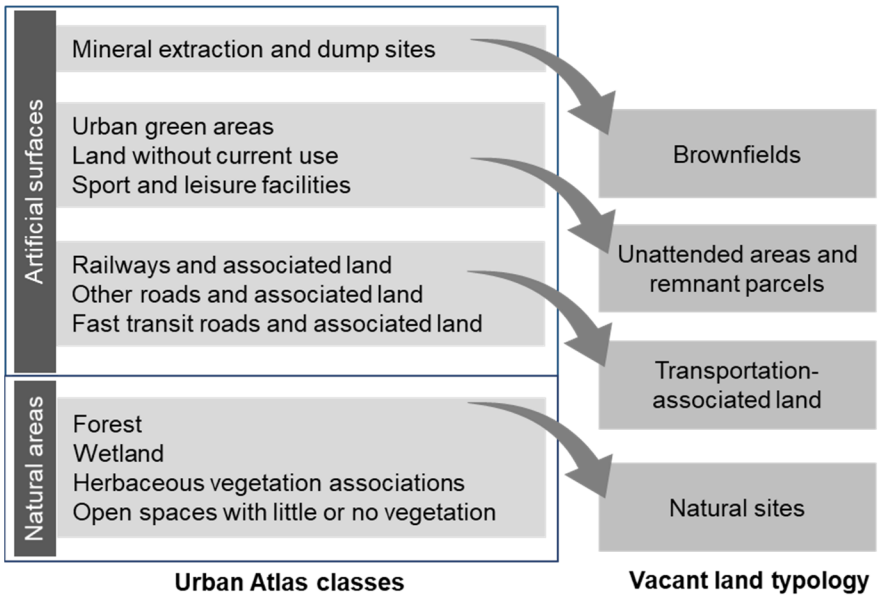

Figure 49 The relationship between Urban Atlas classes and vacant land categories.

Based on the above revised vacant land categories, together with the UA classes, the following vacant land typology is proposed.

- *Transportation-associated land*: land and spaces that are related to transportation systems including railways, highways, and other roads.
- *Natural sites*: these sites are located within built-up areas, yet have not been used due to their physical constrains by environmental conditions such as drainage areas, wetlands, hillsides, steep slope, river bands, and river floodplains.
- *Unattended areas or remnant parcels:* these sites are empty and inactive, look like gaps within a built-up area, or leftover spaces within the urban fabric. They very often appear as unimproved woods and unimproved vacant parcels but not parks or gardens. Part of these sites are already reserved for future expansion and future development.
- *Brownfields:* the land or premises has previously been used and is currently underused. Reusing such a brownfield may be complicated by treatment of existing structures or contaminations. Typically, there are derelict buildings or structures onsite and the previous land use include for example industry, military, agriculture, or commerce.

The biggest advantage of this typology is that the categories match with the vacant land related UA classes, thus benefiting vacant site identification using UA. This typology also follows the basic classification structure of UA which divides the land into artificial surfaces and natural areas. The defined vacant land typology puts *natural sites* into the natural area and all the other categories into the artificial surface.

According to the above-described relationship between vacant land and GOS, the *transportation-associated land*, *natural sites*, as well as *unattended areas and remnant parcels* belong to both vacant land and GOS. Brownfields certainly do not overlap with GOS. It only belongs to vacant land.

4.2.3. The data fusion framework indicated by the vacant land typology

Although the definition of vacant land strongly indicates utilization of UA data, UA only provides a starting point; and additional data need to be integrated to complete vacant site selection. The definition of the vacant land typology implies two levels of data fusion processes (Figure 50).

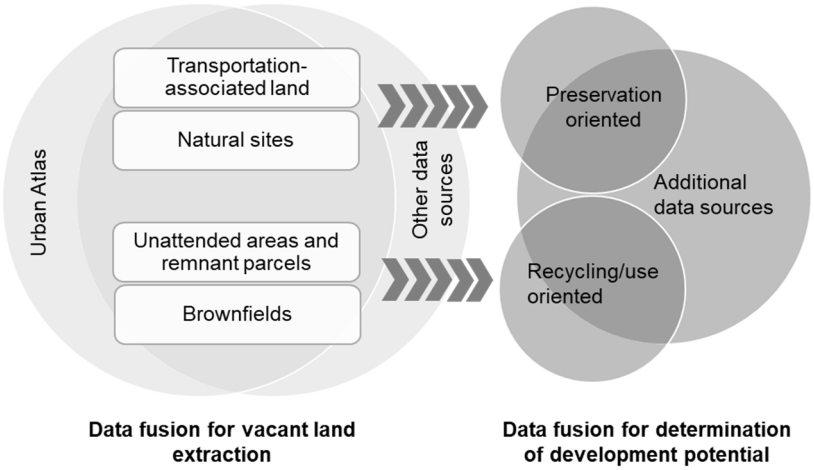

Figure 50 The data fusion framework indicated by the vacant land typology.

Firstly, vacant land related UA classes are vector features. Further extraction of vacant sites will select or clip these features depending on the information from the other data sources. The extracted sites will also be recorded as vector features. Thus, the fusion takes place at the feature level.

Secondly, the typology describes the reasons causing vacancy which serves as a primary orientation of land development potential. *Transportation-associated land* is limited by the odd-shape and unfit location. *Natural sites* probably include steep slopes, drainage areas, hillsides, riverbanks, river flooding zones, wetlands, as well as environmentally protected zones. These two types of vacant land are not suitable to be developed. Instead, they should be preserved to enhance the ecological system and environmental protection. The vacancy of *brownfields* and *unattended areas and remnant parcels* is human-related: for *brownfields*, it is due to the high cost of the treatment of contamination, demolition of existing buildings, or land leveling; for *unattended areas and remnant parcels*, it is due to unintended retention or reservation for future use. These two types of vacant land are awaiting utilization, and therefore have priority for further development including recycling and reuse. However, this is just a first orientation of land use implied by the definition. The final decision on the land use of all the vacant sites depends on additional criteria, such as the connection to transportation and energy infrastructure. To calculate these criteria, additional data sources need to be integrated together, leading to a fusion on the decision level.

The two levels of data fusion can only be implemented one after the other. The data fusion on the feature level needs to be done first so that the location of vacant site is already identified. Then, the land development of each site can be decided based on the data fusion on the decision level.

Since the definition takes UA classes into account, the site extraction has a dependence on UA data. This dependence varies according to the type of the vacant land. The lower the dependence on UA, the more additional data need to be integrated. For the *transportation-associated land* category, all possible sites are included in UA transportation-related classes; thus, the site extraction depends on UA data. The *natural sites* as well as *unattended areas and remnant parcels* are mixed with used land in UA classes. Therefore, site identification of this type of vacant land partly depends on UA data, and partly depends on additional land use information which can be useful for the separation of used and unused land. For brownfields, UA classes cover only a few parts so that the additional data sources are more important than UA data for site identification.

The typology indicates that each type of vacant land needs an individual data fusion procedure. More precisely speaking, individual site selection rules are applied in the data fusion process. Rule-based or knowledge-based approaches have been widely used in data fusion procedures (Ban *et al.*, 2010; Lucas *et al.*, 2007; Zhang and Wang, 2003), mainly for image classification purposes. These methods are applied here for vacant land extraction. Due to the different input data, the rules for site identification vary according to the type of the vacant land. The detailed data fusion procedure is demonstrated in subchapter 4.4.

4.3. Available open geospatial data for vacant land extraction

UA is the most important dataset but only UA is insufficient to extract all types of vacant land. This subchapter firstly illustrates how UA classes can be directly or indirectly used for vacant land extraction. Then, other ancillary data and their role in vacant land extraction are also introduced.

4.3.1. The role Urban Atlas plays in vacant land extraction

UA provides Europe-wide land use and land cover maps, which can be viewed and downloaded through the services supported by the European Copernicus program. For the reference year 2006, UA 2006 covers 305 functional urban areas, including cities with more than 100,000 inhabitants. Later, UA 2012 was extended to nearly 700 larger cities.

The UA is mainly based on the combination of (statistical) image classification and visual interpretation of very high-resolution satellite imagery. The input data are multispectral SPOT-5, SPOT-6, and Formosat-2 pan-sharpened images with a 2 m to 2.5 m spatial resolution (European Commission, 2016). The final product is vector data in Esri shapefile format with minimum mapping unit 0.25 ha in urban areas and 1 ha in rural areas. Focusing on urban areas, UA 2006 contains 21 classes of which just four classes represent the agricultural and natural classes. UA 2012 extended this to 27 classes with more detailed classification in rural areas.

4.3.1.1. Urban atlas classes that can be directly taken as vacant land

Land without current use: "Areas in the vicinity of artificial surfaces still waiting to be used or re-used. The area is obviously in a transitional position, 'waiting to be used'. Waste land, removed former industry areas ('brown fields'), gaps in between new construction areas or leftover land in the urban context ('green fields'). No actual agricultural or recreational use. No construction is visible, without maintenance, but no undisturbed fully natural or semi-natural vegetation (secondary ruderal vegetation). Also areas where the street network is already finished, but actual erection of buildings is still not visible." (European Commission, 2016, p. 21)

The description of this class indicates that all the sites included in these classes are certainly vacant land. According to the defined typology, this class contains more than one type of vacant land: "waiting to be used" and "gaps or leftover land" fits to the class *unattended areas and remnant parcels*; "waste land" and "removed former industry" belong to the class *brownfields.* Through ground truth check of this class in the study area, it was found that these features mainly refer to the class *unattended areas and remnant parcels*, only few involve *brownfields*. Thus all of them are directly taken into the class *unattended areas and remnant parcels.*

Open spaces with little or no vegetation: This class includes "a) beaches, dunes, sand:< 10% vegetation cover; beaches, dunes and sand plains, (coastal or inland location), gravel along rivers; seasonal rivers, if water is characteristic for a shorter part of the year (< 2 months). b) Bare rocks :> 90% of the land surface of bare rocks, (i.e. < 10% vegetation); rocks, gravel fields, landslides; scree (fragments resulting from mechanical and chemical erosion. Weathering rocks forming heaps of coarse debris at the foot of steep slopes), cliffs, rocks. c) Sparsely vegetated areas: steppes, tundra, badlands, scattered high altitude vegetation. Bare soils inside military

training areas. Vegetation cover 10 - 50%. d) Burnt areas: Recently burnt forest or shrubs (but not natural grassland), still mainly black on EO data. e) Snow and ice: glacier and perpetual snow." (European Commission, 2016, p. 24).

The description of this class presents various environmental conditions that keep the sites under constraints from development, such as gravel along rivers, landslides, and glaciers. Only one exception is the bare soil inside military training area, which does not fit to the definition of vacant land. However, this kind of sites do not commonly appear. Considering most of the cases, the features from this class can be grouped into the *natural sites* whose vacancy is caused by unfit physical conditions.

4.3.1.2. Urban Atlas classes containing vacant land

Green urban areas: "Public green areas for predominantly recreational use such as gardens, zoos, parks, castle parks and cemeteries. Suburban natural areas that have become and are managed as urban parks. Forests or green areas extending from the surroundings into urban areas are mapped as green urban areas when at least two sides are bordered by urban areas and structures, and traces of recreational use are visible." (European Commission, 2016, p. 21)

As the definition indicates, greenest urban areas serve as recreational ground. However, by ground truth check it was discovered that this class also includes some vegetated areas without obvious traces of any usage on site. These green patches are leftover land that should be focused on.

Sport and leisure facilities: "All sports and leisure facilities including associated land, whether public or commercially managed: e.g. Theresienwiese (Munich), public arenas for any kind of sports including associated green areas, parking places, etc.: golf courses; sports fields (also outside the settlement area); camp grounds; leisure parks; riding grounds; racecourses; amusement parks; swimming resorts etc.; holiday villages ('Club Med'); allotment gardens; glider or sports airports, aerodromes without sealed runway; marinas." (European Commission, 2016, p. 22)

Most of the sites from this class have a certain function, except that some large recreational ground such as an allotment area partially contains underused/unimproved woods. In the future, these patches of woods could be developed for the same or other purposes. At the current moment, they have not been used. To precisely measure all possible vacant land sites, these kinds of patches also need to be taken into consideration.

Fast transit roads and associated land, other roads and associated land and railways and associated land. As the name indicates, these classes not only include the road surface or railways, but also the areas surrounded by highway or railway junctions. The enclosed areas are mostly greenfields and cannot be used for any purpose.

Herbaceous vegetation association, forest and wetland classes are mostly large in scale and under supervision and are thus not vacant. Only some small patches extend into dense built-up areas, bordered by urban structures. In other words, these pieces are leftover areas from urbanization or landscape fragmentation from urban sprawl. They are probably no longer under regular supervision and thus can be considered as vacant land in the category of *natural sites*.

4.3.2. The role of other ancillary data in vacant land extraction

Imperviousness is a series of soil sealing maps which is also provided by the Copernicus Land Monitoring Service. It "captures the spatial distribution of artificially sealed areas, including the level of sealing of the soil per area unit" (Copernicus Programme, 2019a). The sealing level, which is also referred to as imperviousness degree 1% to 100%, is produced by semi-automated classification based on calibrated NDVI. The imperviousness data consists of two products: status layers for any of the 4 reference years 2006, 2009, 2012, and 2015, and change layers for each of the 3-year periods between the four reference years, as well as for the period 2006 to 2012. The products are raster layers with 20 m spatial resolution and an aggregated resolution of 100 m. Imperviousness is taken into consideration because it can be used to separate vacant green patches from used land which is indicated by the sealed surfaces. Moreover, imperviousness layers of different years can be used to identify abandoned areas, because a reduced degree of sealing probably indicates lack of routine maintenance.

CORINE Land Cover (CLC) data is also provided by the Copernicus Land Monitoring Service. It is a pan-European land cover map, initiated in the reference year 1990 and updated in 2000, 2006, 2012, and 2018. It has a minimum mapping unit of 25 ha. CLC is produced by most countries using visual interpretation of high-resolution satellite imagery. In a few countries, semi-automatic solutions are applied, using national *in situ* data, satellite images, and GIS information. (Copernicus Programme, 2019b)

OSM is a project aimed at building a free geographic database of the world. For this purpose, it created and distributed a dedicated, freely editable map of the world. Any registered contributor can edit the data, for example based on manual survey and fieldwork with global positioning system, usually referred to as GPS, devices (Bennet, 2010). OSM data provision is under the Open Database License and access is thus free of charge. The data is stored in a PostgreSQL/PostGIS database where spatial objects are represented as vector-based geometric features. OSM mapping elements consist of *nodes* which are geographic positions stored as coordinates in the World Geodetic System, usually referred to as WGS, number 84 reference, *ways* that may be interpreted either as a polyline or a polygon, and *relations* to build up the relationship between nodes and ways. A *tag* is used to describe the specific features of map elements and consists of two items, a *key* and a *value*. For vacant land detection, tags can be used as a searching tool. For example, setting "landuse" as the key, the values list for this key contains terms such as "brownfield", "proposed", "abandoned", "disused", "abandoned:farmyard", "vacant", and "reserve" (OSM, n.d.). If taking railway as the key, the possible values consist of terms such as "abandoned" and "disused". These tags indicate possible vacant land including brownfields and are therefore of interest. The complete OSM dataset covers the whole planet and is available in different file formats. Users can import a subset of OSM data into their own database or download the preprocessed subset data in the Esri shapefile format from the Geofabrik website (http://download.geofabrik.de/).

Wikidata is a free knowledge base driven by a community and initiated by the Wikimedia Foundation, as well as providing a repository for linked, open data, it aims to support Wikipedia and its sibling projects by providing a centralized database. In OpenStreetMap Wikidata entities can be linked on every kind of OSM object using the wikidata key. With wikidata tag, data can

be easily checked with the Wikidata+OSM SPARQL query services (www.wikidata.org/wiki/Wikidata:SPARQL_query_service/queries).

Figure 51 shows an example of using Wikidata and OSM SPARQL query services to search "abandoned village" in the Czech Republic. More than 1,000 sites were found and are presented in OSM. The coordinates of each abandoned site can be read from the results table.

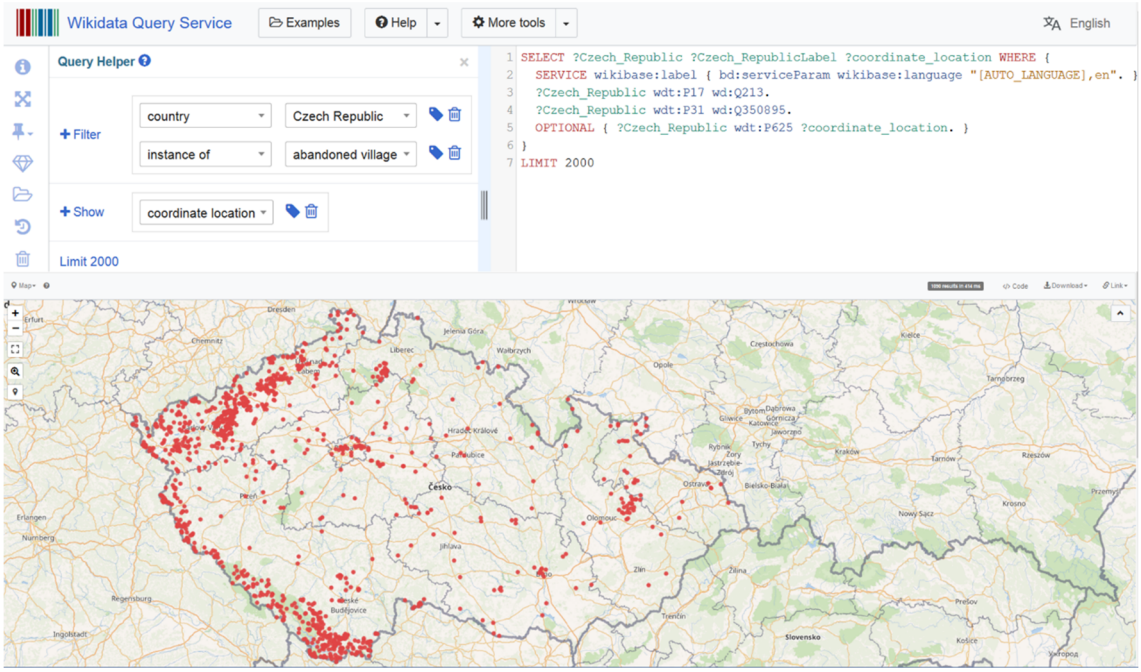

Figure 51 An example showing vacant land search results from Wikidata (https://query.wikidata.org/).

Social media data is created by social media such as Facebook, Twitter, Instagram, or Flickr. It consists of user-generated content such as text messages, photos, or videos, which in general are referred to as posts. Some of the posts are tagged with a location, and through analyzing the spatial distributions of these geotagged posts, the appearance of human activity can be discovered. Several social media applications provide a data anonymization service in order to remove personally identifiable information. However, the metadata contains spatial references that can be collected through a publicly accessible application programming interface (API). It is assumed that on the brownfields or abandoned sites, buildings or houses remain empty or unused, and very low human activity will appear. Therefore, posts from social media will seldom be generated on these sites. The number of posts can be used as an indicator of the state of site usage.

4.4. Data fusion procedures for vacant land extraction

As already mentioned in subchapter 4.3, from *transportation-associated land*, *natural sites*, *unattended areas and remnant parcels* to *brownfield*, the dependence on UA is gradually reduced, and this means that the difficulty of site extraction increases. In the following, site extraction follows an easy-to-difficult order and starts with *transportation-associated land*.

4.4.1. Extraction of transportation-associated land

The features from UA transportation-related classes contain both the roadways and the land nearby. Extraction of the land is equal to excluding the roadways and railways. It is an

innovative way to use a circle inside each feature to exclude these long and narrow features representing paved roadways. For each polygon, the centroid is first calculated. The center of the circle is located at the centroid of the polygon, and the radius of the circle is the minimum distance from the polygon centroid to the border of the polygon. The widths of the streets are assumed to be mostly less than 20 m. Therefore, for polygons that can contain an inner circle with a radius of more than 20 m, it contains the associated land and needs to be selected. The next step is to check whether the associated land has already been used or is in vacant status. This is done by investigating the sealing conditions using the imperviousness layer. For each polygon, the average degree of sealing is calculated. Then, from the last selected polygons, those with an average degree of sealing less than 50% are further selected. This means that the final selected polygons contain at least half of its area that is unsealed. From the finally selected polygons, the vegetation patches which have an imperviousness value of zero were clipped. The complete workflow of the site selection is illustrated in Figure 52.

In this data fusion workflow, three parts are marked as grey color. These are the rules to determine site selection. The first rule was used to exclude the rails or paved roadways, the second rule was set to recognize the site that possibly contains vacant land and the last rule was used to extract the vacant patch. The data fusion behind this site selection process is between UA vector data and imperviousness raster data. These two datasets play different roles during the data processing procedure: UA data is taken as the starting point. Then, through the complete site selection workflow. The raster layer is integrated into the workflow in the in the second step. Finally, the results are derived from both data sets.

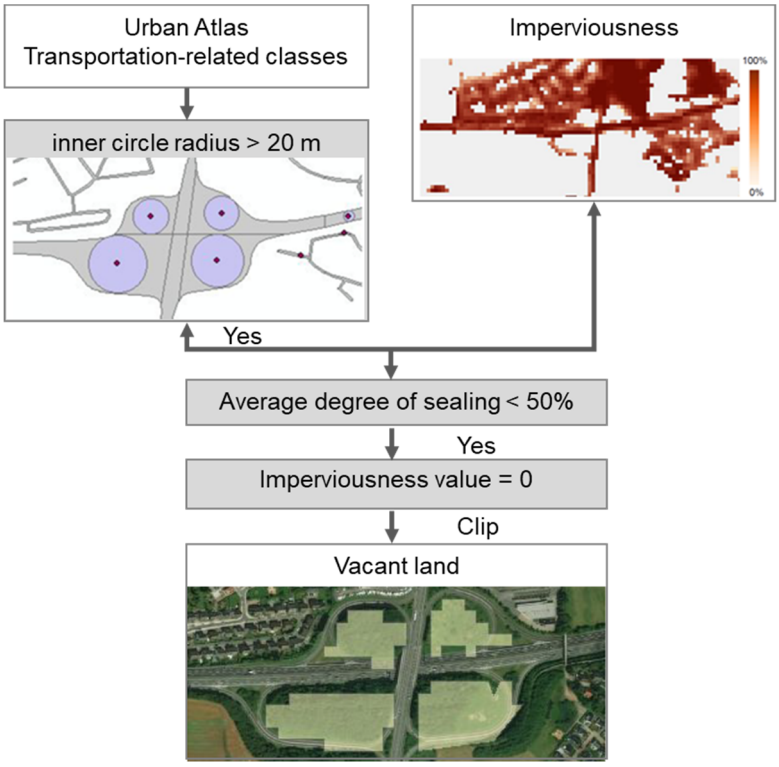

Figure 52 The data fusion procedure to extract transportation-associated vacant land**.**

4.4.2. Extraction of natural sites

The UA classes standing for natural areas including *Forest*, *Herbaceous vegetation associations*, *Open spaces with little or no vegetation*, and *Wetlands* are firstly combined to

form a natural area layer. In this layer, those in the non-built-up areas are mostly under supervision or protection and cannot be identified as urban vacant land. Therefore, in the next step, a mask of built-up areas needs to be created. This mask of built-up areas is different from the administrative boundary of the city. The administrative urban area consists of not only built-up areas but also non-built-up areas. The mask of built-up areas is created using CLC data and named urban fabric envelope.

CLC consists of 44 land cover classes, from which the classes representing artificial surfaces are selected, including *airports*, *construction sites*, *continuous urban fabric*, *discontinuous urban fabric*, *dump sites*, *green urban areas*, *sport and facilities*, *road and rail networks and associated land, industrial or commercial units*. Then, these features are merged into one layer, and the convex hull of these features forms the urban fabric envelope. The envelope encloses the built-up areas, but not the natural areas represented by other CLC classes such as *mixed forest*, *broad-leaved forest*, and *natural grassland.* The CLC uses a minimum mapping unit of 25 ha, which means it ignores differences under this size. In contrast, UA has a minimum mapping unit of 0.25 ha. A natural area with size between 0.25 ha and 25 ha will be recorded by UA, but not by CLC. Additionally, if this natural area appears within the urban envelope, it is of interest, because it is a small patch of natural area but appears within the dense built-up area which could be a vacant natural site. The site selection workflow is illustrated in Figure 53.

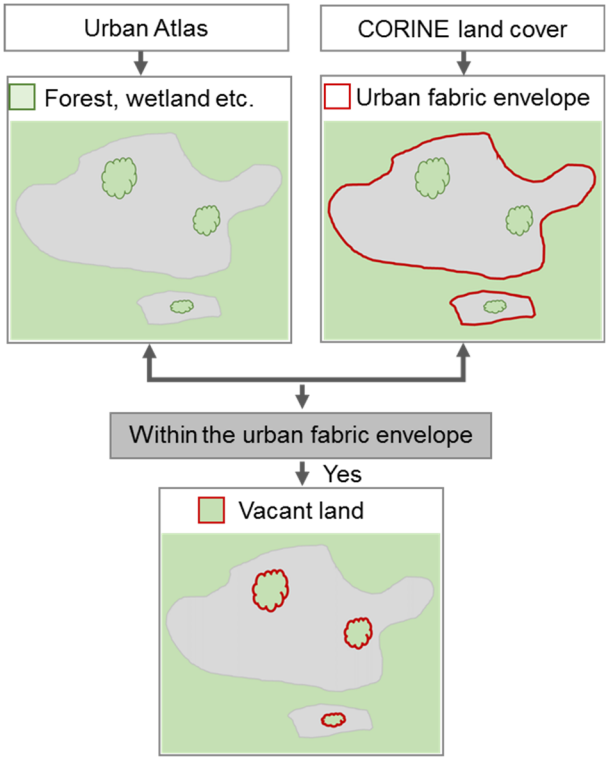

Figure 53 The data fusion procedure to extract vacant natural sites.

The challenge of extracting this type of vacant land is in distinguishing the natural area in the built-up area from the non-built-up area. After the urban fabric envelope is completed, the extraction of the *natural site* is rather straightforward. Only one selection rule is applied: those natural areas outside of the urban fabric envelope are disregarded and those within the urban fabric envelopes are classified as vacant land. The data fusion in the background of the site selection is between UA and CLC. Here, CLC plays a slightly more crucial role than UA,

because the data fusion rule is built up upon CLC. CLC precision will directly decide the quality of the output results.

4.4.3. Extraction of unattended areas and remnant parcels

For this type of vacant land, UA classes *green urban area*, *sport and leisure facilities*, and *land without current use* are focused on. These classes contain partly used land and partly vacant land. The main goal of the site selection is to exclude the used part. Therefore, OSM land use information is applied. The data processing contains three parts:

- Selection of the UA class *green urban areas* and at the same time, selection of OSM land use classes: *park*, *allotments*, *cemetery*, *farm*, *orchard*, *park*, *recreation ground*, *vineyard*. If the features from *green urban areas* contain the selected features in OSM, they are filtered out. The remaining features are green patches without certain usage.
- Selection of the UA class *sport and leisure facilities*, and at the same time select OSM land use class *forest*. If a sport and leisure facilities feature contains forest feature from OSM, then clipping is applied. The cut-off areas are sport ground related land without usage. Here, only forest is taken into the selection while the other vegetated type *meadow* is not included, because sport areas often contain places vegetated by grass which looks similar to a meadow, like football fields. These places are used land and do not belong to vacant land.
- All UA *land without current use* features.

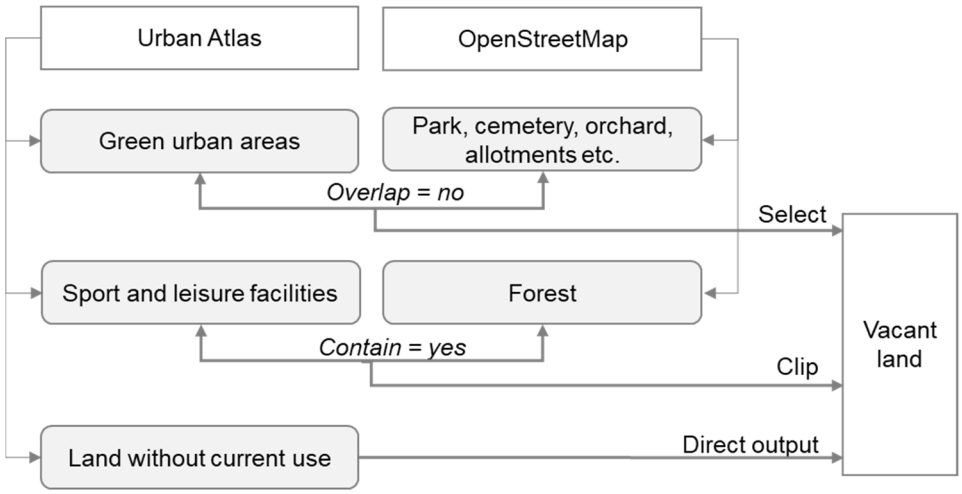

Figure 54 The data fusion workflow to extract unattended areas and remnant parcels.

Figure 54 illustrates the overall site selection process, which is also a rule-based data fusion procedure. The data fusion is between UA vector features and OSM land use information. The rule setting is based on whether UA and OSM features are overlapping. In this fusion procedure, UA and OSM are used in parallel. Both of the datasets work as the main data sources and are of equal importance.

4.4.4. Extraction of brownfields

In the four types of vacant land, brownfields are the most challenging ones in terms of automatic site detection. UA contains only one class *mineral extraction and dump sites* which could include brownfield sites. Thus, it cannot be used as the main data source. It is also difficult to use other remote sensing data for direct site identification, because brownfields have a varied

morphology, and the surface could be vegetated or completely sealed. Even if contamination is one distinct character, it does not necessarily appear on all brownfields. Other than this, no specific factors can be used for site extraction. There is no difference between normal buildings and derelict buildings from the view of the remote optical sensor. Therefore, additional open data sources must be included.

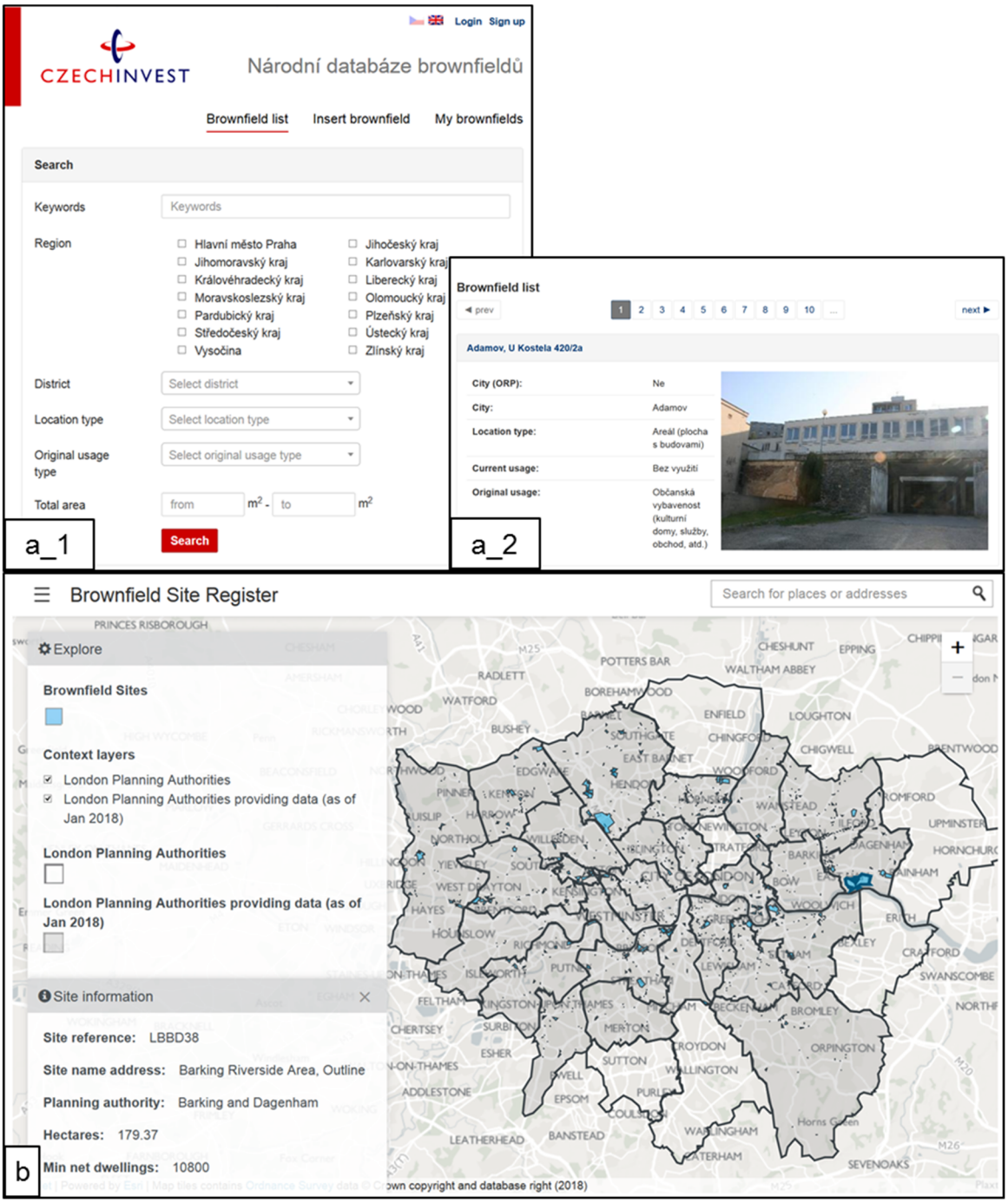

Figure 55 Screenshots of two open brownfield databases from governments: (a) brownfield published by an agency from the Czech Republic; (b) brownfield published by the London Planning Authorities.

For a country that faces serious brownfield issues, such as the Czech Republic, there is often a nation-wide brownfield database open to the public. The Ministry of the Economy of the Czechoslovak Republic established the Investment and Business Development Agency, CzechInvest, on October 1, 1990 (CzechInvest, n.d.). This agency published a national brownfields database online (www.brownfieldy.eu). It provides an overview of the number,

characteristics, and development status of brownfields in the whole country. Detailed information about the brownfields are published such as location, original usage, current usage, and pictures (see Figure 55a). The UK has taken similar action concerning brownfields. In 2017, the Ministry of Housing, Communities & Local Government of the UK started the Brownfield Land Registers Action, aimed at providing up-to-date and consistent information about brownfields. The local planning authorities are required to prepare, maintain, and publish information about brownfields covering their area. They should also provide transparent information about sites that are available and suitable for residential development (UK Government, 2017). Figure 55b shows the brownfield published on the register by London's city planning authority (Greater London Authority, 2019), where brownfield sites are marked with polygons, and the detailed information such as location, size, and ownership status are described.

In some countries, brownfield databases are only available for certain cities or states. This is the case for Bavaria and the city of Leipzig in Germany. The Bavarian State Office for the Environment provides a site management database including brownfields (Bayerisches Landesamt für Umwelt, 2018). In the city of Leipzig, the office for Urban Renewal and Housing Development also published a list of brownfields (Bürger für Leipzig Stiftung, n.d.).

Certainly, there are some cities where brownfields exist, but no related databases are open to the public. In this case, the OSM database and Wikidata queries can be taken into consideration. In the OSM database, the focus should be on objects which are tagged with words indicating a brownfield, such as *abandoned*, *disused*, and *demolished*. The same principle also works for Wikidata queries, where labels such as *abandoned village*, *former train station*, and *former building or structure* should be tested during the search. Wikidata offers a user manual which provides assistance to people using this query, and the results can be presented in table form or on a map (www.mediawiki.org/wiki/Wikidata_Query_Service/User_Manual).

The searched brownfield sites from OSM or Wikidata are crowdsourced, and it is thus necessary to further validate the reliability of the information. Building temperature in winter time can be used as an indicator of derelict sites, as low temperature implies no usage of a heating system. The data process to retrieve building temperature is already illustrated in chapter 3. Moreover, considering that an abandoned site will lack maintenance, the degree of sealing should be reduced over time. Therefore, imperviousness status can be investigated. The imperviousness change layers from 2006 to 2009, 2009 to 2012, 2012 to 2015, and 2006 to 2012 are of special interest. These layers contain already processed data that can be directly taken into use.

Social media data can also be useful. The basic idea of using social media data is that on brownfields or abandoned sites, very few human activities appear. Therefore, very few posts on social media at these sites will be generated. However, not all social media platforms provide a service that allows posts to be searched through a publicly accessible API, or even be searched by coordinates or area of interest. For example, Facebook as one of the most popular social media applications does not offer an API function for spatial search. In contrast, Twitter, Instagram, and Flickr offer access to their data using spatial-related search queries. Therefore, the user can define a bounding box and collect the posts within.

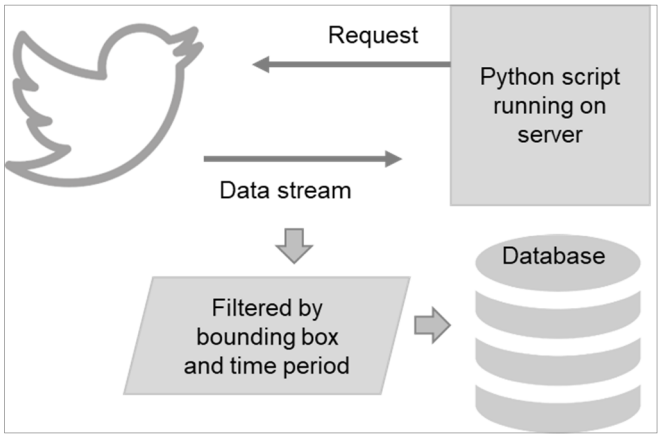

Figure 56 Retrieval of a human activity map using Twitter (adapted from URBIS deliverable 3.3, not published)

For most social media platforms, users can only collect real-time posts through public access. For reflecting human activity, the posts within an accumulated time are more relevant. Therefore, the request for searching public posts must be regularly sent to the server and the retrieved data need to be stored into a database. After a period, the number of collected posts reflects the level of human activity, as more posts indicates more frequent activity. Taking Twitter as an example, Figure 56 shows the data processing workflow. Firstly, a bounding box and a time period are set up. Then, Python scripts start to run on a server, triggering Twitter API functions to search posts within the bounding box, and the filtered data is received through a data stream. Within a set time period, this will run iteratively. The retrieved posts are recorded in point geometry format together with the metadata of the posts. Afterward, the received data are imported into a database and can be further processed into an activity density (posts per unit) map.

The overall workflow for brownfield sites identification is illustrated in Figure 57. The first step is to search available brownfield information. It starts with a published database from a national or local authority where information is rather reliable. If no such kind of database is available or the information from official authorities is not up to date, crowdsourced information can be taken. Then, the vacancy of brownfields can be validated with certain criteria, such as low building temperature in winter, no or low human activity, and decreased sealing conditions. Up to this point, the site vacancy could still be uncertain. There are more indicators worth investigation based on additional data sources, such as contamination on the condition that free hyperspectral images are available. The more data sources, the better the validation of vacancy can be realized. It is an open question which open data sources can be further used to examine the site vacancy.

From the data fusion point of view, a continuous data fusion procedure takes place and a set of rules have been established. The first rule is to include possible brownfields by integrating information from a published database, OSM, and Wikidata. Then, thermal, social media, and sealing degree data are incorporated to validate the vacancy of the selected brownfields. For each data set, a specific rule is tailored according to the character of the vacant site. Later, the upcoming free data sources can also be added to the fusion procedure. Along with additional fused data, more brownfields will be identified as well as a more precise description of brownfields will be received.

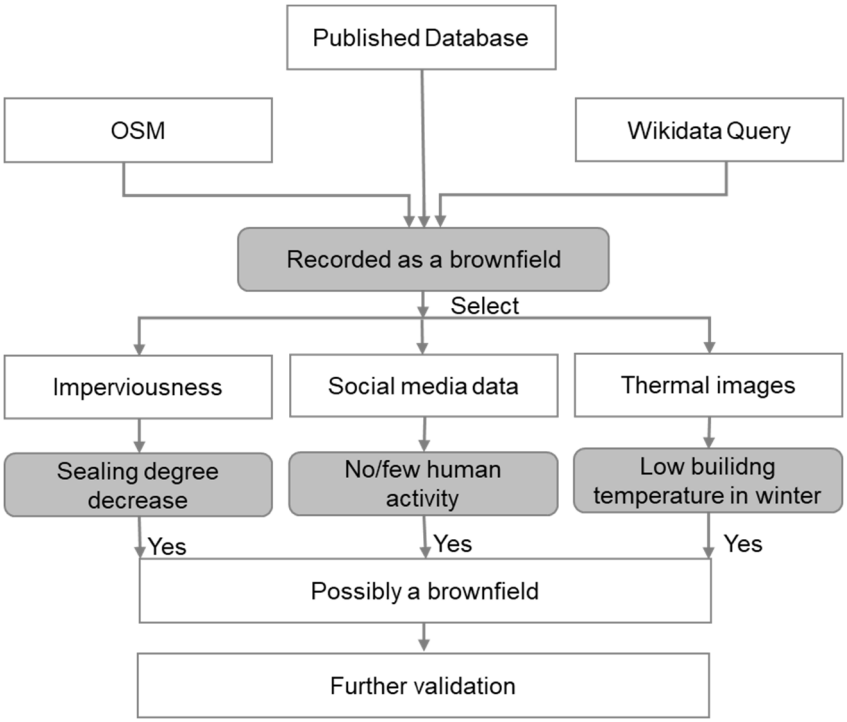

Figure 57 Incomplete data fusion procedure for brownfield identification.

The vacancy status of a brownfield is dynamic, which means it could change over time. Therefore, attention needs to be paid to the acquisition time of the used data in the data fusion procedure. It needs several rounds to validate the site vacancy. For each round, the used datasets should be collected in the same time period.

4.5. Vacant land identification results based on data fusion

Based on the mentioned data fusion procedures, all four types of vacant land were automatically extracted. In the following, the vacant land extraction results are presented. For each type of vacant land, at least one or two sites are illustrated with their appearance in Google Maps.

4.5.1. Transportation-associated land

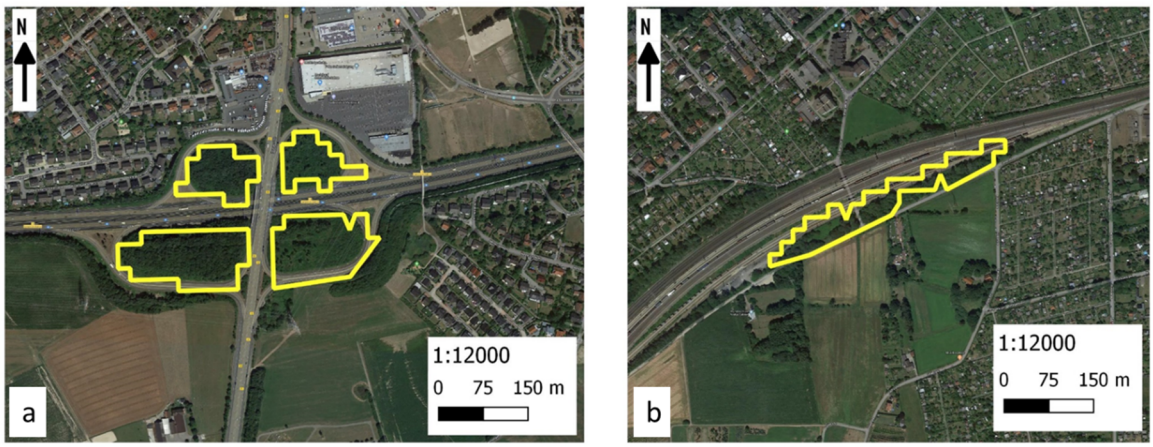

Figure 58 Two transportation-associated vacant sites: (a) highway related and (b) railway related.

The extracted transportation-associated vacant sites are sparsely distributed. Most of them are located at the highway junction and enclosed by the roadways, while a few of them are near the railways. Figure 58 shows two typical extract sites from the resulting layer. One is highway

related land and the other is railway related. The outline of the features is not smooth because it keeps the block pattern of the raster layer from which it was converted. Part of the outline of the features does not align with the green patch perfectly due to the low resolution of the imperviousness layer.

4.5.2. Natural sites

The natural sites are present in slightly higher quantity than the transportation-associated sites. These natural sites are distributed irregularly within the urban and suburban area. Within the city core, two extracted sites are beside rivers (Figure 59). Even though the land within the city core is prohibitively expensive, these two sites are still vacant. It is because the river bank has physical constraints and is not suitable for further development. These two sites fit the definition of this type of vacant land, which emphasizes that the vacancy is due to the unsuitable environment condition. A few more similar sites were also discovered near other rivers.

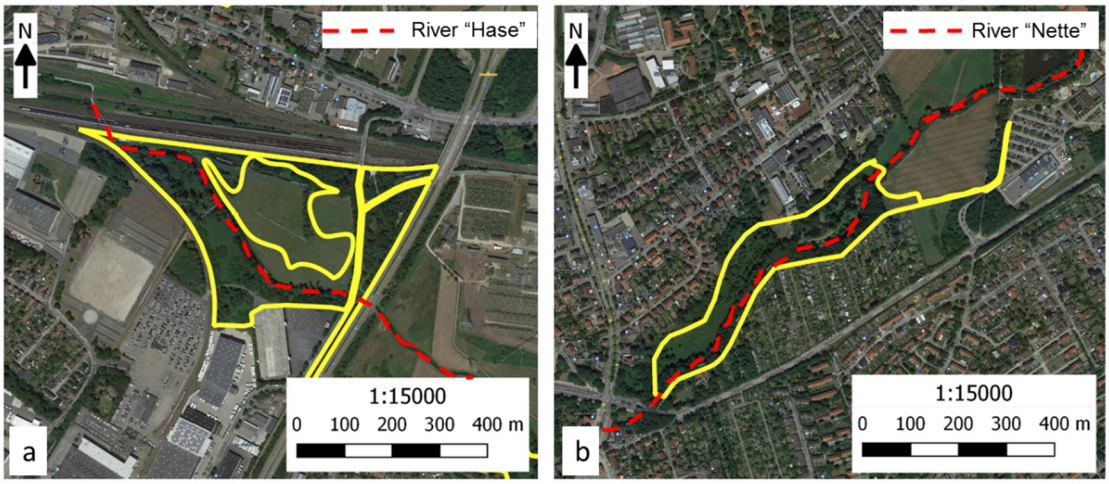

Figure 59 Two vacant natural sites at a riverbank.

Most of the extracted sites are located at urban outskirts which is the rural-urban fringe or the zone from built-up areas to non-built-up areas. Taking the four sites on Figure 60a as an example, which are located at the administrative border of the city of Osnabrück. Another 500 m away towards the north or west, there are already forest, agricultural, or suburban areas. These sites are enclosed by the urban fabric envelope and work as a bridge connecting built-up and agricultural areas. They are the leftover pieces from the process of urbanization. They can be gradually developed in the future. The vacancy of these sites is due to fragmentation caused by urbanization.

A few of the extracted sites have a similar situation as the sites in Figure 60a, but they are located at the border of suburban areas or small towns belonging to the county of Osnabrück. Figure 60b shows that in the town of Georgsmarienhütte, four *natural sites* were identified. These four sites appear as wooded areas within the town. Not far away from these sites, there are larger forest areas. Probably, the small patches were connected to the forests before and are now enclosed by built-up areas, which separated them from the larger forest.

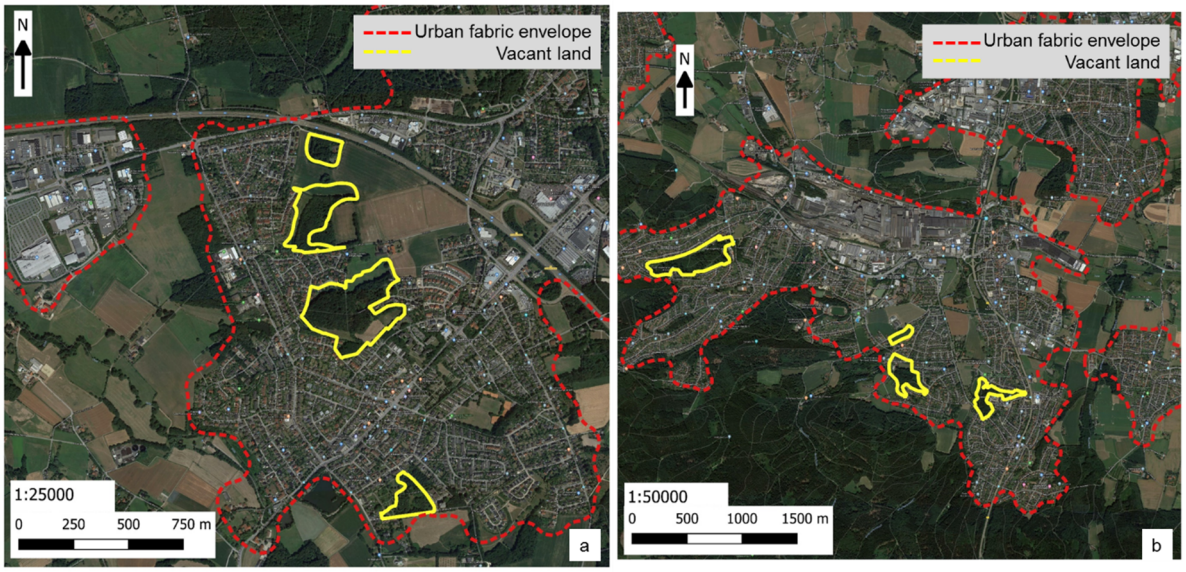

Figure 60 Vacant natural sites located (a) in the city area or (b) suburban area.

4.5.3. Unattended areas and remnant parcels

According to the appearance of the extracted sites, this type of vacant sites can be divided into four subgroups:

- sites beside the recreational ground,
- gaps in the built-up area,
- sites at a street corner or road section, and
- sites where transmission towers are located.

The first subgroup refers to the UA class *sport and facilities*. Thus, the extracted sites are located just beside recreational ground such as allotments (Figure 61a) or football fields (Figure 61b). These sites appear as tiny underwood areas and are the leftovers from recreational usage.

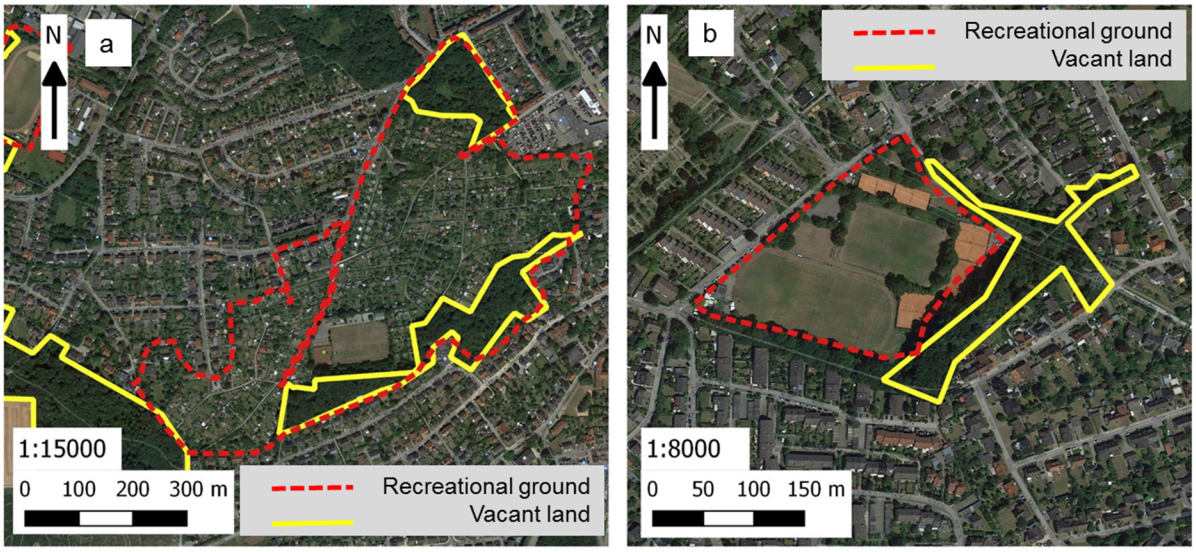

Figure 61 Two unattended areas and remnant parcels beside the recreational ground.

The second subgroup refers to the UA class *green urban area*. The identified sites generally have a very small size, often located in residential areas, and the reason for being vacant is not

clear, while the trace of usage is also not visible. These sites are equally distributed in the city of Osnabrück (Figure 62a and Figure 62b) as well as in the suburban areas or small towns in the county of Osnabrück (Figure 62c). They appear as vegetated gaps in the dense built-up area, with (Figure 62b) or without trees on site (Figure 62a and Figure 62c).

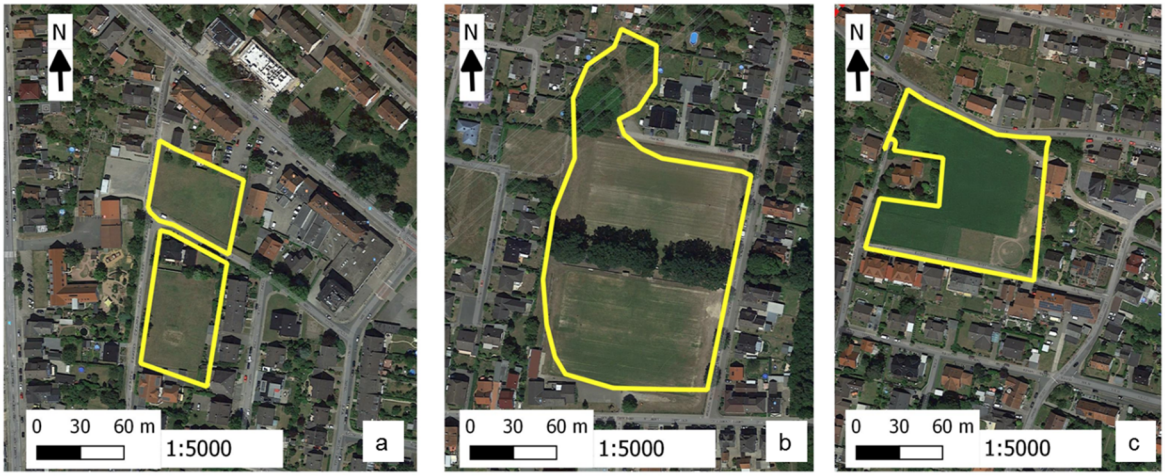

Figure 62 Vacant sites as gaps within built-up areas.

A part of the detected vacant sites appears at street or road corners (Figure 63) or is surrounded by streets or roads. These sites are fragments cut off by transportation systems. They are similar to *transportation-associated land* in nature, but could not be identified in section 4.5.1 because they were not included by the UA transportation-related classes.

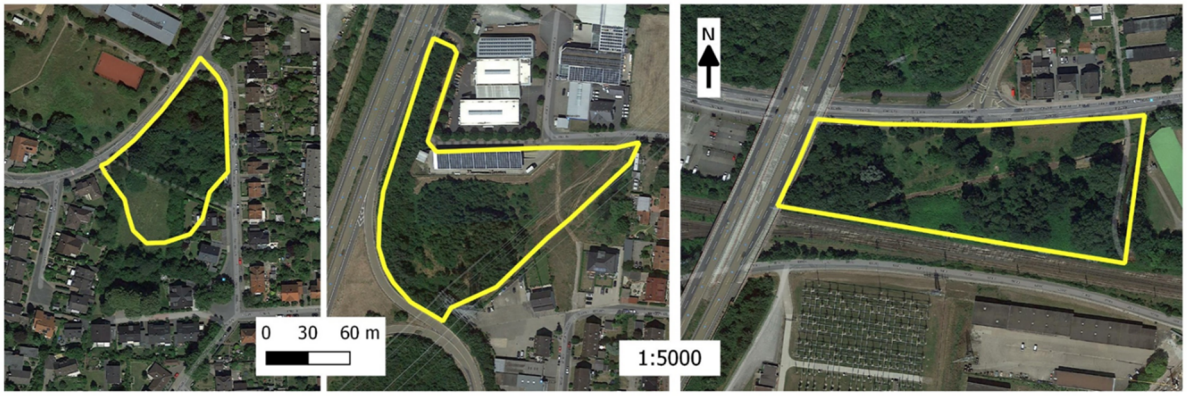

Figure 63 Vacant land appears at street or road corners.

Another special situation is that an electric power transmission tower occurs on the extracted sites (Figure 64, red arrow). The site vacancy was caused by doubts about building-up an area beside a transmission tower.

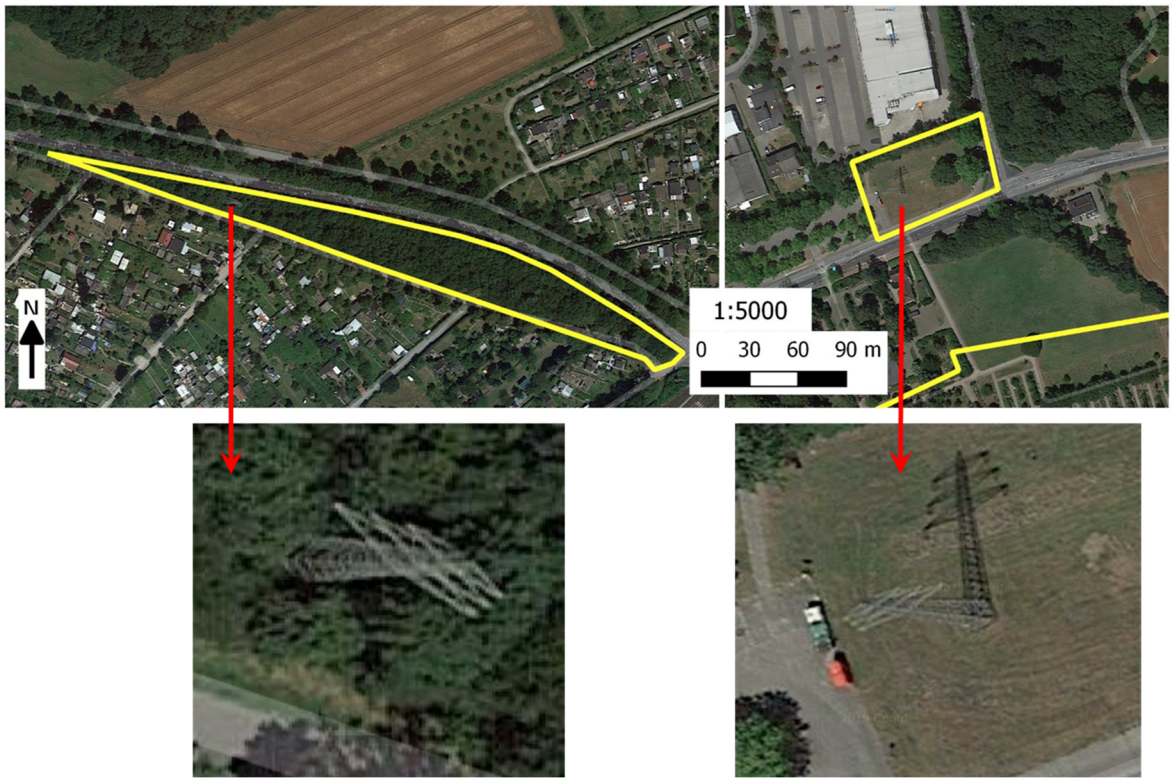

Figure 64 Vacant land caused by power transmission towers.

4.5.4. Brownfield

UA *mineral extraction and dump sites* are directly taken as potential brownfields. Beside this, no database for brownfields is published by the city of Osnabrück. Also, Wikidata and OSM do not have information about brownfields of Osnabrück. This is likely because brownfields are not a serious problem for the city. Only several abandoned barracks from the British Army were taken as brownfields. In 2006, the withdrawal of the British Army was announced, and about 160 ha of land was left to the city (Stadt Osnabrück, 2019a). The local authority has been working on converting these sites into proper use and named them as conversion sites. The map of these sites is published through the website of the city as Figure 65 shows (Stadt Osnabrück, 2019a). Some of these places were quickly reused due to their good condition. For example, the residential quarters for former highly-ranked officers were well-maintained, close to the city center, and offering various recreational facilities. They were thus sold out in 2011. Here, the focus is on the sites “Am Limberg” and “Landwehrviertel”, because the re-development plans were finished rather late in 2015/2016 (Stadt Osnabrück, 2019b). From 2007 to 2015, these sites were supposed to be empty. From then until now, the usage status has not been clarified.

Figure 65 Open brownfield information of the city of Osnabrück published by local authorities.

The activity map was created from the posts collected from Instagram and Twitter in 2016. Posts generated by humans were mostly distributed in the built-up areas. Within the built-up areas, the site "Am Limberg" has rather less human activity compared to the other places nearby. The human activity indicates that this site has neither been intensively used nor empty.

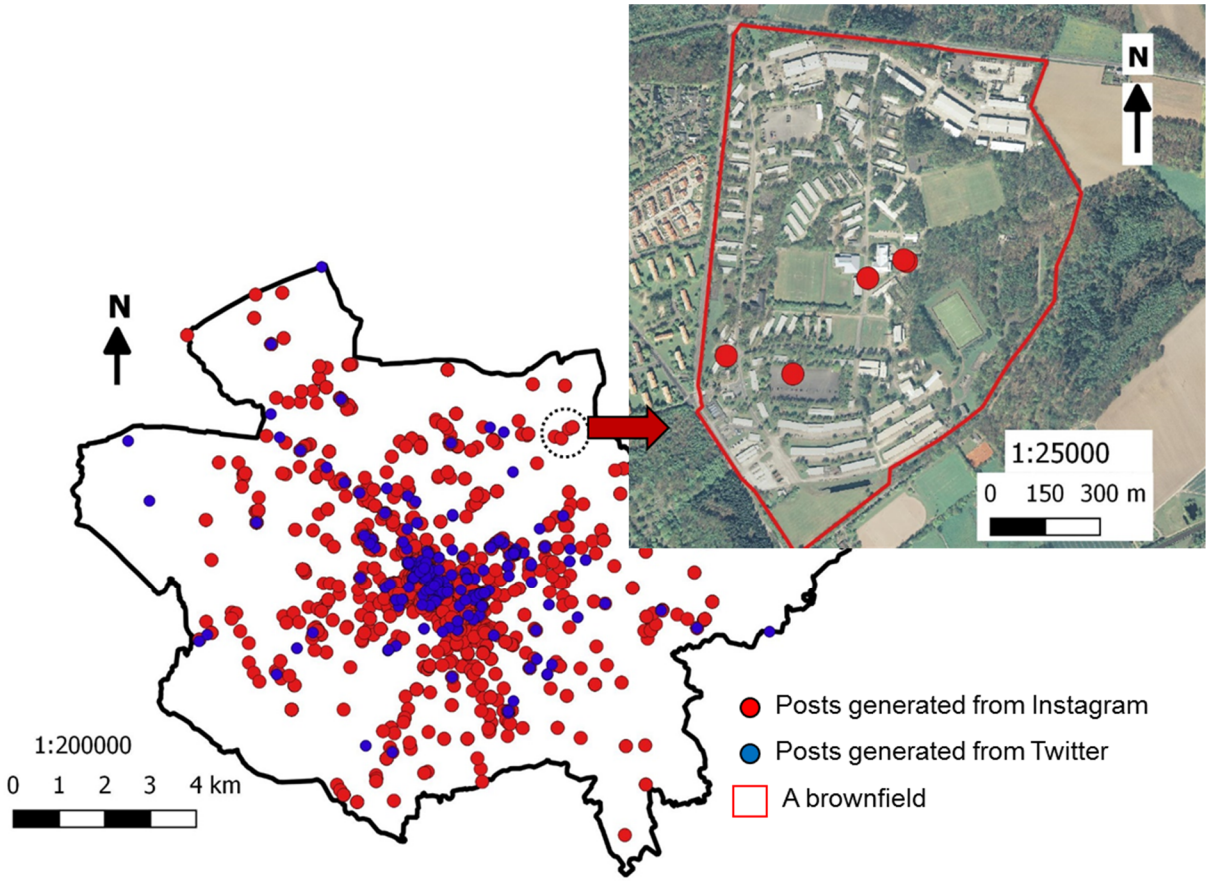

Figure 66 A human activity map created with social media data and its appearance in a brownfield in the city of Osnabrück.

As the data in the past was not collected, social media data only reflects the current status. Thermal data from 2007 to 2013 is available from Landsat 7, and from 2013 onwards available from Landsat 8. To gain information about the usage situation from 2007 onwards, the land surface temperature was examined.

Firstly, the nighttime data was investigated. Landsat 7 thermal images with the acquisition time 2011 were used. At nighttime, built-up areas have a higher temperature than the vegetation areas (concluded in chapter 3). But on the brownfield, the building area had a lower temperature than the vegetation area. Meanwhile, outside the brownfield, the buildings nearby showed a higher temperature than buildings inside (Figure 67a). This could mean that by that time this site was completely empty; the low temperature was caused by the lack of a heating in the abandoned houses.

After 2013, there were no nighttime thermal images available. Thus Landsat 8 thermal images captured during the daytime in 2015 were inspected. Figure 67b shows that in general, the temperature of the buildings within the brownfield is still lower compared to the nearby residential areas. However, within the brownfield some buildings show a higher temperature than others (Figure 67b, highlighted in red). Considering that at this location posts from social media have occurred, it could mean that this site has been partly used since 2015.

Nonetheless, it is still too early to draw a conclusion about the usage status of this brownfield. It is necessary to take a close look at the building area with the higher temperature. By comparison of the appearance of the site on the aerial photo (Figure 67c) and Google Maps (Figure 67d), it was found that the vegetation coverage increased. As a side note, the aerial photo was taken in 2014 and the image from Google Maps is up to date. This means that the roof of these buildings has been gradually covered by trees. Depending on the presence of shade provided by trees, the temperature of the buildings will change. In this case, the different building temperature could be caused by the different vegetation coverage, and therefore cannot be used as a criterion to indicate that the site has been used.

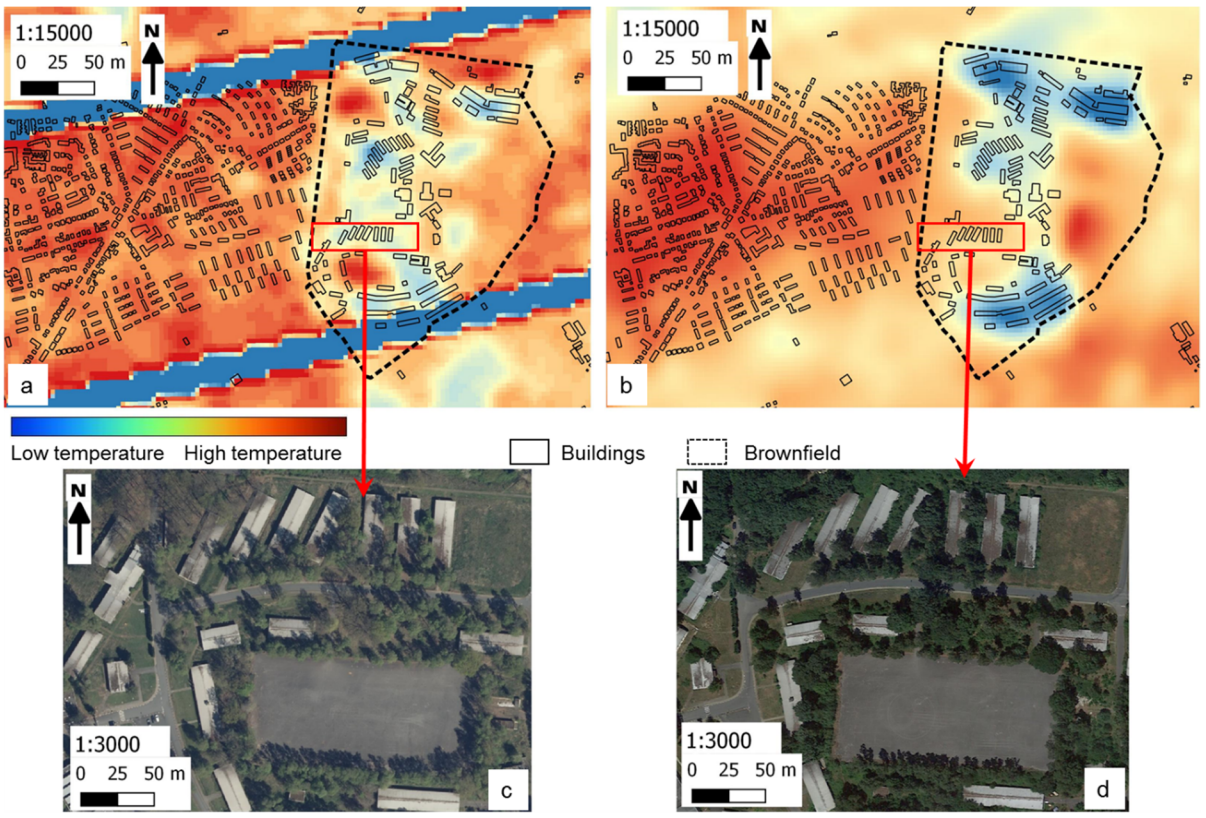

Figure 67 Surface temperature of a brownfield in (a) 2011 at nighttime; (b) 2015 during daytime; (c) aerial photo of the magnified building area in 2014; (d) its appearance on Google Maps.

Additionally, the increased vegetation coverage could be caused by lack of regular maintenance. This can be further validated by the sealing degree changes. If sealing degree has been decreased on a built-up site, it was abandoned. Thus, the imperviousness layers provided by Copernicus were investigated. However, the sealing change maps both from 2006 to 2012 as well as from 2012 to 2015 show no decrease in sealing. Other data is needed to further confirm if this site is still a brownfield. However, this is out of the scope of this thesis, because as mentioned in section 4.4.4, it is a continuous data fusion procedure along with new upcoming data.

In brief, all four types of vacant land have been extracted. All site selection was done with the software QGIS, which is a free and open source GIS platform. The operations mentioned in the site selection procedure, such as selection, overlapping, and clipping were realized by the data processing tools or the spatial quarry tool. The software is fully equipped with common data analysis and processing tools. Additionally, it provides sufficient plugins for special applications. For instance, the *group stats* plugin was used to calculate the basic statistics of the features on a layer. All these plugins are also free to download. Table 9 shows the basic statistics of the extracted sites which were calculated by using the *group stats* plugin.

As the statistical information indicates, the *unattended areas and remnant parcels* have the largest total number and total area. A related point to consider is that this kind of vacant site is extracted from three separated parts: *urban green areas*, *sport facilities*, and *land without current use*. Subsequently, brownfields account for the second largest total area of vacant land. They have a bigger average area than each of the other three types. The listed 83 brownfields are mineral extraction and dump sites, whose vacancy has not been validated individually. Strictly speaking, they are just possible brownfields but still list here to provide a complete overview of the vacant site property. The other two brownfields “Am Limberg” and “Landwehrviertel”, with a size of 70 ha and 37 ha respectively, are not included in Table 9, because the validation procedure indicated that they could have been recycled. Transportation-associated sites have the smallest average size and total area.

Table 9 The statistics of extracted vacant sites in the city and county of Osnabrück.

Vacant land	Count	Sum in ha	Mean in ha	Median in ha
Transportation-associated land	52	66.74	1.28	1.01
Natural sites	61	230.26	3.77	2.53
Unattended areas and remnant parcels	473	1169.46	2.47	0.92
Brownfields	83	659.78	7.95	3.73

Through ground truth validation, it was found that one golf field, two allotments, and a part of the zoo of Osnabrück were also identified as vacant sites. This is due to the incomplete land use information on OSM. The golf field and the zoo are identified as sport and facilities by UA, and identified as forest by OSM. Therefore, they could not be filtered out by the data processing procedure. This means that the imperfections of the source data is causing inaccurate results. Additionally, it was found that within a few identified vacant land sites, houses appear. This could be because the UA data is from 2012, while the background Google Maps image is up-to-date, suggesting that the houses have been built up after 2012. Overall, inspection of the selected sites on Google Maps reveals that a high accuracy of site identification has been achieved.

4.6. Development potential of vacant land for sustainable urban development

Vacant land indicates a low land-use efficiency which directly leads to excessive urban sprawl. The extracted vacant land can be reused for development or for conservation to enhance the urban ecosystem.

4.6.1. Development potential of vacant land

In the definition phase of the vacant land typology, four types of vacant land have been orientated towards development or conservation. Through inspection of the overall detected sites, the further development potential of each type of vacant land is suggested by its site properties.

Natural sites have a large size and dense vegetation. Some of them are near or at a river bank. These sites might hold natural forest or enough space as a habitat for native flora and fauna. If not, they can be used for various purposes such as the reduction of air and noise pollution, to release UHI effects, and to mitigate the negative impact caused by urban sprawl. In brief, preservation should be taken as the priority for this type of vacant land.

Transportation-related land partly belongs to road junctions which can only be preserved, and partly belongs to areas enveloped by roadways. If the roadways surround the site completely from all sides, then it can also only be preserved due to the lack of an entrance. If at least one side of the area is accessible, it could still be used for other purposes.

Unattended areas and conservation sites might also be covered by trees like natural sites. However, they are of much smaller size. The most distinctive feature of this type of sites is that they look like gaps in regular and dense built-up areas. These gaps can be easily filled according to the surrounding land use conditions. For example, gaps between houses can be filled with new houses, and vacant spaces within allotment areas can be further extended into new gardens. This type of vacant site is suitable for further utilization.

The most special character of brownfields is that they have been used before. If the existing buildings and structures are in good condition, they can be directly reused. If not, they also should be recycled for efficient land use purposes.

In conclusion, the development potential increases in the order of *natural site*, *Transportation-associated land*, *unattended areas and remnant parcels*, and *brownfields*. Meanwhile, conservation potential decreases. This was ordered based on the basic character of each type of vacant land and is consistent with the development orientation assumed in the vacant land definition (see section 4.2.3).

However, this conclusion is just a primary judgment for development suitability of all kinds of vacant sites. During practical implementation, more factors need to be taken into consideration. Firstly, there are always exceptions which deviate from the basic character. For example, if a natural site is rather smaller than the usual size and near a dense residential area, then it might be suitable for residential use. Secondly, unfavorable conditions need to be noticed, such as electric power on site. Thirdly, the overall condition should be evaluated with additional criteria. For development purposes, the factors include the size, shape, slope, connection to a

road network, energy and water infrastructure, contamination level, remediation costs, flood risk, and environmental protection zones. For conservation planning, factors such as the vegetation quality, biodiversity, and green connectivity must be considered. Moreover, for each city, it is also necessary to consider specific situations, such as the pressure on land use caused by increasing land demands and particular requirements from end-users. The final decision for the development of a vacant site could be the opposite of the primary decision for it. Taking brownfields as an example, in most cases, they are suitable for reuse, but the uncontaminated sites can become a conservation area after vegetation improvement and ecosystem enhancement.

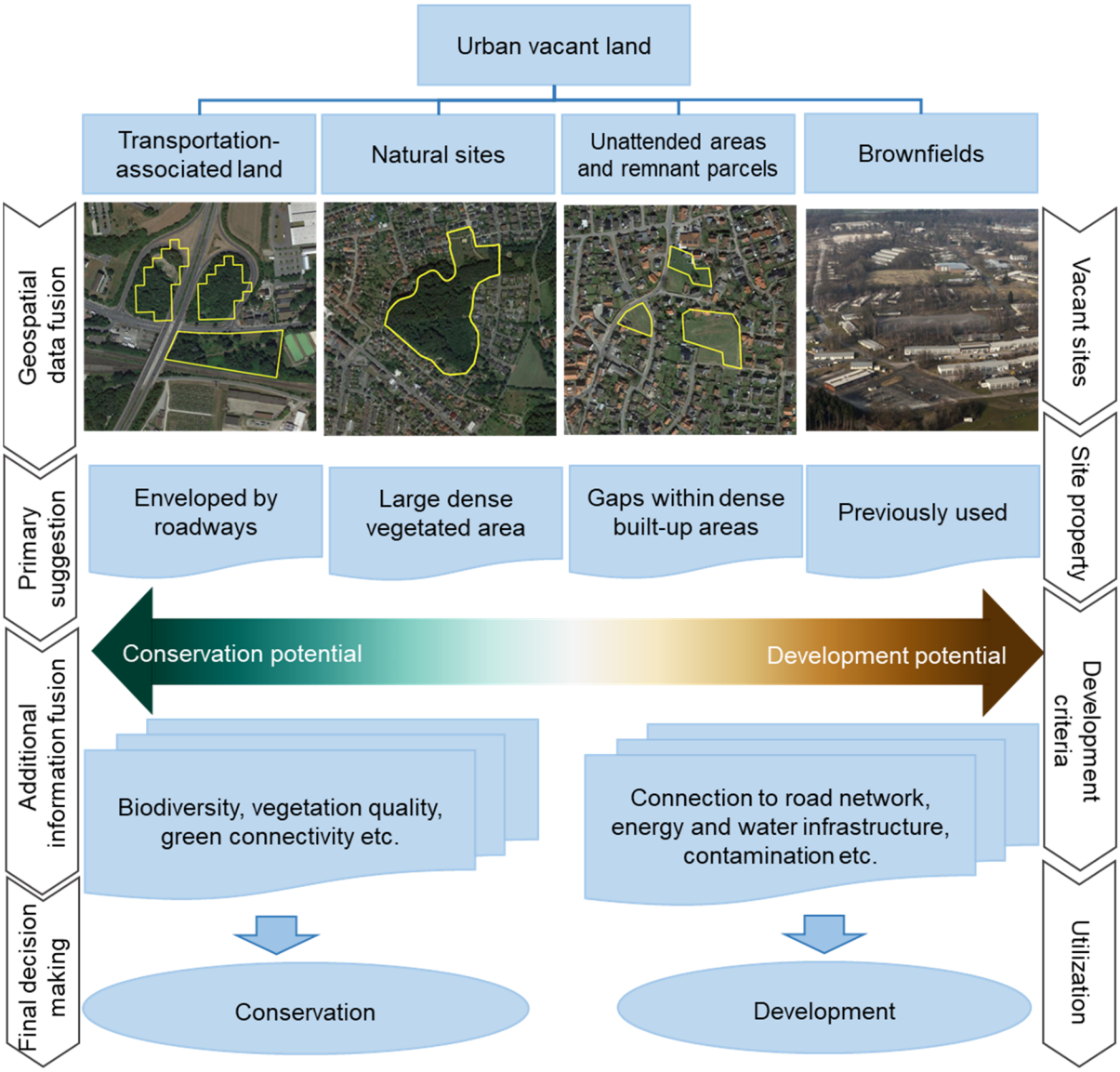

Figure 68 Overall decision-making procedure for vacant land development.

Figure 68 shows the overall procedure to decide the development of urban vacant land. For each type of vacant land, the site identification is completed by open geospatial data fusion. The basic characteristics of the extracted vacant sites point in the direction of the development so that a primary suggestion can be provided. Yet, the final decision for the utilization of the vacant site is much more complex and more criteria should be taken into consideration. Therefore, additional information needs to be fused together to decide if a site should be conserved or further developed. It could happen that for one criterion, several data sets must be

incorporated together. The decision also depends on which criteria have priority or are more important, which varies from development purposes (e.g. residential area or hospital) and different end-users. A multi-criteria decision-making system could be applied here. The detailed decision-making guidelines, however, are outside of the scope of this thesis.

4.6.2. Vacant land for sustainable urban development

After the final decision has been made for the utilization of vacant land, it will generate environmental, economic, and social impacts on urban areas which are spelled out in the following:

Development of vacant land will reduce urban land and soil sealing. Urbanization-driven soil sealing produces negative impacts on the urban environment. Due to intense industrialization, the soil quality in urban areas is degraded by accumulated heavy metals (Hu *et al.*, 2013). Rainwater which flows through the sealed surface can be polluted by tire rubber residues (Councell *et al.*, 2004; Edil, 2008). When the water is finally washed into rivers, the hydrological environment will be harmed (Ramanathan *et al.*, 2001). Soil sealing and compaction reduces rainwater penetration and increases surface runoff. Consequently, the flood arrival time will be shortened and flood damage will be increased (Murata and Kawai, 2018). Intensive urban soil sealing reinforces the UHI effect which causes uncomfortable summers. Part of the vacant land can also be upgraded into natural conservation sites which will reduce environmental impairment caused by soil sealing.

Land recycling or reuse of brownfields creates new market opportunities for estate agents and private individuals. From the land and property development perspective, vacant land provides additional land for households and enterprises and reduces the negative economic effects caused by a tight housing market. Development of vacant land increases urban land use efficiency and slows down the process of suburbanization. As a result, it saves cost on commuting from home to work and the extension of urban infrastructures between urban and suburban regions. Abandoned sites will weaken cities' attractiveness and competitiveness, and thus harming the local economy.

Longtime abandoned buildings or houses could become unsafe areas that may be used for illegal activities. The neighborhood may be distressed unless the redevelopment starts. The underused gap places in dense built-up areas can be developed into a playground and recreational areas, providing desirable ways of living and working. Meanwhile, the vacant sites which are suitable for natural conservation will improve the urban air quality and reduce urban noise which will directly improve the quality of life and human health (Sandifer *et al.*, 2015). Vacant land development will improve the land use efficiency and therefore reduce risk to human safety when the urban area exceeds the flooding zone. The decision for vacant land development often involves the local communities, in a form of deliberative policy-making Therefore, public participation can improve communication between citizens and the government, build strategic alliances, and avoid litigation costs.

In summary, this chapter firstly reflects on the issues appearing in the URBIS project. Even when various data sources were used, inaccurate vacant land mapping results were produced. Such an ineffective data fusion was mainly caused by the unclear vacant land typology. This

thesis thus proposes a new vacant land typology. The defined typology takes UA vacant land-related classes into consideration and characterizes vacant land into four types. The definition of vacant land also indicates two levels of data fusion: on the feature level, the vacant sites are identified; on the decision level, the utilization of the vacant site can be decided. The feature level fusion was done before the decision level, while mixing of these two levels caused the confusion in the URBIS project.

This chapter focuses on the geospatial data fusion on the feature level. For each type of vacant land, a detailed data fusion procedure was illustrated. For identification of transportation-associated land, UA vector layer and imperviousness raster layer were combined. To extract the natural sites, UA classes were integrated with the CLC map. To find the unattended area and remnant parcels, the fusion was between UA classes and OSM land use information. Brownfield was most challenging to extract; UA, social media data, thermal images, Wikidata, and published databases were used. This fusion procedure can be extended to include further data sources. Using this typology, the extracted sites fit the original expectation. Various types of vacant land have been successfully identified for the study area. Depending on the site properties, decisions on whether to re-use or re-develop this vacant land can be made by fusing with additional information.

In chapter 5, the data fusion results together with the results from the two application cases are summarized to derive a conclusion about how to conduct data fusion in an effective way to benefit sustainable urban development.

5. Conclusion and Outlook

This chapter summarizes the results of the thesis in order to reflect on all the research questions raised in chapter 1. Furthermore, it provides an outlook about geospatial data fusion research and practice.

5.1. Conclusion

The importance of geospatial data for sustainable development has been recognized world-wide (UN, 2012). Chapter 1 reviewed many of the issues impacting sustainable development that were analyzed, modeled, and mapped with geospatial data. From all sorts of geospatial data, those from open sources were emphasized in this thesis because they are in line with the principles of sustainable development as argued in chapter 1. Data fusion techniques integrate all sorts of open geospatial data together and increase their power to further foster the implementation of sustainable development. However, sustainability is often viewed as an abstract goal due to the complex concept and difficulties in execution. Therefore, this thesis examines application cases to illustrate how open geospatial data fusion provides key and reliable information to achieve sustainable development.

The first step of using open source geospatial data is to collect the available datasets. Remote sensing satellite images were focused on as they are the richest source of open data and can be analyzed and interpreted for the use in various urban development applications and purposes. Most satellites offer the repetitive acquisition of coverage of the Earth's surface and these images can thus be easily processed to explore dynamic themes, such as land cover changes and urban sprawl. The biggest disadvantage of open satellite images is the low spatial resolution which limits its utilization on urban areas.

Existing image fusion algorithms could neither sharpen a one-band thermal image nor keep the spectral information of hyperspectral images through image sharpening. Therefore, the simplified Ehlers fusion was developed. This algorithm discards the IHS transformation from the original Ehlers fusion, which requires the original image to consist of at least three bands. In this way, it breaks the limit of the number of bands required for image sharpening. By using an FFT, the simplified Ehlers fusion processes image enhancement in the frequency domain. No matter which sensor recorded the image or which spectral coverage it provides, all of them can be transformed into different frequency elements. Hence, it overcomes the disadvantage of most of the image fusion algorithms which only work well when the input images are from the same sensor and cover similar spectral regions. The algorithm could realize effective spectral preservation and spatial enhancement at the same time because the spectral and spatial information are separated along with different frequencies. High frequencies represent the detailed spatial information. Then, filter techniques were applied to allow suitable high frequencies to pass through and form a new image. The range and the amount of frequencies which will pass through can be controlled by the type and size of the filters. This is particularly useful for images from urban areas because the filters are adjustable to exactly match the urban features. The advantages of this algorithm are summarized in the following:

- It is flexible with the number of bands of the target image,
- the target image and high-resolution source image can be from different sensors, as it has been tested using Landsat 7 and Landsat 8, Landsat 8 and ASTER, as well as aerial photos and hyperspectral images,
- the sharpening effect is adjustable through the types and sizes of filters, and
- it is also suitable for images which have multi-bands with different spatial resolutions.

The fusion algorithm was tested with one band thermal images as well as with hyperspectral images with hundreds of bands. By visual inspection, the fusion results show excellent spatial improvement and color preservation. Quantitative quality evaluation was also applied, and the results show that simplified Ehlers fusion outperforms the classic fusion methods. However, the quantitative quality assessment was not focused on because the commonly used quality evaluation indices are statistical functions. In chapter 2, it is demonstrated that statistical methods calculate the pixel value differences between the original image and the fused image. As spatial enhancement will no doubt introduce pixel value changes, these methods are therefore not suitable for assessing spatial quality improvement. Additionally, these statistical methods can be influenced by image processing procedures such as geo-registration, image clipping, and resampling which are unavoidable procedures in image fusion. Therefore, it is not necessary to pursue perfect results from the quality assessment indices; rather it is important to investigate if the sharpened image provides improved performance in the application context.

The developed fusion algorithm was then implemented in a first application case, mainly focused on improving the spatial resolution of thermal images for UHI analysis. Compared to the fusion process in the experiment presented in chapter 2, more factors need to be considered in the application case, such as the atmospheric correction and particular data acquisition time. For UHI analysis, nighttime data is crucial. Thus, Landsat 7 and ASTER nighttime images were chosen. Landsat 8 images were also included due to its frequent repetitive data acquisition.

Simplified Ehlers fusion was applied between the Landsat 8 panchromatic band and the thermal bands from Landsat 7, ASTER, and Landsat 8 respectively. In the application of open geospatial data fusion, weather, atmospheric, and other conditions of the image were unavoidable factors influencing the fusion effect. The fusion between Landsat 8 and ASTER was influenced by the clouds and snow appearing on the images, while the fusion between Landsat 8 and Landsat 7 was affected by the erroneous stripes on the Landsat 7 images.

Even with these unfavorable conditions, spatial improvement was achieved in the fused thermal images. It was possible to reveal that temperature differs between agriculture and forest because the border between them was spatially enhanced. Through image fusion, the temperature difference within built-up areas could also be discovered, which is not distinguishable in the original thermal image. In brief, by applying the simplified Ehlers fusion to the thermal images, spatial information was increased and more spatial details were visible. Thus, the open geospatial image could provide a more accurate measurement of the surface temperature in the urban area.

Based on the fused thermal images, the UHI effect on the city of Osnabrück during daytime and nighttime could be analyzed. In this way, the main factors contributing to the heat effect were revealed. Based on these outcomes, it is suggested that UHI mitigation actions should be

focused on making use of industrial waste heat, reducing the temperature rising in dense built-up areas such as by using reflective roofs and increasing green spaces, as well as utilization of cool pavements.

The first application case showed that data fusion is remarkably beneficial for analysis of urban issues. However, low spatial resolution is not the only barrier that limits the use of geospatial data in urban research. The results of the URBIS project, chosen because of its open source data approach, show that even with very high resolution satellite images (5 m), the extracted urban vacant sites are not in agreement with ground truth data. However, the undesirable results show that inappropriate piling-up of various data sets can lead to meaningless results.

Therefore, the second application focused on the identification of urban vacant land. Before applying data fusion techniques, it was necessary to precisely understand the research target in the context of urban development. For instance, vacant land refers to land recycling while GOS correspond to urban sprawl. Mixing them together will increase the difficulty in site detection. The main reason causing the unsuitable outcome in the project was the unclear definition of the vacant land typology. To define the vacant land in a way that enables their extraction using geospatial data, the differences between vacant land, brownfields, as well as GOS first needs to be clarified. Secondly, the data availability and its properties were investigated. The feasibility of identification of vacant sites using open source data depends on the availability in UA. Thus, the definition of vacant land matches the UA classes to a maximum extent. Finally, the definition also provides the general data fusion framework: from the horizontal view, it includes data fusion on the feature level and decision level; from the vertical view, each type of defined vacant land needs an individual data fusion process.

The dependence on UA for site extraction decreases from (1) *transportation-associated land*, (2) *natural sites*, (3) *unattended areas and remnant parcels,* to (4) *brownfields*. At the same time, the complexity of the necessary fusion procedures increases from (1) to (4). For each type of vacant land, data fusion was done between different datasets, such as a combination of UA and OSM data, as well as the integration of UA and CLC data. In each of these four data fusion processes, a rule-based data fusion approach was applied. The fusion rules decided the role that the datasets play in the procedures.

The identification of brownfields was most challenging because its vacancy changes over time. Thermal images, published brownfield databases, posts from Instagram and Twitter, Wikidata, and OSM land use information were involved. Data from agencies or authorities such as UA, imperviousness layer, satellite images, and databases were first taken into consideration as they are reliable and have been validated. Data from citizen science such as OSM and Wikidata were also used because OSM provides crucial land use information and Wikidata offers valuable information about brownfields. Even though citizen science has issues of completeness and reliability, the information that it provided could not be obtained for free from other sources. Social media data was used as an indicator of site vacancy. It plays a role which is not replaceable, as it reflects human activities. Moreover, this fusion procedure can be extended to new upcoming data.

Compared to the first application case, in which mainly satellite images were used, the second application case combines multi-source datasets of different nature. This is because UHI

analysis mainly relies on thermal images, whereas vacant land is a much more complex research object. It contains several types, appears with different land covers, and involves different land uses types. It is shown that with a clear definition of the urban object, data fusion can act as a powerful tool to extract the desired information. The extracted vacant sites, on the one hand, can be used for redevelopment, increase land for construction, and reduce urban sprawl from taking more land from agriculture and forest. On the other hand, they can also be used for conservation and/or green infrastructure enhancement.

The two application cases present data fusion techniques from different perspectives: one focuses on data fusion in depth and the other one emphasizes data fusion in breadth. In the first case, two images were fused together to generate one more informative image. In the second case, various data sets were combined. During the data fusion process, the source data was not edited, but useful information was selected out from each data set to create a combined data set.

In the first application case, MATLAB was used for image sharpening while QGIS was used for image processing. In the second application case, only QGIS was used as the data processing and analysis platforms. In this way, it could be shown that urban issues such as vacant land can be analyzed entirely using open source data and software. This fulfills the goal of this thesis which aims to use only open sources for sustainable urban research.

5.2. Outlook

Continuing population growth and urbanization has resulted in a situation where cities occupy just 2% of the Earth's land but account for 60% to 80% of total energy consumption and 75% of carbon emissions (UN, n.d.). In most western European countries, it is expected that the urban population will increase to above 90% (EEA, 2017). Urbanization brings increasingly more issues where sustainable development needs to be implemented (EEA and FOEN, 2016). Open geospatial data fusion can provide sufficient, accurate, irreplaceable, and up to date information for urban research for sustainability.

With the proliferation of open geospatial data and higher availability to the public, more data can be integrated into the fusion procedure. Sensor web, as one of the four open data sources, have not been used in this study. Because different sensor manufacturers come with different protocols, integrating diverse sensors is not straightforward (Bröring *et al.*, 2011). The integration of sensor web data will bring real-time information for urban applications and are therefore of great interest. The author of the thesis proposes that open geospatial data should be used to study sustainable urban development. However, since there were no available open source hyperspectral data available, hyperspectral data were only used for testing the developed algorithm but not for application cases, The Environmental Mapping and Analysis Program, aimed at providing hyperspectral data at a global scale, is currently in the development and production phase (http://www.enmap.org). In the future, the produced data in combination with other open data will permit the application of geospatial data fusion to a large extent. This means that on one hand, the data fusion procedure could become more complex; on the other hand, geospatial data fusion will become a more powerful tool and more useful information can be extracted.

This thesis raised the drawback of current indices for quantitative evaluation of fusion quality but has not made any suggestions on alternative options. Some ideas referring to this issue seem very promising. For example, Pohl *et al*. (2017) proposed a standardized process to objectively assess fusion quality. It includes a quality protocol and a visual quality protocol. However, this proposal is still multispectral-image-oriented, and further adaptation is needed to make it also fit to one band or hyperspectral images. Fusion quality is crucial for the assessment of image fusion algorithms. Further research on quality evaluation would contribute to this study. In addition to this long-term outlook, this thesis opened four research lines that could be explored in the near future.

Simplified Ehlers fusion was programmed in MATLAB, following the original source code of Ehlers fusion. However, MATLAB is a commercial software. It will be beneficial for many users if the simplified Ehlers fusion algorithm could be integrated into open source software. GRASS GIS is an optimal platform to implement this idea because it is a free and open source software which provides commands for an FFT (operation i.fft) and an inverse FFT (operation i.ifft). Additionally, it can be used to generate high-pass, low-pass, as well as donut filters (e.g. operation r.circle). With all of these conditions, the software is poised to apply the algorithm. GRASS GIS also encourages users to develop their own unique tools and offers guidelines and documentation to develop extensions. In the future, the simplified Ehlers fusion can be further developed into an add-on. It would also be a necessity to set up a function to quantitatively measure the computing time. In contrast to Ehlers fusion, the program loop in simplified Ehlers fusion does not use IHS transformation but goes band by band. It would be very interesting to compare algorithm efficiency in terms of computing time.

The *UHI* analysis of the city of Osnabrück encountered the problem of insufficient satellite images taken at nighttime. This was because Osnabrück has not been closely monitored by such satellites. In contrast, for megacities like Shanghai, nighttime thermal data can be retrieved from Landsat 8. If applying the method developed in this thesis to megacities, the Landsat 8 nighttime thermal images can be sharpened and the UHI phenomenon in megacities can be investigated more deeply.

Vacant land extraction in this work was based on UA which offers data for the city and county of Osnabrück only from the year 2012. For 305 major European cities, it provides data from the year 2006 and 2012. In the future, the data from 2018 will also be published. Therefore, it is possible to extract vacant land from different years, to investigate if the vacant land has increased or decreased. A city with increased vacant land should re-consider its urban development plan. In this thesis, about 1400 ha of vacant land for the city and county of Osnabrück was detected. If the same method could be carried out in the other 300 European cities, it will reveal a considerable amount of vacant land suitable for urban development. Moreover, when merging the extracted vacant land together with agricultural land and forest area, a complete GOS layer can be formed. This layer can be used to analyze urban sprawl, urban green connectivity, and urban land fragmentation.

Open geospatial data is rapidly expanding, which will provide more sources of data. In the future, more satellite images will be available. For example, Sentinel-4 has two missions that are planned to be launched: the first one in 2019 and the following in 2027. The project for updating Copernicus high resolution layer kicked off in January 2019 (GAF, 2019), which

means more GIS data will be published later. Citizen science will be pushed forward because volunteers are encouraged to collect and report geospatial data, such as the EU biodiversity Strategy to 2020 (European Commission, 2011) which considers citizen science initiatives as valuable means for biodiversity conservation. All of this will lead to even broader data fusion, as well as more applications for researching urban sustainable development.

When dealing with urban issues, due to the rather small scale of urban objects, high-resolution data is more desirable, which favors commercial data. Consequently, geospatial data has been pushed to an ever higher resolution—up to millimeters. However, changing this perspective may lead to the development of creative solutions to work with and provide more open data despite their lower resolution. In this way, the UN endorsement of integrating geospatial information into sustainable development plans (UN, 2015) can be realized even in poorer regions of our planet, leading to truly global sustainable development.

Bibliography

Abdi, A.M., 2020. Land cover and land use classification performance of machine learning algorithms in a boreal landscape using Sentinel-2 data. GIScience Remote Sens. 57, 1–20. https://doi.org/10.1080/15481603.2019.1650447

Agam, N., Kustas, W.P., Anderson, M.C., Li, F., Neale, C.M.U., 2007. A vegetation index based technique for spatial sharpening of thermal imagery. Remote Sens. Environ. 107, 545–558. https://doi.org/10.1016/j.rse.2006.10.006

Aja-Fernandez, S., Estepar, R.S.J., Alberola-Lopez, C., Westin, C.-F., 2006. Image Quality Assessment based on Local Variance, in: 28th Annual International Conference of the IEEE Engineering in Medicine and Biology Society. IEEE, pp. 4815–4818. https://doi.org/10.1109/IEMBS.2006.259516

Akbari, H., Cartalis, C., Kolokotsa, D., Muscio, A., Pisello, A.L., Rossi, F., Santamouris, M., Synnef, A., Wong, N.H., Zinzi, M., 2015. Local climate change and urban heat island mitigation techniques – the state of the art. J. Civ. Eng. Manag. 22, 1–16. https://doi.org/10.3846/13923730.2015.1111934

Al-Ruzouq, R., Hamad, K., Shanableh, A., Khalil, M., 2017. Infrastructure growth assessment of urban areas based on multi-temporal satellite images and linear features. Ann. GIS 23, 183–201. https://doi.org/10.1080/19475683.2017.1325935

Ali, H., Choi, J., 2019. A Review of Underground Pipeline Leakage and Sinkhole Monitoring Methods Based on Wireless Sensor Networking. Sustainability 11, 1–24. https://doi.org/10.3390/su11154007

Alker, S., Joy, V., Roberts, P., Smith, N., 2000. The Definition of Brownfield. J. Environ. Plan. Manag. 43, 49–69. https://doi.org/10.1080/09640560010766

Alonzo, M., Roth, K., Roberts, D., 2013. Identifying Santa Barbara's urban tree species from AVIRIS imagery using canonical discriminant analysis. Remote Sens. Lett. 4, 513–521. https://doi.org/10.1080/2150704X.2013.764027

ArcGIS, 2019. ArcGIS Hub - Open Data [WWW Document]. URL https://hub.arcgis.com/pages/open-data (accessed 4.15.19).

Artis, D.A., Carnahan, W.H., 1982. Survey of emissivity variability in thermography of urban areas. Remote Sens. Environ. 12, 313–329. https://doi.org/10.1016/0034-4257(82)90043-8

Aytekın, Ö., Erener, A., Ulusoy, İ., Düzgün, Ş., 2012. Unsupervised building detection in complex urban environments from multispectral satellite imagery. Int. J. Remote Sens. 33, 2152–2177. https://doi.org/10.1080/01431161.2011.606852

Bakillah, M., Liang, S., 2016. Open geospatial data, software and standards. Open geospatial data, Softw. Stand. 1, 1–2. https://doi.org/10.1186/s40965-016-0004-1

Ban, Y., Hu, H., Rangel, I.M., 2010. Fusion of Quickbird MS and RADARSAT SAR data for urban land-cover mapping: object-based and knowledge-based approach. Int. J. Remote Sens. 31, 1391–1410. https://doi.org/10.1080/01431160903475415

Baranka, G., Bozó, L., Ciglič, R., Komac, B., 2016. Urban Heat Island Gold Standard and Urban Heat Island Atlas. Gold Standard for UHI Measurements and Introduction of The Central-European Urban Heat Island Atlas, in: Musco, F. (Ed.), Counteracting Urban Heat Island Effects in a Global Climate Change Scenario. Springer, Basel, Switzerland, pp. 41–70. https://doi.org/10.1007/978-3-319-10425-6_15

Bäumker, M., Heimes, F.J., 2002. New Calibration and Computing Method for Direct Georeferencing of Image and Scanner Data Using the Position and Angular Data of an Hybrid Inertial Navigation System, in: Heipke, C., Jacobsen, K., Wegmann, H. (Eds.), Integrated Sensor Orientation. Test Report and Workshop Proceedings. European Organization for Experimental Photogrammetric Research. Federal Agency for Catography and Geodesy, Frankfurt am Main, Germany, pp. 197–212.

Bayerisches Landesamt für Umwelt, 2018. Flächenmanagement [WWW Document]. URL https://www.lfu.bayern.de/umweltkommunal/flaechenmanagement/index.htm (accessed 4.15.19).

Beauchemin, M., Fung, K.B., Geng, X., 2002. A Method Based on Local Variance for Quality Assessment of Multiresolution Image Fusion. Int. Arch. Photogramm. Remote Sens. Spat. Inf. Sci. 34, 32–35.

Bhattacharjee, K., 2010. Energy Conservation Opportunities in Industrial Waste Heat Recovery Systems. Energy Eng. 107, 7–13. https://doi.org/10.1080/01998595.2010.10132367

Bonano, M., Manunta, M., Marsella, M., Lanari, R., 2012. Long-term ERS/ENVISAT deformation time-series generation at full spatial resolution via the extended SBAS technique. Int. J. Remote Sens. 33, 4756–4783. https://doi.org/10.1080/01431161.2011.638340

Bröring, A., Echterhoff, J., Jirka, S., Simonis, I., Everding, T., Stasch, C., Liang, S., Lemmens, R., 2011. New Generation Sensor Web Enablement. Sensors 11, 2652–2699. https://doi.org/10.3390/s110302652

Buldrini, F., Simoncelli, A., Accordi, S., Pezzi, G., Dallai, D., 2015. Ten years of citizen science data collection of wetland plants in an urban protected area. Acta Bot. Gall. 162, 365–373. https://doi.org/10.1080/12538078.2015.1080187

Bürger für Leipzig Stiftung, n.d. Flächen in Leipzig [WWW Document]. URL http://www.flaechen-in-leipzig.de/brachen/index.asp (accessed 4.15.19).

Cartwright, L.A., Cvetkovic, M., Graham, S., Tozer, D., Chow-Fraser, P., 2015. URBAN: Development of a Citizen Science Biomonitoring Program Based in Hamilton, Ontario, Canada. Int. J. Sci. Educ. Part B 5, 93–113. https://doi.org/10.1080/21548455.2013.855353

Chen, N., Chen, X., Wang, K., Niu, X., 2014. Progress and challenges in the architecture and service pattern of Earth Observation Sensor Web for Digital Earth. Int. J. Digit. Earth 7, 935–951. https://doi.org/10.1080/17538947.2013.834385

Chen, X.-L., Zhao, H.-M., Li, P.-X., Yin, Z.-Y., 2006. Remote sensing image-based analysis of the relationship between urban heat island and land use/cover changes. Remote Sens. Environ. 104, 133–146. https://doi.org/10.1016/j.rse.2005.11.016

Clerici, N., Valbuena Calderón, C.A., Posada, J.M., 2017. Fusion of Sentinel-1A and Sentinel-2A data for land cover mapping: a case study in the lower Magdalena region, Colombia. J. Maps 13, 718–726. https://doi.org/10.1080/17445647.2017.1372316

Coll, C., Galve, J.M., Sanchez, J.M., Caselles, V., 2010. Validation of Landsat-7/ETM+ Thermal-Band Calibration and Atmospheric Correction With Ground-Based Measurements. IEEE Trans. Geosci. Remote Sens. 48, 547–555. https://doi.org/10.1109/TGRS.2009.2024934

Connors, J.P., Lei, S., Kelly, M., 2012. Citizen Science in the Age of Neogeography: Utilizing Volunteered Geographic Information for Environmental Monitoring. Ann. Assoc. Am. Geogr. 102, 1267–1289. https://doi.org/10.1080/00045608.2011.627058

Copernicus Programme, 2019a. Copernicus Land Monitoring Service [WWW Document]. URL https://land.copernicus.eu/pan-european (accessed 5.17.20).

Copernicus Programme, 2019b. CORINE Land Cover [WWW Document]. URL https://land.copernicus.eu/pan-european/corine-land-cover (accessed 4.15.19).

Corbane, C., Lemoine, G., Pesaresi, M., Kemper, T., Sabo, F., Ferri, S., Syrris, V., 2018. Enhanced automatic detection of human settlements using Sentinel-1 interferometric coherence. Int. J. Remote Sens. 39, 842–853. https://doi.org/10.1080/01431161.2017.1392642

Councell, T.B., Duckenfield, K.U., Landa, E.R., Callender, E., 2004. Tire-Wear Particles as a Source of Zinc to the Environment. Environ. Sci. Technol. 38, 4206–4214. https://doi.org/10.1021/es034631f

Craglia, M., Shanley, L., 2015. Data democracy – increased supply of geospatial information and expanded participatory processes in the production of data. Int. J. Digit. Earth 8, 679–693. https://doi.org/10.1080/17538947.2015.1008214

Crowe, P.R., Foley, K., 2017. Exploring urban resilience in practice: a century of vacant sites mapping in Dublin, Edinburgh and Philadelphia. J. Urban Des. 22, 208–228. https://doi.org/10.1080/13574809.2017.1298401

Curran, P.J., 1985. Principles of Remote Sensing. Longman, London.

CzechInvest, 2018. Database of brownfields [WWW Document]. URL http://www.brownfieldy.eu/en/home/ (accessed 4.15.19).

CzechInvest, n.d. History [WWW Document]. URL https://www.czechinvest.org/en/About-CzechInvest/History (accessed 4.15.19).

Demirbas, M.F., 2006. Thermal Energy Storage and Phase Change Materials: An Overview. Energy Sources, Part B Econ. Planning, Policy 1, 85–95. https://doi.org/10.1080/009083190881481

Documentation QGIS Testing, n.d. Raster Analysis [WWW Document]. URL https://docs.qgis.org/testing/en/docs/user_manual/working_with_raster/raster_analysis.html (accessed 4.15.19).

Edil, T.B., 2008. A review of environmental impacts and environmental applications of shredded scrap tires, in: Hazarika, H., Yasuhara, K. (Eds.), Scrap Tire Derived Geomaterials. Opportunities and Challenges. CRC Press, Boca Raton, FL, pp. 3–18.

EEA, 2017. Climate change, impacts and vulnerability in Europe 2016. An indicator-based report. Luxembourg. https://doi.org/10.2800/534806

EEA, FOEN, 2016. Urban sprawl in Europe. Joint EEA-FOEN report. https://doi.org/10.2800/143470

Ehlers, M., Klonus, S., Johan Åstrand, P., Rosso, P., 2010. Multi-sensor image fusion for pansharpening in remote sensing. Int. J. Image Data Fusion 1, 25–45. https://doi.org/10.1080/19479830903561985

EPA, n.d. Brownfields [WWW Document]. URL https://www.epa.gov/brownfields (accessed 4.15.19).

ESA, 2019. Proba-1 [WWW Document]. URL https://earth.esa.int/web/guest/missions/esa-operational-eo-missions/proba (accessed 4.14.19).

Essa, W., van der Kwast, J., Verbeiren, B., Batelaan, O., 2013. Downscaling of thermal images over urban areas using the land surface temperature–impervious percentage relationship. Int. J. Appl. Earth Obs. Geoinf. 23, 95–108. https://doi.org/10.1016/j.jag.2012.12.007

European Commission, 2016. Mapping Guide Urban Atlas.

European Commission, 2011. The EU Biodiversity Strategy to 2020. Luxembourg. https://doi.org/10.2779/39229

Fiaschi, S., Tessitore, S., Bonì, R., Di Martire, D., Achilli, V., Borgstrom, S., Ibrahim, A., Floris, M., Meisina, C., Ramondini, M., Calcaterra, D., 2017. From ERS-1/2 to Sentinel-1: two decades of subsidence monitored through A-DInSAR techniques in the Ravenna area (Italy). GIScience Remote Sens. 54, 305–328. https://doi.org/10.1080/15481603.2016.1269404

FLIR, n.d. FLIR MSX® – Multi-Spectral Dynamic Imaging [WWW Document]. URL https://www.flir.com/instruments/multi-spectral-dynamic-imaging/ (accessed 5.10.20).

Forkuor, G., Dimobe, K., Serme, I., Tondoh, J.E., 2018. Landsat-8 vs. Sentinel-2: examining the added value of sentinel-2's red-edge bands to land-use and land-cover mapping in Burkina Faso. GIScience Remote Sens. 55, 331–354. https://doi.org/10.1080/15481603.2017.1370169

Franci, F., Mandanici, E., Bitelli, G., 2015. Remote sensing analysis for flood risk management in urban sprawl contexts. Geomatics, Nat. Hazards Risk 6, 583–599. https://doi.org/10.1080/19475705.2014.913695

Friedel, M.J., Buscema, M., Vicente, L.E., Iwashita, F., Koga-Vicente, A., 2018. Mapping fractional landscape soils and vegetation components from Hyperion satellite imagery using an unsupervised machine-learning workflow. Int. J. Digit. Earth 11, 670–690. https://doi.org/10.1080/17538947.2017.1349841

Funning, G.J., Parsons, B., Wright, T.J., Jackson, J.A., Fielding, E.J., 2005. Surface displacements and source parameters of the 2003 Bam (Iran) earthquake from Envisat advanced synthetic aperture radar imagery. J. Geophys. Res. Solid Earth 110. https://doi.org/10.1029/2004JB003338

GAF, 2019. Copernicus Land Monitoring: High-Resolution Layers 2018 kick off! [WWW Document]. URL https://www.gaf.de/content/copernicus-land-monitoring-high-resolution-layers-2018-kick (accessed 4.15.19).

Gallaun, H., Sannier, C., Pennec, A., Weis, E., Hirschmugl, M., Steinegger, M., Miletich, P., 2017. GMES Initial Operations / Copernicus Land monitoring services – Validation of products. Validation Services for the geospatial products of the Copernicus land Continental and local components including in-situ data (lot 1). Tenders – EEA/MDI/14/010.

Gao, F., de Colstoun, E.B., Ma, R., Weng, Q., Masek, J.G., Chen, J., Pan, Y., Song, C., 2012. Mapping impervious surface expansion using medium-resolution satellite image time series: a case study in the Yangtze River Delta, China. Int. J. Remote Sens. 33, 7609–7628. https://doi.org/10.1080/01431161.2012.700424

GEO, n.d. About us [WWW Document]. URL https://www.earthobservations.org/geo_community.php (accessed 4.15.19).

Goetz, A.F.H., Vane, G., Solomon, J.E., Rock, B.N., 1985. Imaging Spectrometry for Earth Remote Sensing. Science (80-.). 228, 1147–1153. https://doi.org/10.1126/science.228.4704.1147

Golubiewski, N.E., Wessman, C.A., 2010. Discriminating urban vegetation from a metropolitan matrix through partial unmixing with hyperspectral AVIRIS data. Can. J. Remote Sens. 36, 261–275. https://doi.org/10.5589/m10-041

Gonzalez, R.C., Woods, R.E., 2007. Digital Image Processing, 3rd ed. Prentice Hall International, Upper Saddle River, NJ.

Gooch, M.J., Chandler, J.H., Stojic, M., 1999. Accuracy Assessment of Digital Elevation Models Generated Using the Erdas Imagine Orthomax Digital Photogrammetric System. Photogramm. Rec. 16, 519–531. https://doi.org/10.1111/0031-868X.00140

Goodman, M., n.d. Understanding Proprietary Infrared Image Files [WWW Document]. URL https://www.irinfo.org/04-01-2006-colbert/ (accessed 4.15.19).

Graham, E., 1993. The Urban Heat Island of Dublin City During the Summer Months. Irish Geogr. 26, 45–57. https://doi.org/10.1080/00750779309478717

Greater London Authority, 2019. Brownfield Land Register - London Datastore [WWW Document]. URL https://data.london.gov.uk/dataset/brownfield-land-register (accessed 4.15.19).

Harris Geospatial Solutions, 2019. Fast Fourier Transform (FFT) Background [WWW Document]. URL https://www.harrisgeospatial.com/docs/BackgroundFastFourierTransform.html (accessed 4.15.19).

Heldens, W., Taubenböck, H., Esch, T., Heiden, U., Wurm, M., 2013. Analysis of Surface Thermal Patterns in Relation to Urban Structure Types: A Case Study for the City of Munich, in: Remote Sensing and Digital Image Processing. pp. 475–493. https://doi.org/10.1007/978-94-007-6639-6_23

Henry, J. -B., Chastanet, P., Fellah, K., Desnos, Y. -L., 2006. Envisat multi-polarized ASAR data for flood mapping. Int. J. Remote Sens. 27, 1921–1929. https://doi.org/10.1080/01431160500486724

Hillen, F., Höfle, B., Ehlers, M., Reinartz, P., 2014. Information fusion infrastructure for remote-sensing and in-situ sensor data to model people dynamics. Int. J. Image Data Fusion 5, 54–69. https://doi.org/10.1080/19479832.2013.870934

Hörig, B., Kühn, F., Oschütz, F., Lehmann, F., 2001. HyMap hyperspectral remote sensing to detect hydrocarbons. Int. J. Remote Sens. 22, 1413–1422. https://doi.org/10.1080/01431160120909

Hu, Y., Liu, X., Bai, J., Shih, K., Zeng, E.Y., Cheng, H., 2013. Assessing heavy metal pollution in the surface soils of a region that had undergone three decades of intense industrialization and urbanization. Environ. Sci. Pollut. Res. 20, 6150–6159. https://doi.org/10.1007/s11356-013-1668-z

Humboldt State University, 2018. Radiometric Calibration and Corrections [WWW Document]. URL http://gsp.humboldt.edu/OLM/Courses/GSP_216_Online/lesson4-1/radiometric.html (accessed 4.15.19).

Hutgens, C., Vohland, M., 2014. Downscaling land surface temperatures from MODIS data to mesoscale resolution with Random Forest regression, in: Seyfert, E., Gülch, E., Heipke, C., Schiewe, J., Sester, M. (Eds.), Geoinformation Öffnet Das Tor Zur Welt. DGPF Tagungsband 23. Deutsche Gesellschaft für Photogrammetrie, Fernerkundung und Geoinformation e.V., Munich, Germany.

Iino, S., Ito, R., Doi, K., Imaizumi, T., Hikosaka, S., 2018. CNN-based generation of high-accuracy urban distribution maps utilising SAR satellite imagery for short-term change monitoring. Int. J. Image Data Fusion 9, 302–318. https://doi.org/10.1080/19479832.2018.1491897

Jacobs, C., Zipf, A., 2017. Completeness of citizen science biodiversity data from a volunteered geographic information perspective. Geo-spatial Inf. Sci. 20, 3–13. https://doi.org/10.1080/10095020.2017.1288424

Jawak, S.D., Luis, A.J., 2013. A Comprehensive Evaluation of PAN-Sharpening Algorithms Coupled with Resampling Methods for Image Synthesis of Very High Resolution Remotely Sensed Satellite Data. Adv. Remote Sens. 02, 332–344. https://doi.org/10.4236/ars.2013.24036

Jeganathan, C., Hamm, N.A.S., Mukherjee, S., Atkinson, P.M., Raju, P.L.N., Dadhwal, V.K., 2011. Evaluating a thermal image sharpening model over a mixed agricultural landscape in India. Int. J. Appl. Earth Obs. Geoinf. 13, 178–191. https://doi.org/10.1016/j.jag.2010.11.001

Jet Propulsion Laboratory, 2017. AVIRIS - Airborne Visible / Infrared Imaging Spectrometer – Data [WWW Document]. URL https://aviris.jpl.nasa.gov/data/get_aviris_data.html (accessed 4.15.19).

Khorchani, M., Martin-Hernandez, N., Vicente-Serrano, S.M., Azorin-Molina, C., Garcia, M., Domínguez-Duran, M.A., Reig, F., Peña-Gallardo, M., Domínguez-Castro, F., 2018. Average annual and seasonal Land Surface Temperature, Spanish Peninsular. J. Maps 14, 465–475. https://doi.org/10.1080/17445647.2018.1500316

Khraisheh, M., Benyahia, F., Adham, S., 2013. Industrial case studies in the petrochemical and gas industry in Qatar for the utilization of industrial waste heat for the production of fresh water by membrane desalination. Desalin. Water Treat. 51, 1769–1775. https://doi.org/10.1080/19443994.2012.714725

Kim, G., Miller, P.A., Nowak, D.J., 2018. Urban vacant land typology: A tool for managing urban vacant land. Sustain. Cities Soc. 36, 144–156. https://doi.org/10.1016/j.scs.2017.09.014

Koppel, K., Zalite, K., Voormansik, K., Jagdhuber, T., 2017. Sensitivity of Sentinel-1 backscatter to characteristics of buildings. Int. J. Remote Sens. 38, 6298–6318. https://doi.org/10.1080/01431161.2017.1353160

Kovářík, V., 2011. Possibilities of Geospatial Data Analysis Using Spatial Modeling in ERDAS IMAGINE, in: Proceedings of the International Conference on Military Technologies 2011 – ICMT'11. Brno, Czech Republic, pp. 525–531.

Kruse, F.A., Boardman, J.W., Lefkoff, A.B., Young, J.M., Kierein-Young, K.S., 2000. HyMap: an Australian Hyperspectral Sensor Solving Global Problems – Results from USA HyMap Data Acquisitions, in: Proceedings of the 10th Australasian Remote Sensing and Photogrammetry Conference. Remote Sensing and Photogrammetry Association of Australasia, Adelaide, Australia.

Kustas, W.P., Norman, J.M., Anderson, M.C., French, A.N., 2003. Estimating subpixel surface temperatures and energy fluxes from the vegetation index–radiometric temperature relationship. Remote Sens. Environ. 85, 429–440. https://doi.org/10.1016/S0034-4257(03)00036-1

Kyriou, A., Nikolakopoulos, K., 2018. Assessing the suitability of Sentinel-1 data for landslide mapping. Eur. J. Remote Sens. 51, 402–411. https://doi.org/10.1080/22797254.2018.1444944

Labib, S.M., Harris, A., 2018. The potentials of Sentinel-2 and LandSat-8 data in green infrastructure extraction, using object based image analysis (OBIA) method. Eur. J. Remote Sens. 51, 231–240. https://doi.org/10.1080/22797254.2017.1419441

Lauriola, P., 2016. Introduction, in: Musco, F. (Ed.), Counteracting Urban Heat Island Effects in a Global Climate Change Scenario. Springer, Basel, Switzerland, pp. XLVII–LIII. https://doi.org/10.1007/978-3-319-10425-6

Leighton, J.M., Sowter, A., Tragheim, D., Bingley, R.M., Teferle, F.N., 2013. Land motion in the urban area of Nottingham observed by ENVISAT-1. Int. J. Remote Sens. 34, 982–1003. https://doi.org/10.1080/01431161.2012.714507

Li, J., Song, C., Cao, L., Zhu, F., Meng, X., Wu, J., 2011. Impacts of landscape structure on surface urban heat islands: A case study of Shanghai, China. Remote Sens. Environ. 115, 3249–3263. https://doi.org/10.1016/j.rse.2011.07.008

Li, M., Zhang, Z., Lo Seen, D., Sun, J., Zhao, X., 2016. Spatiotemporal Characteristics of Urban Sprawl in Chinese Port Cities from 1979 to 2013. Sustainability 8. https://doi.org/10.3390/su8111138

Li, S., Li, Z., Gong, J., 2010. Multivariate statistical analysis of measures for assessing the quality of image fusion. Int. J. Image Data Fusion 1, 47–66. https://doi.org/10.1080/19479830903562009

Li, Z.-L., Tang, B.-H., Wu, H., Ren, H., Yan, G., Wan, Z., Trigo, I.F., Sobrino, J.A., 2013. Satellite-derived land surface temperature: Current status and perspectives. Remote Sens. Environ. 131, 14–37. https://doi.org/10.1016/j.rse.2012.12.008

Liang, B., Weng, Q., Tong, X., 2013. An evaluation of fractal characteristics of urban landscape in Indianapolis, USA, using multi-sensor satellite images. Int. J. Remote Sens. 34, 804–823. https://doi.org/10.1080/01431161.2012.714506

Lo, C.P., Quattrochi, D.A., 2003. Land-Use and Land-Cover Change, Urban Heat Island Phenomenon, and Health Implications. Photogramm. Eng. Remote Sens. 69, 1053–1063. https://doi.org/10.14358/PERS.69.9.1053

Lo, C.P., Quattrochi, D.A., Luvall, J.C., 1997. Application of high-resolution thermal infrared remote sensing and GIS to assess the urban heat island effect. Int. J. Remote Sens. 18, 287–304. https://doi.org/10.1080/014311697219079

Long, H., Zhao, Z., 2005. Urban road extraction from high-resolution optical satellite images. Int. J. Remote Sens. 26, 4907–4921. https://doi.org/10.1080/01431160500258966

Long, W., Srihar, S., 2004. Land cover classification of SSC image: unsupervised and supervised classification using ERDAS imagine, in: IGARSS 2004. IEEE International Geoscience and Remote Sensing Symposium. Anchorage, AK, pp. 2707–2712. https://doi.org/10.1109/IGARSS.2004.1369859

Longley, P.A., Goodchild, M.F., Maguire, D.J., Rhind, D.W., 2015. Geographic Information Science and Systems. Wiley, Hoboken, NJ.

Lucas, R., Rowlands, A., Brown, A., Keyworth, S., Bunting, P., 2007. Rule-based classification of multi-temporal satellite imagery for habitat and agricultural land cover mapping. ISPRS J. Photogramm. Remote Sens. 62, 165–185. https://doi.org/10.1016/j.isprsjprs.2007.03.003

Mahour, M., Tolpekin, V., Stein, A., Sharifi, A., 2017. A comparison of two downscaling procedures to increase the spatial resolution of mapping actual evapotranspiration. ISPRS J. Photogramm. Remote Sens. 126, 56–67. https://doi.org/10.1016/j.isprsjprs.2017.02.004

MathWorks, 2019. Histogram of image data [WWW Document]. URL https://www.mathworks.com/help/images/ref/imhist.html (accessed 4.15.19).

Mayunga, S.D., Coleman, D.J., Zhang, Y., 2010. Semi-automatic building extraction in dense urban settlement areas from high-resolution satellite images. Surv. Rev. 42, 50–61. https://doi.org/10.1179/003962609X451690

Millar, E.E., Hazell, E.C., Melles, S.J., 2019. The 'cottage effect' in citizen science? Spatial bias in aquatic monitoring programs. Int. J. Geogr. Inf. Sci. 33, 1612–1632. https://doi.org/10.1080/13658816.2018.1423686

Mukherjee, S., Joshi, P.K., Garg, R.D., 2017. Analysis of urban built-up areas and surface urban heat island using downscaled MODIS derived land surface temperature data. Geocarto Int. 32, 900–918. https://doi.org/10.1080/10106049.2016.1222634

Murata, T., Kawai, N., 2018. Degradation of the urban ecosystem function due to soil sealing: involvement in the heat island phenomenon and hydrologic cycle in the Tokyo metropolitan area. Soil Sci. Plant Nutr. 64, 145–155. https://doi.org/10.1080/00380768.2018.1439342

Ngie, A., Abutaleb, K., Ahmed, F., Darwish, A., Ahmed, M., 2014. Assessment of urban heat island using satellite remotely sensed imagery: a review. South African Geogr. J. 96, 198–214. https://doi.org/10.1080/03736245.2014.924864

Nichol, J., 2009. An Emissivity Modulation Method for Spatial Enhancement of Thermal Satellite Images in Urban Heat Island Analysis. Photogramm. Eng. Remote Sens. 75, 547–556. https://doi.org/10.14358/PERS.75.5.547

Nichol, J., 2005. Remote Sensing of Urban Heat Islands by Day and Night. Photogramm. Eng. Remote Sens. 71, 613–621. https://doi.org/10.14358/PERS.71.5.613

Nichol, J., Lee, C.M., 2005. Urban vegetation monitoring in Hong Kong using high resolution multispectral images. Int. J. Remote Sens. 26, 903–918. https://doi.org/10.1080/01431160412331291198

Nichol, J.E., 1996. Analysis of the urban thermal environment with LANDSAT data. Environ. Plan. B Plan. Des. 23, 733–747. https://doi.org/Doi 10.1068/B230733

Nie, Q., Man, W., Li, Z., Huang, Y., 2016. Spatiotemporal Impact of Urban Impervious Surface on Land Surface Temperature in Shanghai, China. Can. J. Remote Sens. 42, 680–689. https://doi.org/10.1080/07038992.2016.1217484

Northam, R.M., 1971. Vacant Urban Land in the American City. Land Econ. 47, 345–355. https://doi.org/10.2307/3145071

Nosek, B.A., Alter, G., Banks, G.C., Borsboom, D., Bowman, S.D., Breckler, S.J., Buck, S., Chambers, C.D., Chin, G., Christensen, G., Contestabile, M., Dafoe, A., Eich, E., Freese, J., Glennerster, R., Goroff, D., Green, D.P., Hesse, B., Humphreys, M., Ishiyama, J., Karlan, D., Kraut, A., Lupia, A., Mabry, P., Madon, T., Malhotra, N., Mayo-Wilson, E., McNutt, M., Miguel, E., Paluck, E.L., Simonsohn, U., Soderberg, C., Spellman, B.A., Turitto, J., VandenBos, G., Vazire, S., Wagenmakers, E.J., Wilson, R., Yarkoni, T., 2015. Promoting an open research culture. Science (80-.). 348, 1422–1425. https://doi.org/10.1126/science.aab2374

OGC, 2019. The Open Geospatial Consortium [WWW Document]. URL http://www.opengeospatial.org/ (accessed 4.15.19).

OSM, n.d. Landuse [WWW Document]. URL https://taginfo.openstreetmap.org/keys/landuse#values (accessed 4.15.19).

Palubinskas, G., 2013. Fast, simple, and good pan-sharpening method. J. Appl. Remote Sens. 7. https://doi.org/10.1117/1.JRS.7.073526

Palubinskas, G., Reinartz, P., 2011. Multi-resolution, multi-sensor image fusion: General fusion framework, in: Stilla, U., Gamba, P., Juergens, C., Maktav, D. (Eds.), Proceedings of Joint Urban Remote Sensing Event, JURSE 2011. Munich, Germany, pp. 313–316. https://doi.org/10.1109/JURSE.2011.5764782

Papadakis, D., Milosavljevic, I., 2019. Copernicus Sentinel Benefits Study. Exploring sectoral uptake of Sentinel data within academic publications.

Parr, D.A., Scholz, M., 2015. Building a Low-Cost Geographic Website for Collecting Citizen Science Contributions. Pap. Appl. Geogr. 1, 205–211. https://doi.org/10.1080/23754931.2015.1014263

Pesaresi, M., Corbane, C., Julea, A., Florczyk, A., Syrris, V., Soille, P., 2016. Assessment of the Added-Value of Sentinel-2 for Detecting Built-up Areas. Remote Sens. 8. https://doi.org/10.3390/rs8040299

Plank, S., Jüssi, M., Martinis, S., Twele, A., 2017. Mapping of flooded vegetation by means of polarimetric Sentinel-1 and ALOS-2/PALSAR-2 imagery. Int. J. Remote Sens. 38, 3831–3850. https://doi.org/10.1080/01431161.2017.1306143

Pohl, C., Moellmann, J., Fries, K., 2017. Standardizing quality assessment of fused remotely sensed images. Int. Arch. Photogramm. Remote Sens. Spat. Inf. Sci. – ISPRS Arch. 42, 863–869. https://doi.org/10.5194/isprs-archives-XLII-2-W7-863-2017

Pohl, C., van Genderen, J.L., 2017. Remote Sensing Image Fusion: A Practical Guide. CRC Press, Boca Raton, FL.

Pohl, C., van Genderen, J.L., 1998. Review article. Multisensor image fusion in remote sensing: Concepts, methods and applications. Int. J. Remote Sens. 19, 823–854. https://doi.org/10.1080/014311698215748

Preuß, T., Verbücheln, M. (Eds.), 2013. Towards Circular Flow Land Use Management. The CircUse Compendium. German Institute of Urban Affairs, Berlin.

Priyadarsini, R., 2009. Urban Heat Island and its Impact on Building Energy Consumption. Adv. Build. Energy Res. 3, 261–270. https://doi.org/10.3763/aber.2009.0310

Ramanathan, V., Crutzen, P.J., Kiehl, J.T., Rosenfeld, D., 2001. Aerosols, Climate, and the Hydrological Cycle. Science (80-.). 294, 2119–2124. https://doi.org/10.1126/science.1064034

Rashed, T., Jürgens, C., 2010. Remote Sensing of Urban and Suburban Areas, Remote Sensing and Digital Image Processing, Remote Sensing and Digital Image Processing. Springer, Dordrecht. https://doi.org/10.1007/978-1-4020-4385-7

Raucoules, D., Le Mouelic, S., Carnec, C., King, C., 2003. Urban subsidence in the city of Prato (Italy) monitored by satellite radar interferometry, in: 2003 IEEE International Geoscience and Remote Sensing Symposium. Proceedings. IEEE, Toulouse, France, pp. 1225–1227. https://doi.org/10.1109/IGARSS.2002.1025896

Riaza, A., Buzzi, J., García-Meléndez, E., Carrère, V., Sarmiento, A., Müller, A., 2015. Monitoring acidic water in a polluted river with hyperspectral remote sensing (HyMap). Hydrol. Sci. J. 60, 1064–1077. https://doi.org/10.1080/02626667.2014.899704

Rodriguez-Galiano, V., Pardo-Iguzquiza, E., Sanchez-Castillo, M., Chica-Olmo, M., Chica-Rivas, M., 2012. Downscaling Landsat 7 ETM+ thermal imagery using land surface temperature and NDVI images. Int. J. Appl. Earth Obs. Geoinf. 18, 515–527. https://doi.org/10.1016/j.jag.2011.10.002

Rujoiu-Mare, M.-R., Olariu, B., Mihai, B.-A., Nistor, C., Săvulescu, I., 2017. Land cover classification in Romanian Carpathians and Subcarpathians using multi-date Sentinel-2 remote sensing imagery. Eur. J. Remote Sens. 50, 496–508. https://doi.org/10.1080/22797254.2017.1365570

Sandifer, P.A., Sutton-Grier, A.E., Ward, B.P., 2015. Exploring connections among nature, biodiversity, ecosystem services, and human health and well-being: Opportunities to enhance health and biodiversity conservation. Ecosyst. Serv. 12, 1–15. https://doi.org/10.1016/j.ecoser.2014.12.007

Santamouris, M., 2013. Using cool pavements as a mitigation strategy to fight urban heat island—A review of the actual developments. Renew. Sustain. Energy Rev. 26, 224–240. https://doi.org/10.1016/j.rser.2013.05.047

Solari, L., Barra, A., Herrera, G., Bianchini, S., Monserrat, O., Béjar-Pizarro, M., Crosetto, M., Sarro, R., Moretti, S., 2018. Fast detection of ground motions on vulnerable elements using Sentinel-1 InSAR data. Geomatics, Nat. Hazards Risk 9, 152–174. https://doi.org/10.1080/19475705.2017.1413013

Stadt Osnabrück, 2019a. Konversion in Osnabrück [WWW Document]. URL https://www.osnabrueck.de/konversion/startseite/ (accessed 4.14.19).

Stadt Osnabrück, 2019b. Kaserne Am Limberg [WWW Document]. URL https://www.osnabrueck.de/konversion/kaserne-am-limberg/ (accessed 4.15.19).

Stadt Osnabrück, 2018. Informationen aus der Osnabrücker Statistik [WWW Document]. Osnabrück Aktuell. URL https://www.osnabrueck.de/fileadmin/eigene_Dateien/01_osnabrueck.de/011_Rathaus/Statistik/user_upload/OS_Aktuell_Interaktiv_201804.pdf (accessed 4.14.19).

Stathopoulou, M., Cartalis, C., 2009. Downscaling AVHRR land surface temperatures for improved surface urban heat island intensity estimation. Remote Sens. Environ. 113, 2592–2605. https://doi.org/10.1016/j.rse.2009.07.017

Tan, K., Liao, Z., Du, P., Wu, L., 2017. Land surface temperature retrieval from Landsat 8 data and validation with geosensor network. Front. Earth Sci. 11, 20–34. https://doi.org/10.1007/s11707-016-0570-7

Tang, J., Wang, L., Yao, Z., 2006. Analyzing Urban Sprawl Spatial Fragmentation Using Multi-temporal Satellite Images. GIScience Remote Sens. 43, 218–232. https://doi.org/10.2747/1548-1603.43.3.218

Thomas, C., Ranchin, T., Wald, L., Chanussot, J., 2008. Synthesis of Multispectral Images to High Spatial Resolution: A Critical Review of Fusion Methods Based on Remote Sensing Physics. IEEE Trans. Geosci. Remote Sens. 46, 1301–1312. https://doi.org/10.1109/TGRS.2007.912448

Tiwari, P.S., Pande, H., Aye, M.N., 2010. Exploiting IKONOS and Hyperion data fusion for automated road extraction. Geocarto Int. 25, 123–131. https://doi.org/10.1080/10106040903180485

Topaloğlu, R.H., Sertel, E., Musaoğlu, N., 2016. Assesment of Classification Accuracies of Sentinel-2 and Landsat-8 Data fpr Land Cover / Use Mapping. nternational Arch. Photogramm. Remote Sens. Spat. Inf. Sci. – ISPRS Arch. XLI-B8, 1055–1059. https://doi.org/10.5194/isprsarchives-XLI-B8-1055-2016

Trianni, G., Dell'Acqua, F., Gamba, P., 2010. Geographic information system (GIS)-aided per-segment scene analysis of multitemporal spaceborne synthetic aperture radar (SAR) series with application to urban areas. Int. J. Remote Sens. 31, 6005–6014. https://doi.org/10.1080/01431161.2010.512304

Twele, A., Cao, W., Plank, S., Martinis, S., 2016. Sentinel-1-based flood mapping: a fully automated processing chain. Int. J. Remote Sens. 37, 2990–3004. https://doi.org/10.1080/01431161.2016.1192304

UK Government, 2017. Brownfield land registers [WWW Document]. URL https://www.gov.uk/guidance/brownfield-land-registers (accessed 4.15.19).

UN, 2015. Transforming our World: The 2030 Agenda for Sustainable Development, General Assembley 70 session. https://doi.org/10.1007/s13398-014-0173-7.2

UN, 2012. The future we want. Outcome document of the United Nations Conference on Sustainable Development. Rio de Janeiro, Brazil, 20–22 June 2012.

UN, n.d. Make cities inclusive, safe, resilient and sustainable [WWW Document]. URL https://www.un.org/sustainabledevelopment/cities/ (accessed 4.15.19).

USGS, 2019. Landsat 7 [WWW Document]. URL https://www.usgs.gov/land-resources/nli/landsat/landsat-7?qt-science_support_page_related_con=0#qt-science_support_page_related_con (accessed 4.14.19).

USGS, 2018a. Earth Observing 1 [WWW Document]. URL https://archive.usgs.gov/archive/sites/eo1.usgs.gov/ (accessed 4.15.19).

USGS, 2018b. Landsat 8 (L8). Data Users Handbook (Version 3.0). Sioux Falls, SD.

Wagner, T.C., 2004. Energy-Savings Systems for Commercial Building CHP and Industrial Waste Heat Applications. Cogener. Distrib. Gener. J. 19, 66–80. https://doi.org/10.1080/15453660409509054

Wald, L., 1999. Some Terms of Reference in Data Fusion. IEEE Trans. Geosci. Remote Sens. 37, 1190–1193. https://doi.org/10.1109/36.763269

Wang, F., Yuan, H., 2010. Challenges of the Sensor Web for disaster management. Int. J. Digit. Earth 3, 260–279. https://doi.org/10.1080/17538947.2010.484510

Wang, Z., Bovik, A.C., 2002. A universal image quality index. IEEE Signal Process. Lett. 9, 81–84. https://doi.org/10.1109/97.995823

Wang, Z., Ziou, D., Armenakis, C., Li, D., Li, Q., 2005. A comparative analysis of image fusion methods, in: IEEE Transactions on Geoscience and Remote Sensing. pp. 1391–1402. https://doi.org/10.1007/978-81-322-0997-3_31

Weng, Q., Hu, X., Lu, D., 2008. Extracting impervious surfaces from medium spatial resolution multispectral and hyperspectral imagery: a comparison. Int. J. Remote Sens. 29, 3209–3232. https://doi.org/10.1080/01431160701469024

Weng, Q., Lu, D., Schubring, J., 2004. Estimation of land surface temperature–vegetation abundance relationship for urban heat island studies. Remote Sens. Environ. 89, 467–483. https://doi.org/10.1016/j.rse.2003.11.005

Wiemann, S., Bernard, L., 2016. Spatial data fusion in Spatial Data Infrastructures using Linked Data. Int. J. Geogr. Inf. Sci. 30, 613–636. https://doi.org/10.1080/13658816.2015.1084420

Xi, Y., Thinh, N.X., Li, C., 2019. Preliminary comparative assessment of various spectral indices for built-up land derived from Landsat-8 OLI and Sentinel-2A MSI imageries. Eur. J. Remote Sens. 52, 240–252. https://doi.org/10.1080/22797254.2019.1584737

Xiao, Q., Ustin, S.L., McPherson, E.G., 2004. Using AVIRIS data and multiple-masking techniques to map urban forest tree species. Int. J. Remote Sens. 25, 5637–5654. https://doi.org/10.1080/01431160412331291224

Xu, S., Ehlers, M., 2017. Hyperspectral image sharpening based on Ehlers fusion. Int. Arch. Photogramm. Remote Sens. Spat. Inf. Sci. – ISPRS Arch. 42, 941–947. https://doi.org/10.5194/isprs-archives-XLII-2-W7-941-2017

Yang, Y., Li, X., Pan, X., Zhang, Y., Cao, C., 2017. Downscaling Land Surface Temperature in Complex Regions by Using Multiple Scale Factors with Adaptive Thresholds. Sensors 17. https://doi.org/10.3390/s17040744

Yuhendra, Alimuddin, I., Sumantyo, J.T.S., Kuze, H., 2012. Assessment of pan-sharpening methods applied to image fusion of remotely sensed multi-band data. Int. J. Appl. Earth Obs. Geoinf. 18, 165–175. https://doi.org/10.1016/j.jag.2012.01.013

Zhan, W., Chen, Y., Wang, J., Zhou, J., Quan, J., Liu, W., Li, J., 2012. Downscaling land surface temperatures with multi-spectral and multi-resolution images. Int. J. Appl. Earth Obs. Geoinf. 18, 23–36. https://doi.org/10.1016/j.jag.2012.01.003

Zhan, W., Chen, Y., Zhou, J., Li, J., Liu, W., 2011. Sharpening Thermal Imageries: A Generalized Theoretical Framework From an Assimilation Perspective. IEEE Trans. Geosci. Remote Sens. 49, 773–789. https://doi.org/10.1109/TGRS.2010.2060342

Zhang, Q., Wang, J., 2003. A rule-based urban land use inferring method for fine-resolution multispectral imagery. Can. J. Remote Sens. 29, 1–13. https://doi.org/10.5589/m02-075

Zhangyan, J., Yunhao, C., Jing, L., 2006. On urban heat island of Beijing based on landsat TM data. Geo-spatial Inf. Sci. 9, 293–297. https://doi.org/10.1007/BF02826743

Zheng, Z., Chen, N., Li, P., Wang, W., 2012. Integration of hydrological observations into a Spatial Data Infrastructure under a Sensor Web environment. Int. J. Digit. Earth 6, 22–40. https://doi.org/10.1080/17538947.2012.743605

Zhou, H., Wang, Y., Yan, S., Li, Y., Liu, X., Zhang, F., 2018. Monitoring of recent ground surface subsidence in the Cangzhou region by the use of the InSAR time-series technique with multi-orbit Sentinel-1 TOPS imagery. Int. J. Remote Sens. 39, 8113–8128. https://doi.org/10.1080/01431161.2018.1482020